

**Quantification of the chemical ozone loss in the
northern and southern polar vortices using
SCIAMACHY limb measurements**

Thiranan Sonkaew

Universität Bremen

**Quantification of the chemical ozone loss in the
northern and southern polar vortices using
SCIAMACHY limb measurements**

Vom Fachbereich für Physik und Elektrotechnik
der Universität Bremen

zur Erlangung des akademischen Grades eines

Doktor der Naturwissenschaften (Dr. rer. nat.)

genehmigte Dissertation

von

Thiranan Sonkaew

1. Gutachter:	Prof. Dr. J. P. Burrows
2. Gutachter:	Prof. Dr. O. Schrems
1. Prüfer:	Prof. Dr. P. Richter
2. Prüfer:	PD Dr. A. Ladstätter-W.
Eingereicht am:	7.12.2009
Tag des Promotionskolloquiums:	18.01.2010

Abstract

This study deals with the retrieval of stratospheric and lower mesospheric ozone profiles from satellite observations of limb-scattered solar radiation with SCIAMACHY on the Envisat satellite. The retrieval combines spectral information in the Chappuis and Hartley absorption bands of ozone and employs the SCIATRAN radiative transfer model. The retrieved ozone profiles are applied into two aspects.

First, the sensitivity of the ozone profile retrieval to tropospheric clouds is examined using the SCIATRAN radiative transfer model. The considered clouds are vertically and horizontally homogeneous. An aerosol-free atmosphere and Mie phase functions for cloud particles are assumed. Neglecting clouds in the retrieval, the relative errors of ozone profile retrievals in a cloudy atmosphere are computed. The cloud sensitivity of the limb ozone retrievals is significant in the Chappuis bands at lower stratospheric altitudes. The relative error in the retrieved ozone concentrations gradually decreases with increasing altitude and becomes negligible above approximately 40 km. Cloud optical thickness, ground albedo and solar zenith angle have a large impact on the ozone retrievals. For a given cloud optical thickness value, clouds with different geometrical thicknesses or different cloud altitudes have a similar impact on the ozone retrievals, if the clouds are outside the field of view of the instrument. The effective radius of water droplets and the solar azimuth angle has a small influence on the error. Neglecting clouds in the ozone profile retrievals generally leads to a low bias. For the most frequent cloud types, the total error is below 6% above 15 km altitude, if clouds are completely neglected in the retrieval.

Second, the stratospheric and lower mesospheric ozone profile data set of SCIAMACHY measurements of limb-scattered solar radiation in the period 2002 - 2009 is used to determine the chemical ozone loss in both the Arctic and Antarctic polar vortices using the vortex average method. The vortex boundary is determined with a potential vorticity (PV) criterion applied to UKMO stratospheric analyses. The chemical ozone loss at the 450 - 600 K isentropic levels is derived from the difference between observed ozone abundances and the ozone modelled considering diabatic cooling, but no chemical ozone loss. The results show accumulated chemical ozone losses of up to 20 - 40% between the beginning of January and the end of March inside the Arctic polar vortex. Strong interannual variability of the Arctic ozone loss is observed, with the cold winters 2005 and 2007 showing the largest chemical ozone losses. The ozone loss in the southern polar vortex does not change much from year to year. At the 475 K isentropic level

total relative ozone losses of 70 - 80% between mid–August and mid–November are observed every year inside the vortex, even in the anomalous year 2002. SCIAMACHY measurements of polar stratospheric clouds and the chemical ozone loss inside polar vortex are in good agreement. Comparisons of the vertical variation of ozone loss derived from SCIAMACHY observations with several independent techniques for the northern hemisphere winter 2004/2005 show very good agreement.

List of Publications

1. Articles in peer-reviewed journals

As first author:

- Sonkaew, T., Rozanov, V. V., von Savigny, C., Rozanov, A., Bovensmann, H. and Burrows, J. P.: 2009, Cloud sensitivity studies for stratospheric and lower mesospheric ozone profile retrievals from measurements of limb-scattered solar radiation, *Atmos. Meas. Tech.*, 2, 653-678
- Sonkaew, T., von Savigny, C., Eichmann, K.-U., Rozanov, A., Weber, M., Bovensmann, H. and Burrows, J. P.: 2009, Chemical ozone loss in Arctic and Antarctic polar winters from SCIAMACHY limb measurements 2002-2009, in progress

As co-author:

- Jones, A., Urban, J., Murtagh, D. P., Eriksson, P., Brohede, S., Haley, C., Degenstein, D., Bourassa, A., von Savigny, C., Sonkaew, T., Rozanov, A., Bovensmann, H. and Burrows, J. P.: 2009, Evolution of stratospheric ozone and water vapour time series studied with satellite measurements, *Atmos. Chem. Phys.*, 9, 6055-6075
- Dikty, S., Weber, M., von Savigny, C., Sonkaew, T., Rozanov, A. and Burrows, J. P.: 2009, Modulations of the 27-day solar rotation signal in stratospheric ozone from SCIAMACHY (2003–2008), *J. Geophys. Res.*, doi:10.1029/2009JD012379, in press

2. Selected oral and poster presentations at conferences and workshops (only first author)

Oral presentations:

- Sonkaew, T., Rozanov, V. V., von Savigny, C., Rozanov, A., Bovensmann, H. and Burrows, J. P.: Cloud sensitivity studies for stratospheric and lower mesospheric ozone profile retrievals from limb scattered solar radiance, The 4th International Limb Workshop, Virginia, USA, October, 2007
- Sonkaew, T., Rozanov, V. V., von Savigny, C., Rozanov, A., Bovensmann, H. and Burrows, J. P.: Cloud sensitivity studies for stratospheric and lower mesospheric ozone profile retrievals from limb scattered solar radiance, SADDU meeting 2008, Bremen, Germany, June, 2008

- Sonkaew, T., Rozanov, V. V., von Savigny, C., Rozanov, A., Rozanov, V. V., Eichmann, K.-U., Bovensmann, H. and Burrows, J. P.: Cloud sensitivity studies to ozone profile retrievals and Chemical ozone loss from SCIAMACHY limb measurements, IUP seminar, Bremen, Germany, January, 2009
- Sonkaew, T., von Savigny, C., Eichmann, K.-U., Rozanov, A., Weber, M., Bovensmann, H. and Burrows, J. P.: 2009, The chemical ozone loss from SCIAMACHY limb measurements in the Arctic and Antarctic winter since 2002–2005, SADDU meeting 2009, Netherlands Institute for Space Research, Utrecht, Netherlands, March, 2009

Poster presentations:

- Sonkaew, T., Rozanov, V. V., von Savigny, C., Rozanov, A., Bovensmann, H. and Burrows, J. P.: Cloud sensitivity studies for stratospheric and lower mesospheric ozone profile retrievals from limb scattered solar radiance, The European Geosciences Union (EGU), Vienna, Austria, April, 2008
- Sonkaew, T., Rozanov, V. V., von Savigny, C., Rozanov, A., Bovensmann, H. and Burrows, J. P.: Cloud sensitivity studies for stratospheric and lower mesospheric ozone profile retrievals from limb scattered solar radiance, Quadrennial Ozone Symposium (QOS), Tromso, Norway, June, 2008
- Sonkaew, T., von Savigny, C., Eichmann, K.-U., Rozanov, A., Bovensmann, H. and Burrows, J. P.: Polar chemical ozone loss as observed from SCIAMACHY, The Atmospheric Science Conference 2009, Barcelona, Spain, September, 2009

Contents

Abstract	i
List of Publications	iii
List of Figures	vii
List of Tables	xii
1 Introduction	1
1.1 Motivation and objective	1
1.2 Thesis contents	2
2 Stratospheric ozone	4
2.1 Ozone chemistry in stratosphere	4
2.1.1 The Chapman mechanism	4
2.1.2 Catalytic ozone destruction cycles	6
2.1.3 Polar ozone hole	10
2.2 Spectroscopy and absorption cross-section of ozone	13
2.3 Dynamics and transport of stratospheric ozone	15
2.3.1 Diabatic ozone descent	17
2.3.2 Potential vorticity as the polar vortex indicator	19
3 SCIAMACHY	21
3.1 The SCIAMACHY instrument	21
3.2 SCIAMACHY measurement geometries	22
3.2.1 The nadir viewing geometry	22
3.2.2 The occultation viewing geometry	23
3.2.3 The limb viewing geometry	23
3.3 The optical configuration of the SCIAMACHY instrument	26
4 Radiative transfer and the ozone retrieval algorithm	28
4.1 Radiative transfer in the atmosphere	28
4.2 Inverse method and optimal estimation	30
4.3 The SCIATRAN software	33

4.4	The ozone profile retrieval methodology	34
4.5	Ozone profile retrieval results	36
5	Cloud sensitivity studies for the ozone profile retrievals from limb measurements	40
5.1	Methodology	41
5.2	Errors associated to clouds	43
5.3	Approximate approach to estimate the retrieval errors	45
5.4	Atmospheric and cloud scenarios	48
5.5	Absolute radiance vs. Chappuis triplet	49
5.6	Investigation of the retrieval errors	53
5.6.1	Cloud optical thickness	54
5.6.2	Effective radius of water droplets	58
5.6.3	Cloud top height and geometrical thickness	60
5.6.4	Ground albedo	61
5.6.5	Solar zenith and azimuthal angles	65
5.6.6	Most frequent clouds	68
5.7	Concluding remarks on the cloud sensitivity of ozone profile retrievals .	69
6	Retrieval of the polar chemical ozone loss using SCIAMACHY limb measurements	71
6.1	The chemical ozone loss algorithms	72
6.2	Polar vortex position	74
6.3	The chemical ozone loss from the vortex average method	80
6.3.1	Arctic chemical ozone loss	80
6.3.2	Antarctic chemical ozone loss	85
6.4	The correlation of chemical ozone loss and polar stratospheric clouds as observed from SCIAMACHY limb measurements	88
6.5	Comparison of the chemical ozone loss from SCIAMACHY limb measurements to other instruments and techniques	93
6.6	Concluding remarks on the chemical ozone loss inside the polar vortex .	95
7	Summary and Outlook	98
A	Relationship between the Chappuis triplet and the limb radiance profile in the center of the Chappuis band	100
B	Abbreviations	108
	Bibliography	110
	Erklärung	126
	Acknowledgements	127

List of Figures

2.1	The temperature dependence of the ozone absorption cross section in different spectral ranges measured with the GOME FM.	15
2.2	The large scale picture of planetary circulation (Fig. is taken from Holton et al. (1995)).	16
3.1	Schematics of the three different viewing geometries of the SCIAMACHY instrument. (Courtesy of S. Noël, IUP, Bremen)	22
3.2	Illustration of the limb and nadir viewing geometries of the SCIAMACHY instrument. (Courtesy of S. Noël, IUP, Bremen)	23
3.3	Orientation of the Envisat orbit plane throughout a year (not to scale and modified from von Savigny (2002)).	25
3.4	Latitudinal coverage of SCIAMACHY limb observations as a function of the month.	25
3.5	The optical configuration of SCIAMACHY, (Graphics courtesy of DLR-IMF).	27
4.1	Samples of monthly averaged ozone profiles retrieved from SCIAMACHY limb–scatter observations for selected months and years in the Arctic (solid line) and Antarctic (dashed line) regions for latitudes poleward of 60°.	37
4.2	Sample validation result for the vertical ozone profiles retrieved from SCIAMACHY and SAGE II instruments at the co–located observations in 2005 (Amekudzi et al., 2008).	38
4.3	Time series of retrieved ozone concentrations from SCIAMACHY and HALOE instruments between 40°N – 60°N latitudes. The top panel shows the ozone concentration at an altitude of 40 km and the bottom panel for an altitude of 25 km.	39
5.1	Contribution of the terms $\Delta S(h_i; 0)/W_f(h_i)$ and $\Delta W(h_i)/W_f(h_i)$ to the linearized approximate retrieval error obtained according to Eq. (5.20). Panel a shows the results for the absolute limb radiance at 602 nm, panel b for the normalized limb radiance at 602 nm and panel c for the Chappuis triplet. The calculations were performed using the parameters given in Table 5.2.	51

5.2	Comparison of the approximate errors of the ozone profile retrieval calculated with and without linearity assumption according to Eqns. (5.20) and (5.13), respectively. Panel (a) shows the results for the absolute limb radiance at 602 nm, panel (b) for the absolute normalized limb radiance at 602 nm, and panel (c) for the Chappuis triplet. The calculations were performed for the same set of parameters as in Fig. 5.1.	53
5.3	Same as Fig. 5.2 but for a surface albedo of 0.9.	54
5.4	An example of the ozone vertical profile obtained neglecting the tropospheric clouds in the retrieval process, as described by Eq. (5.6), in comparison with the true vertical distribution of ozone. The calculations were performed for the same set of parameters as in Fig. 5.1.	55
5.5	Relative errors in the retrieved ozone profiles due to neglect of clouds in the retrieval process. Results are shown for different altitudes of the cloud layer and for different cloud optical thicknesses τ : (a) low clouds (1 – 3 km), (b) middle clouds (2 – 7 km), (c) high clouds (6 – 15 km) for the standard tangent height range, i.e., $h_{low} = 9$ km is the lowest tangent height included in the retrieval, (d) high clouds for the reduced tangent height range, $h_{low} = 19$ km.	56
5.6	Panel a: approximate retrieval error according to Eq. (5.13) at tangent heights of 12 km, 15 km, 19 km and 29 km as a function of the cloud optical thickness. Panel b and panel c: Chappuis triplet for a cloudy and a cloud-free atmosphere as well as integrated weighting function at a tangent height of 12 km and 29 km respectively. The calculations were performed for a middle cloud (the same scenario as in Fig. 5.5b). Please note that the subscripts “c” and “f” refer to a cloudy and a cloud-free atmosphere, respectively.	57
5.7	Panel a: relative errors in the retrieved ozone profiles due to neglect of clouds in the retrieval process for different r_e . Panel b: approximate retrieval error according to Eq. (5.13) at tangent heights of 12 km, 15 km, and 19 km as a function of the r_e . Panel c: Chappuis triplet for a cloudy and a cloud-free atmosphere as well as integrated weighting function at a tangent height of 12 km. The calculations were performed for a middle cloud and the parameter set given in Table 5.2.	59
5.8	Relative errors in the retrieved ozone profiles due to neglect of clouds in the retrieval process. The results are shown for different cloud top heights and geometrical thicknesses of the cloud. Left panel: different cloud top heights for a fixed cloud geometrical thickness (1 km). Right panel: different cloud geometrical thicknesses for a fixed cloud top height (7 km). The calculations were performed for the parameter set given in Table 5.2.	60

5.9	Panel a: relative errors in the retrieved ozone profiles due to neglect of clouds in the retrieval process for different surface albedos. Panel b: approximate retrieval error according to Eq. (5.13) at tangent heights of 12 km, 15 km, 19 km and 29 km as a function of the surface albedo. Panels c and d: Chappuis triplet for a cloudy and a cloud-free atmosphere as well as integrated weighting function at a tangent height of 12 km and 29 km respectively. The calculations were performed for a middle cloud, $\tau = 10$, and the parameter set given in Table 5.2. Panel e: same as the left top panel but τ of 2.	62
5.10	Relative ozone profile retrieval errors for different surface albedo values A_f in the forward simulations, but a fixed albedo $A_r = 0.3$ assumed in the retrievals (panel a), and a constant albedo of $A_f = 0.3$ in the forward simulations and varying albedo A_r used for the retrievals (panel b). The calculations were performed for the parameter set given in Table 5.2.	64
5.11	Relative errors in the retrieved ozone profiles due to neglect of clouds in the retrieval process for different viewing geometries. Left panel: retrieval errors for different SZAs and a fixed SAA of 90° . Right panel: retrieval errors for different SAAs and a fixed SZA of 30° . The calculations were performed for the scenario as given in Table 5.2.	66
5.12	Left panel: approximate retrieval error according to Eq. (5.13) at tangent heights of 12 km, 15 km, and 19 km as a function of the SZA. Right panel: Chappuis triplet for a cloudy and a cloud-free atmosphere as well as integrated weighting function at a tangent height of 12 km. The calculations were performed for a middle cloud (the same scenario as in Fig. 5.11).	67
5.13	Relative errors in the retrieved ozone profiles due to neglect of clouds in the retrieval process for viewing geometries typical for SCIAMACHY (left panel) and OSIRIS (right panel) measurements. The calculations were performed for a middle cloud (the same scenario as in Fig. 5.11).	67
5.14	Relative errors in the retrieved ozone profiles due to neglect of clouds in the retrieval process for most frequent clouds for typical viewing geometries of the SCIAMACHY instrument. The calculations were performed with the scenario as given in Table 5.2.	69
6.1	The daily and zonally averaged modified potential vorticity at the 475 K isentropic level in the Arctic stratosphere for latitudes of SCIAMACHY observations in 2002 – 2009 during winter – spring (given in modified potential vorticity unit (MPVU)). Data were averaged over 5° latitude bins.	75
6.2	The daily and zonal maximum modified potential vorticity at the 475 K isentropic level in the Arctic stratosphere for the latitudes of SCIAMACHY observations in 2002 – 2009 during winter – spring.	76
6.3	SABER V01.07 temperature data over the Arctic region (70°N – 90°N) in the winters of 2003-2009. The dashed line illustrates the daily highest temperature. (The figure is taken from the presentation of Fussen, D. from the Atmospheric science conference, Barcelona, 2009.)	77

6.4	The daily and zonally averaged modified potential vorticity at the 475 K isentropic level in the Antarctic stratosphere for the latitudes of SCIAMACHY observations in 2002 – 2008 during winter – spring.	78
6.5	The daily and zonal minimum modified potential vorticity at the 475 K isentropic level in the Antarctic stratosphere for the latitudes of SCIAMACHY observations in 2002 – 2008 during winter – spring.	79
6.6	Panel a): observed changes in ozone mixing ratio, panel b): daily change in ozone mixing ratio due to diabatic descent determined with MIRAD model simulations, panel c): accumulated ozone mixing ratio from daily diabatic descent (dashed line) and the observed ozone mixing ratio (solid line), panel d): chemical ozone loss in ppmv (solid line) and the linear fit to the chemical ozone loss (dashed line), and panel e): chemical ozone loss in percent from SCIAMACHY observations at the 475 K isentropic level in the Arctic stratosphere in 2003 – 2009 during winter – spring.	81
6.7	The vortex average ozone loss versus time and potential temperature between the 450 K and 600 K isentropic levels in the Arctic stratosphere derived from SCIAMACHY limb observations for the years 2003-2009.	84
6.8	Panel a): observed changes in ozone mixing ratio, panel b): daily change in ozone mixing ratio due to diabatic descent determined with MIRAD model simulations, panel c): accumulated ozone mixing ratio from daily diabatic descent (dashed line) and the observed ozone mixing ratio (solid line), panel d): chemical ozone loss in ppmv (solid line) and the linear fit to the chemical ozone loss (dashed line), and panel e): chemical ozone loss in percent from SCIAMACHY observation at the 475 K isentropic level in the Antarctic stratosphere in 2002 – 2008 during winter – spring.	85
6.9	The vortex average ozone loss versus time and potential temperature between the 450 K and 600 K isentropic levels in the Antarctic stratosphere derived from SCIAMACHY limb observations between 15 August and 15 November 2002–2008.	87
6.10	Polar maps of PSC occurrence rate in the northern hemisphere during January and February 2003–2009 from SCIAMACHY limb measurements.	89
6.11	Panel a) The variation of PSC occurrence rate and chemical ozone loss from SCIAMACHY limb measurements. The red lines show the averaged PSC occurrence rates in the northern hemisphere in January (triangle) and on February (square) for the 40°–65° latitude range. The chemical ozone losses from the start day (see Table 6.1) until April, 1 are shown as the black line with black-filled circles and until the last day when the polar vortex observed are shown as the black-open circle. Panel b) The red line with triangles shows the averaged PSC occurrence rates in the southern hemisphere during September for the 40°–75° latitude range and the chemical ozone loss between August, 15 and November, 15 is shown as the black line with circles.	90

6.12	Scatter plot of PSC occurrence rate and chemical ozone loss from SCIAMACHY limb measurements. The circles show the PSC occurrence rate in the northern hemisphere in January and the triangles show the PSC occurrence rate in the southern hemisphere in September. The linear fit of PSC occurrence rate and chemical ozone loss is shown in the blue line for the northern hemisphere and the red line for both hemispheres.	91
6.13	Polar maps of PSC occurrence rate in the southern hemisphere during August and September 2002–2008 from SCIAMACHY limb measurements.	92
6.14	The chemical ozone loss over the time period from 5 January to 25 March 2005, estimated using various data sources and techniques. The data from the other instruments and methods are taken from Rex et al. (2006) and references therein.	94
6.15	Chemical ozone loss in the Arctic stratosphere during spring/winter 2004-2005 from the other works. Top panel: Using the passive subtraction technique, differences were determined between passive ozone calculated by the SLIMCAT CTM and ozone measured by the POAM III, SAGE III, EOS MLS, ACE-FTS, and MAESTRO instruments (taken from Singleton et al. (2007)). Bottom panel: Using the vortex average method, the simulated ozone loss at latitude $> 65^{\circ}\text{N}$ from the CLaMS model is shown (taken from Grooß and Müller (2007)).	95

List of Tables

2.1	The theoretical wavelength thresholds (in nm) for different ozone photolysis channels.	14
3.1	Overview of the SCIAMACHY spectrometer channels.	26
4.1	The lowest (h_{low}) and reference (h_r) tangent heights for the wavelengths used.	35
5.1	Cloud classification by top and bottom heights and optical thickness, τ . The τ values are the same as in the ISCCP classification.	49
5.2	Cloud parameter sets used in this study. The varied parameters are marked with (\surd).	50
5.3	Overview of the sensitivity of ozone vertical profile retrievals to the tropospheric clouds (relative retrieval error in % is shown) for the most frequent clouds ¹ for typical viewing geometries of the SCIAMACHY instrument.	69
6.1	The chemical ozone loss rate in the Arctic during 2003–2009 at the 475 K isentropic level between the start and end dates listed.	83
6.2	The chemical ozone loss rate over Antarctica between 15 August and 15 November in 2002–2008 at the 475 K isentropic level.	86

Chapter 1

Introduction

1.1 Motivation and objective

Ozone plays an important role in the evolution of life on earth. About 90% of atmospheric ozone occurs in the stratosphere to absorb the biologically harmful ultraviolet (UV) radiation from the sun. Due to the high absorption of UV radiation by ozone in the stratosphere, this trace gas is one of the major factors determining the vertical temperature profile of the earth's atmosphere. The remaining about 10% of ozone reside in the troposphere. The tropospheric ozone is a pollutant and can damage living tissue of plants, animals and humans. Many studies have shown that the stratospheric ozone abundance has been decreasing globally during the second half of the 20th century until about the mid-nineties, when a change of the sign of the ozone trend occurred, particularly in the upper stratospheric region (e.g., [Newchurch et al., 2003](#); [Jones et al., 2009](#); [Steinbrecht et al., 2009](#)). The general causes of the stratospheric ozone loss have been classified by [Rowland \(2006\)](#) into three types: (i) natural change in the dynamics of the stratosphere; (ii) change in the natural chemistry of NO_x in the stratosphere and (iii) chemical changes induced by mankind, especially through the introduction of artificial chlorine-containing compounds such as the Chlorofluorocarbons (CFCs). The ozone loss driven by these processes leads to a cooling of the stratosphere, because ozone is one of the principal absorbers of solar radiation. Note, that enhanced CO_2 abundances also cause a cooling of the stratosphere. Many efficient catalytic chain reactions to destroy the ozone in the stratosphere were discovered in the last half-century, involving the chemical species HO, HO_2 , NO, NO_2 , Cl and ClO.

This work focuses on the retrieval of stratospheric ozone from the measurements of limb-scattered solar radiation and the application of the retrieved ozone profiles to estimate the chemical ozone loss in the polar vortices in both hemispheres. Additionally, the effect of tropospheric clouds on the retrieval of ozone profiles has also been investigated in detail and will be presented here.

1.2 Thesis contents

The structure of this thesis is as follows:

- Chapter 2 presents an overview of stratospheric ozone chemistry, spectroscopy and the absorption cross-section of ozone. Relevant concepts of atmospheric dynamics will be briefly explained in this chapter as well.
- In chapter 3 the main characteristics of the SCIAMACHY instrument are briefly described.
- In chapter 4 the radiative transfer equation, the retrieval method, and the SCIA-TRAN software package used for retrieving the ozone profiles from the limb-scattered solar radiation are explained. Validation results of the ozone data product from SCIAMACHY limb observations are shown in the last section of this chapter.
- Chapter 5 presents the effect of tropospheric clouds on the retrieval of ozone profiles in the stratosphere and the lower mesosphere from satellite measurements of the scattered solar radiation in limb viewing geometry. Using the numerical simulation method the errors in the retrieved ozone profiles occurring when neglecting tropospheric clouds in the retrieval process are analyzed in dependence of the cloud optical and geometrical parameters, surface albedo, and the viewing geometry (solar zenith and azimuth angles). In the framework of this study the following cloud parameters are considered: cloud optical thickness (τ), cloud top height, effective radius of water droplets (r_e), and cloud geometrical thickness. All results for cloud sensitivity studies are summarized in the last section of this chapter.

- Chapter 6 presents investigations of the chemical ozone loss in the stratosphere over the Arctic and Antarctic regions in winter/spring 2002–2009. The polar vortex as calculated from United Kingdom Meteorological Office (UKMO) stratospheric assimilation data along the SCIAMACHY observation tracks at high latitudes are shown in this chapter. Furthermore, an excellent agreement of the chemical ozone loss derived from SCIAMACHY limb observations with other instruments and methods is presented.
- The conclusions of this work and an outlook are presented in the last chapter.

Chapter 2

Stratospheric ozone

This chapter is divided into three sections. The first section contains an overview of the stratospheric ozone chemistry including the Chapman mechanism and some important catalytic ozone destruction cycles. A short description of the ozone spectroscopy follows in the second section. The atmospheric dynamics relevant for stratospheric ozone is briefly described in the last section.

2.1 Ozone chemistry in stratosphere

2.1.1 The Chapman mechanism

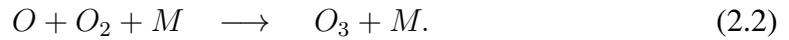
The photochemical theory of ozone formation and destruction was first proposed by [Chapman \(1930\)](#) based on oxygen-only reactions. The elementary reactions now known as the Chapman mechanism are described in the following.

Solar ultraviolet radiation in the stratosphere slowly dissociates molecular oxygen (O_2) in the Schumann-Runge bands (175-200 nm) and in the Hertzberg continuum (extending to 242 nm) producing atomic oxygen (O)



where $h\nu$ denotes a solar ultraviolet photon.

The O reacts rapidly with O_2 and a third molecule, denoted as M (usually O_2 or N_2) to form ozone (O_3)



The O_3 in the above reaction can be rapidly photolized by



decomposing back to O_2 and atomic oxygen O . This atomic oxygen can be in one of two electronic states: $O(^1D)$ (singlet D) or $O(^3P)$ (triplet P). $O(^1D)$ is an electronically excited atomic oxygen and is formed when the absorbed radiation has a wavelength ≤ 310 nm in the Hartley bands (Wayne, 1987). $O(^3P)$ is the ground state atomic oxygen produced when the absorbed radiation has a wavelength in the range of $310 \text{ nm} \leq \lambda \leq 1100$ nm (Huggins or Chappuis bands). Because $O(^1D)$ has higher internal energy and is more reactive than $O(^3P)$, $O(^1D)$ is rapidly converted to $O(^3P)$ through collisions with other molecules such as O_2 or CO_2 . As a result, $O(^3P)$ is more abundant in the stratosphere compared to $O(^1D)$, therefore $O(^3P)$ will be denoted as O further on. More details are described in Section 2.2

The solar UV energy absorbed in reaction 2.3 is converted into heat by processes such as energy transfer to M , providing a thermal source in the 30-50 km altitude range. This process is responsible for maintaining positive temperature gradient versus altitude in the stratosphere. The temperature profile peak at about 50 km defines the stratopause in the atmosphere. The O atom from reaction 2.3 has a very short life time of only between 10^{-2} s and 1 s at 20 km and 40 km, respectively. The O atom immediately re-forms O_3 in reaction 2.2, therefore reaction 2.3 is not considered an ozone loss mechanism.

Chapman proposed the odd oxygen (O_x , i.e., O and O_3) loss mechanism through the reaction



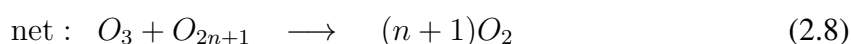
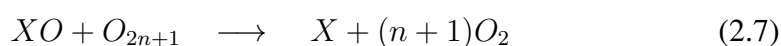
Additionally, the combination of atomic oxygen atoms back to O_2 molecules can be considered as an odd oxygen loss through the reaction



However, Chapman's reactions could not adequately explain the observed ozone in the stratosphere. The prediction of ozone using Chapman's model is higher than the actual globally averaged total ozone by a factor of two. During the second half of the 20th century it has been discovered that stratospheric ozone is chemically destroyed by several catalytic ozone destruction cycles involving other atmospheric trace species.

2.1.2 Catalytic ozone destruction cycles

Several atmospheric trace species participate in catalytic ozone destruction cycles in the stratosphere. The catalytic cycles themselves are pure gas-phase chemistry. Heterogeneous reactions are important to activate Cl, i.e., transfer it from reservoir species ($ClONO_2$ and HCl) to Cl_2 . A brief overview of ozone destruction reactions will be given in this section. The general ozone catalytic destruction cycle is summarized as follows.

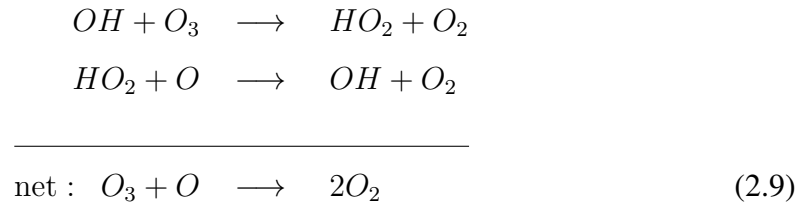


where $X = H, OH, NO, Cl, Br$, belonging to the families of HO_x , NO_x , ClO_x and BrO_x ¹ and $n = \{0, 1\}$.

Based on the work of [Bates and Nicolet \(1950\)](#), [Hampson \(1964\)](#) proposed that stratospheric ozone is catalytically destroyed by HO_x . The main source of OH in the stratosphere is the reaction of atomic oxygen with water vapour. The following reactions

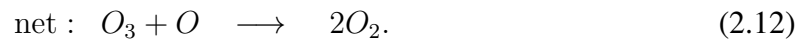
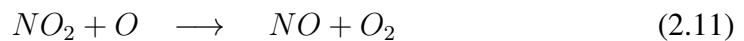
¹ $HO_x = H+OH+HO_2$, $NO_x = NO+NO_2$, $ClO_x = Cl+ClO+OCIO+HOCl+BrCl$, and $BrO_x = Br+BrO+BrCl+HOBr$

show the catalytic ozone loss initiated by hydroxyl (OH).

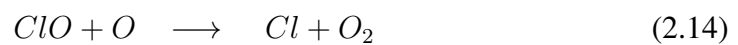
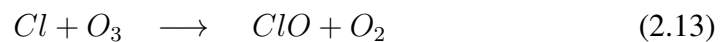


The net effect of this reaction is equivalent to equation 2.8. The HO_x catalytic cycle is most significant at the top of the stratosphere above 45 km altitude.

The most significant contributions to the establishment of the NO_x cycle were the works by Crutzen (1971) and Johnston (1971). The NO_x cycle dominates in the altitude range of 20-40 km and can be summarized as:



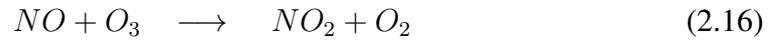
The most important cycle to remove ozone at around 45 km is the ClO_x cycle as suggested by Stolarski and Cicerone (1974):



Almost all chlorine atoms react initially with ozone by reaction 2.13 to form another free radical ClO. The combined effect of all catalytic cycles together with the Chapman reactions allows an adequate description of the observed ozone amounts in the atmosphere.

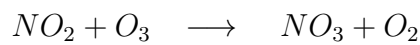
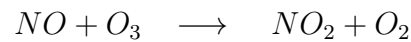
In addition, the loss of ozone from catalytic cycles described above can be determined in terms of odd oxygen loss, i.e., the concentration of O₃ and O. The net overall of the chain reactions is a loss of two odd oxygen by converting the odd oxygen back to even

oxygen (O_2). Some catalytic cycles have no effect on odd oxygen as the change in O_x is balanced in the net reaction. This is called *null cycle*, for example:

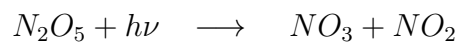
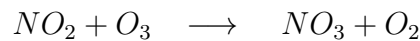
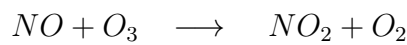


Thus, the efficiency of the NO_x catalytic cycle to destroy the odd oxygen depends on the competition between photolysis (2.17) and the reaction with atomic oxygen (2.11).

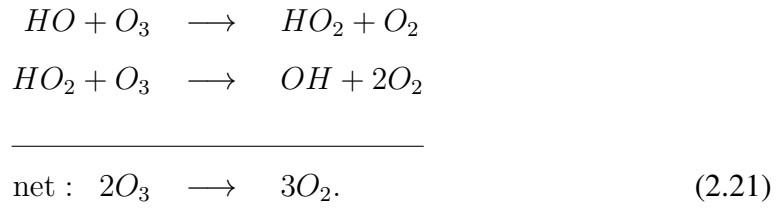
When the catalytic cycles are rate limited by O atoms such as in lower atmospheric regions, then other cycles tend to be important. Two O_3 molecules will be transformed to three O_2 molecules, for example in a NO_x cycle:



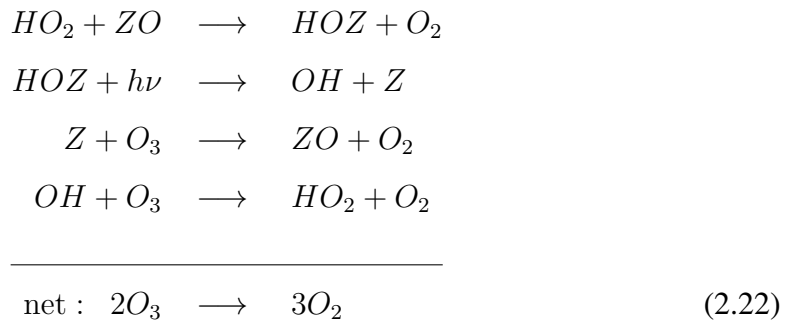
and



The HO_x cycle should also be noted:

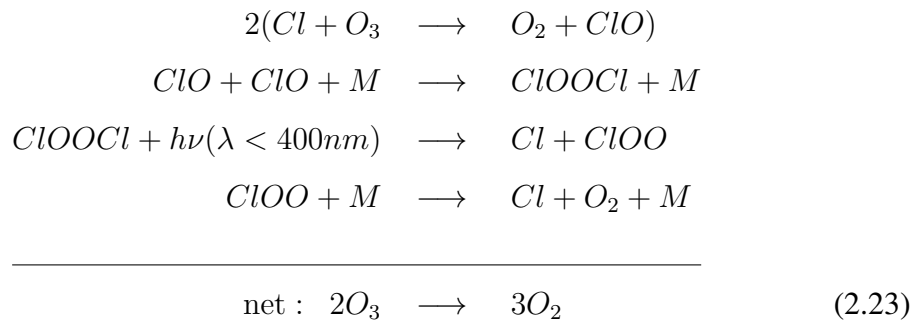


Another O_3 removal cycle in the lower stratosphere near 20 km is:

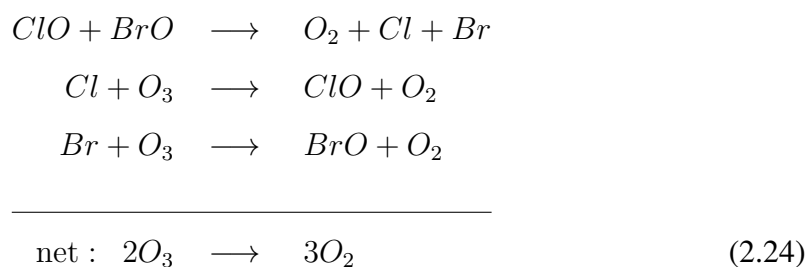


where Z is Cl or Br.

The ClO is of great importance in terms of ozone destruction in regions with limited amounts of O. When the ClO concentration is high (~ 1 ppbv) and the concentration of O atoms is low in the polar lower stratosphere, it can result in the polar ozone hole. The major causes of chemical ozone loss in polar regions involving ClO can be summarized in two catalytic cycles. The first cycle was proposed by [Molina and Molina \(1987\)](#):



The second important catalytic cycle involves both the ClO and BrO (McElroy et al., 1986; Tung et al., 1986):



The net result of these cycles is the destruction of two ozone molecules in the atmosphere.

2.1.3 Polar ozone hole

Massive ozone depletion during austral spring at high southern latitudes was first reported at the Ozone Commission meeting in Halkidiki, Greece, in September 1984 by Chubachi (1984). He used a Dobson spectrophotometer to measure the amount of ozone at Syowa station, Antarctica, from February 1982 through January 1983. His observations show very low amounts of ozone (below 250 DU²) during the October period. However, Chubachi did not point out that these October 1982 total ozone columns were a decrease over October measurements from previous years.

Farman et al. (1985) found large depletions of ozone in September and October of the years 1982 to 1984 over the British Antarctic Survey station at Halley Bay, Antarctica. They reported quickly dropping average October ozone total columns from 300–320 DU in the 1960s to below 200 DU in 1985 and proposed an interaction of ClO_x and NO_x to be responsible for the dramatic loss of spring time polar stratospheric ozone in the southern hemisphere.

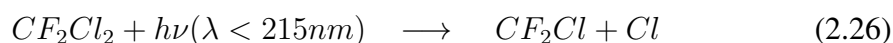
The dramatic decrease of ozone was confirmed by other ground-based observations at other Antarctic stations (Komhyr et al., 1986; Mount et al., 1987) and by the measurements with the Total Ozone Mapping Spectrometer (TOMS) instrument on the Nimbus-7 satellite (Stolarski et al., 1986). As the satellite exploration showed that the depletion extended over 30 million square kilometers, the entire Antarctic continent or about 6%

² 1 Dobson Unit (DU) is defined as an ozone column of 0.01 mm thickness at Standard Temperature and Pressure (STP) corresponding to 2.7×10^{16} ozone molecules/cm².

of the Earth's surface, the phenomenon became known as *the Antarctic ozone hole*. The ozone hole in the atmosphere is the direct effect of human activities. Several theories were proposed to explain the Antarctic ozone hole in the spring season. They can be classified into three categories: i) natural chemistry change of NO_x in the stratosphere, ii) natural dynamics change in the Antarctic stratosphere, and iii) the chemical change from human activities due to injection of chlorine compounds, e.g., CFCs into the atmosphere.

The nitrogen oxide hypothesis was proposed by [Callis and Natarajan \(1986\)](#). High abundances of the NO_x compounds were believed to be produced during the solar maximum around 1979. The NO_x compounds destroy ozone as shown in eq. 2.10-2.12. This theory appeared to be consistent with the observations of [Farmer et al. \(1987\)](#) and [Mankin and Coffey \(1989\)](#) showing low NO_2 concentrations at high latitudes during the Antarctic ozone hole event. Now it is known that the denoxification followed by denitrification inside the polar vortex have different origins.

Polar stratospheric measurements ([Rowland, 1991](#); [Lovelock and Maggs, 1973](#); [Heidt et al., 1975](#); [Schmeltekopf et al., 1975](#)), yielded unusually high stratospheric chlorine concentrations in the mid-1980s compared to the period 1956-1975. The explorations showed that the CFCs such as CFCl_3 (CFC-11) and CF_2Cl_2 (CFC-12) are well mixed in the stratospheric atmosphere. They are capable absorbing the short UV radiation and release Cl atoms that participate in the catalytic destruction of ozone ([Rowland and Molina, 1975](#)).



Laboratory experiments have shown that the atmospheric lifetime of CF_2Cl_2 is about 45 years and about 100 years for CFCl_3 ([Prinn et al., 1987](#)) and no evidence has been found for a major sink of CFCs in the troposphere.

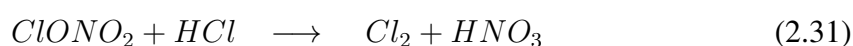
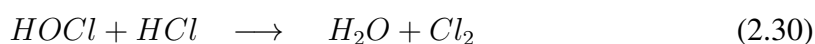
The hypothesis that the sudden stratospheric ozone losses over Antarctica during austral spring involve heterogenous reactions occurring on the surface of polar stratospheric clouds (PSCs) was proposed by [Solomon et al. \(1986\)](#). During winter time the sun is below the horizon, the cold air over Antarctic is surrounded by warmer air at the lower latitudes. This region has strong winds blowing around the boundary between warm and cold air. The rotating air forms the polar vortex isolating the stratospheric polar air

mass from the lower latitude air masses. This effect is more pronounced in the Antarctic than in the Arctic.

Inside the polar vortex, the temperature dramatically drops and is low enough to form PSCs. Several mixtures of hydrates and nitric acid or sulphuric acid can be presented in the PSCs, i.e., nitric acid dihydrate (NAD: $\text{HNO}_3 \cdot 2\text{H}_2\text{O}$), nitric acid trihydrate (NAT: $\text{HNO}_3 \cdot 3\text{H}_2\text{O}$), and sulphuric acid tetrahydrate (SAT: $\text{H}_2\text{SO}_4 \cdot 4\text{H}_2\text{O}$) which facilitate heterogeneous chemistry on the PSCs surface. The size and chemical composition of PSCs is temperature dependent. Two main types of PSCs are classified according to their optical properties (Wayne, 2000).

- Type I PSCs are small with diameter less than $1 \mu\text{m}$, have a mass mixing ratio of about 10 ppbm (part per billion by mass), and consist of HNO_3 particles. This PSCs type is formed at a temperature of about 195 K and often appears in one of two sub-categories. Type Ia is the solid particle consisting of almost pure NAT. Type Ib remains in liquid phase and takes up HNO_3 to form supercooled ternary solutions of $\text{HNO}_3\text{--H}_2\text{SO}_4\text{--}2\text{H}_2\text{O}$.
- Type II PSCs are larger between about $10 \mu\text{m}$ and 1 mm diameter, have a mass mixing ratio of about 1000 ppbm and consist of H_2O –ice. Type II PSCs are formed when the temperature drops below the frost point which is by 5 to 10 K lower than for the Type I PSCs.

In general the chlorine-activation reactions proceed faster on Type II PSCs than on Type I PSCs because the time-scale of the activation processes for Type II PSCs is shorter than for Type I PSCs. The formation of Type II PSCs occurs on time scales of about 1 day at $T \sim 185 \text{ K}$ and only few hours at below 180 K. In case of Type I PSCs formation is in about 10 days. The stratospheric temperature in Antarctic winter is very low which is enough to form Type II PSCs easily. Some of the heterogeneous reactions which efficiently proceed on the PSCs are for example:



The hydrolysis reactions 2.27 and 2.28 are fast on Type II PSCs, but slow on Type I PSCs. Reactions 2.30 and 2.31 are fast on both PSCs Type I and Type II surfaces and return Cl_2 to the atmosphere while HNO_3 remains in the PSC particles. The temporary reservoir compounds HCl and ClONO_2 in reaction 2.31 are the largest fraction of stratospheric chlorine which come from the following reactions:



When the sun reappears in early spring, the Cl or Br compounds are photolyzed and the catalytic ozone destruction chains begin as shown in eq. 2.23 and eq. 2.24. The HNO_3 product can remain in the PSCs, tending to denitrify the lower polar stratosphere. The PSC particles sediment down to lower altitudes, where the NO_x is released again. This NO_x can react with chlorine compounds reforming ClONO_2 reservoir in the atmosphere.

2.2 Spectroscopy and absorption cross-section of ozone

The spectroscopy of ozone has been studied by many scientists in the past. The three-body recombination of atomic and molecular oxygen, eq. 2.2, is the principal ozone-forming reaction at nearly all altitudes in the atmosphere. The ground state of ozone can be approximated as three oxygen atoms in covalent bonds. Each oxygen atom has two unpaired electrons. The central oxygen atom can form a bond with each of the other atoms, leaving an unpaired electron on each terminal atom (Hay and Dunning, 1977). Therefore in fact, ozone in its ground state (X^1A_1 state) is only a compound of $\text{O} - \text{O}_2$ with a bond length of 1.299 \AA and 116° bond angle and has a small bond energy of $\sim 105 \text{ kJmol}^{-1}$. The photolysis of ozone leads to a transition from the ground state to some higher excited states and, of course, leads to the dissociation of the molecules. Depending on the wavelength of the dissociating photons, O and O_2 are produced in different excited states. Table 2.1 shows the thermochemical thresholds for different dissociation channels, expressed as wavelengths in nm.

TABLE 2.1: The theoretical wavelength thresholds (in nm) for different ozone photolysis channels.

	$O_2(^3\Sigma_g^-)$	$O_2(^1\Delta_g)$	$O_2(^1\Sigma_g^+)$	$O_2(^3\Sigma_u^-)$	$O_2(^3\Sigma_u^-)$
$O(^3P)$	1180	612	463	230	173
$O(^1D)$	411	310	267	168	136
$O(^1S)$	237	199	181	129	109

Data taken from [Wayne \(2000\)](#).

Due to spin conservation, the products of photolysis must be both triplets or both singlets³. From Table 2.1, the lowest energy singlet pair is $O(^1D) + O_2(^1\Delta_g)$, hence the favorite threshold wavelength is ~ 310 nm for this spin-allowed channel. The internal vibration and rotation distributions can assist the photon energy causing dissociation of O_3 to form $O(^1D)$ at the wavelength greater than 310 nm. For triplet states, the wavelength has to be less than 1180 nm. The complexity of photodissociation of ozone at wavelength beyond the 310 nm, so-called spin-forbidden, can also contribute to the production pairs $O(^3P) + O_2(^1\Delta_g)$ and $O(^1D) + O_2(^3\Sigma_g^-)$. The GOME Flight Model (FM) absorption cross sections of ozone by [Burrows et al. \(1999\)](#), illustrating the dependence on temperature, are shown in Fig. 2.1 for wavelengths in the UV-Visible spectral range. The temperature dependence of the ozone absorption cross-section is caused by changing rotational and vibrational distributions in the electronic ground state of each transition.

The ozone spectrum is commonly divided into four different absorption bands, i.e., the Hartley, Huggins, Chappuis and Wulf bands. Different ozone absorption bands have different spectral ranges and transition channels between the electronic ground state (X^1A_1) and electronically excited states of ozone ([Steinfeld et al., 1987](#)). The Hartley bands occur in the UV region between 200 nm and 310 nm wavelength and arise from the $^1B_2 \leftarrow X^1A_1$ transition. The Huggins absorption bands have discrete vibrational structure between 310 nm and 370 nm ([Chance et al., 1997](#)), which corresponds to the $^2A_1 \leftarrow X^1A_1$ transition. The Chappuis continuum bands in the visible range cover wavelengths between 400 nm and 650 nm which partly overlap with the Wulf bands ranging from 600 nm to 1100 nm. Theoretically, the Chappuis bands are assigned to the 1B_1 state and the Wulf bands are assigned to the vibrationally allowed transitions of the

³ For transitions between two states with molecule configuration in the ground state (the orbital angular momentum along the molecular axis (Ω) is zero), the transition $\Delta J = 0$ is forbidden (e.g., [Thorne et al. \(1999\)](#)). Therefore, the ozone photolysis by the $O(^1S) + O_2(^1\Sigma_g^+)$ channel is not allowed.

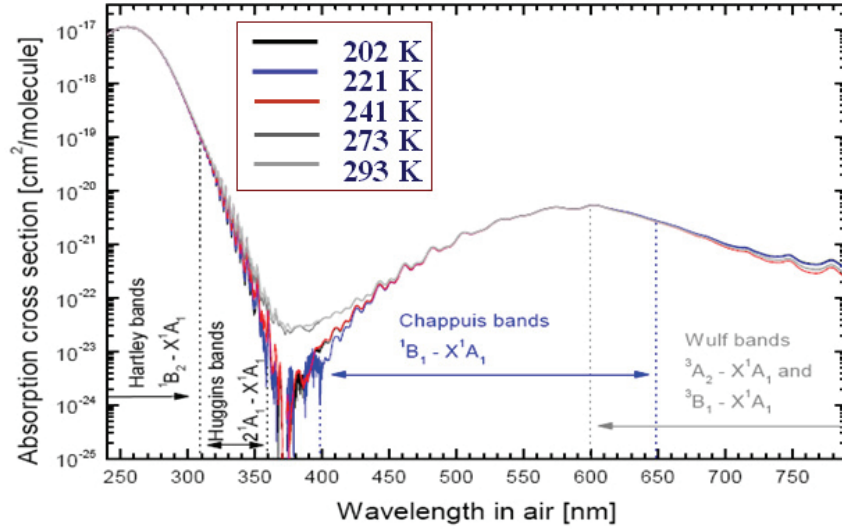


FIGURE 2.1: The temperature dependence of the ozone absorption cross section in different spectral ranges measured with the GOME FM.

3A_2 and 3B_1 electronic states. The transition channels for each band are shown in Fig. 2.1 as well. As can be clearly seen in Fig. 2.1, the ozone cross-section increases with increasing temperature in the Huggins bands. The temperature dependence is negligible in the Hartley bands. The temperature dependence in the Chappuis bands is significant only between 370 and 500 nm and only a small variation of the ozone absorption cross sections for different temperatures is found around the peak of the Chappuis band (at ~ 600 nm). The temperature dependence is one of the criteria for selecting the ozone retrieval wavelengths in this study, which will be discussed in more detail in Section 4.4.

2.3 Dynamics and transport of stratospheric ozone

Most ozone molecules are generated in the tropical upper stratosphere where the largest mean intensity of ultraviolet radiation occurs causing photodissociation of oxygen and subsequent formation of ozone according to Chapman's mechanism. Thus one would expect the ozone concentration to be high in the tropics and correspondingly low in the polar regions. This assumption is not consistent with the actual ozone distribution. Naturally the total ozone columns are low in the tropics and increase toward the poles up to about 60° latitude. This is because dynamical processes play an important role altering the basic distribution of ozone in the stratosphere. A complete description of the atmospheric dynamical systems is beyond the scope of this present thesis. Only

the basic factors of the planetary circulation and dynamical processes governing the diabatic ozone descent in the polar regions are described here. More detail descriptions are given by, e.g., [Holton \(1992\)](#) and [Brasseur and Solomon \(2005\)](#).

The transport of ozone from the tropics to higher latitudes is largely explained by the meridional residual circulation also referred to as the Brewer-Dobson (BD) circulation. [Dobson et al. \(1930\)](#) inferred the existence of a large-scale stratosphere circulation cell characterized by rising motion in the tropics followed by descending poleward motion based on the latitude gradients in ozone observations. [Brewer \(1949\)](#) found a similar motion based on the water vapour observations. This meridional circulation is driven dynamically by planetary waves and is more efficient in the winter hemisphere, while the meridional circulation in the summer hemisphere is much weaker (e.g., [Randel and Wu, 1999](#); [Weber et al., 2003](#)).

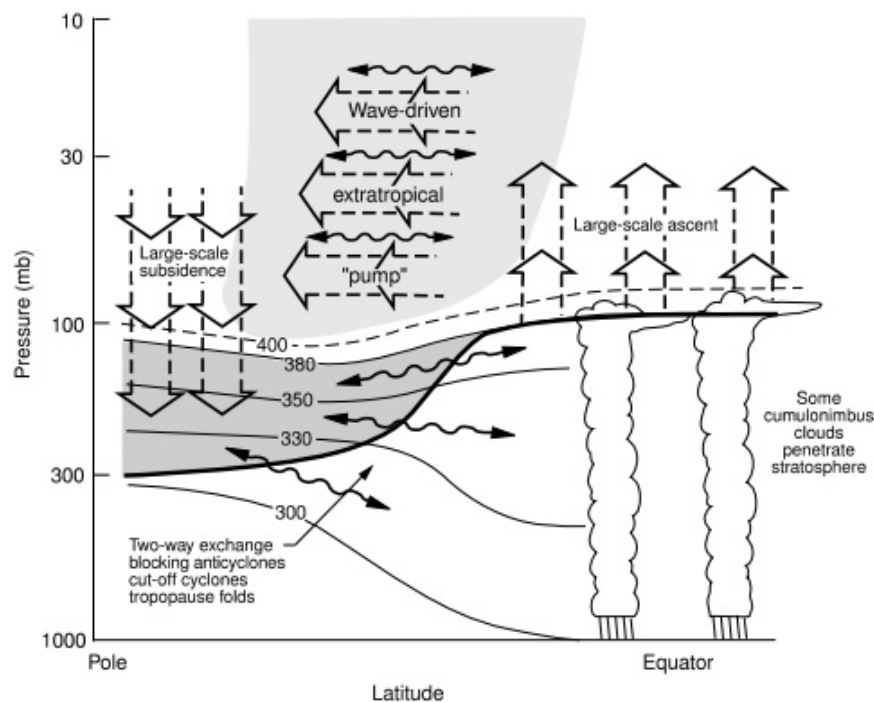


FIGURE 2.2: The large scale picture of planetary circulation (Fig. is taken from [Holton et al. \(1995\)](#)).

Fig. 2.2 shows the large-scale circulation of the atmosphere as a function of latitude and pressure level. The thick black line represents the mean tropopause. The tropopause is near 300 mb at the pole and 100 mb in the tropics. In the tropics, the strong solar radiation causes the formation of deep cumulonimbus clouds, which are able to penetrate the stratosphere. Due to the strong solar radiation in the tropical region, air masses are

heated and rise. At the same time, due to lack of sunlight, a cooling above the winter pole occurs, and large-scale sinking takes place. The tropical air masses are directed upward in the summer hemisphere and downward in the winter hemisphere by the wave-driven extratropical pump mechanism. In addition, air masses can be also transported across the tropopause at middle latitudes in the lowermost stratosphere (dark-grey area in Fig. 2.2), which is referred to as Stratospheric-Tropospheric Exchange (STE). The STE is governed by smaller scale extratropical processes, such as blocking anticyclones, cut-off lows and tropopause folds, to control the rate of air mass transport between troposphere and stratosphere (e.g. Wirth, 1995; Olsen et al., 2004; Dethof et al., 2000).

One of wave driven phenomena influencing stratospheric ozone is the Quasi-Biennial Oscillation (QBO). The QBO is a reversal of the tropical wind in the lower stratosphere (below 35 km) from easterly to westerly⁴ which has a regular cycle averaged period of 26–30 months. The QBO not only affects airmasses in the equatorial lower stratosphere, but also affects airmasses of mid- and high latitudes up to the winter pole. This phenomenon influences dynamical features of the polar vortex and indirectly causes changes of ozone distributions at the middle and high latitudes. In general, the westerly QBO phase leads to a colder and more stable the polar vortex than the easterly QBO phase (Wayne, 2000). The planetary circulation and dynamic processes above illustrate the vertical motion of air masses which is related to the diabatic descent of ozone in the winter polar stratosphere and the stratospheric ozone distribution.

2.3.1 Diabatic ozone descent

The changes of the ozone mixing ratio in the polar stratosphere is commonly attributed to two causes: (i) chemical processes, and (ii) diabatic ozone descent or ascent dynamics, which can be written as:

$$\left. \frac{dO_3}{dt} \right|_{\Theta} = \frac{\partial O_3^c}{\partial t} + \frac{\partial O_3^d}{\partial t}. \quad (2.34)$$

Eq. 2.34 considers the change of the ozone mixing ratio at an isentropic level Θ ⁵. The

⁴ The easterly wind is the equatorial lower stratosphere wind from the east to west and the westerly wind is vice-versa.

⁵ Θ is the potential temperature. It is defined as $\Theta = T \left\{ \frac{p_0}{p} \right\}^{\frac{R}{c_p}}$, where R is the ideal gas constant for dry air, c_p is the specific heat at constant pressure, T is the temperature, and p_0 is the reference pressure at ground level.

adiabatic descent of air masses leads to temperature changes which can occur in the form of adiabatic heating. The vertical ozone change at an isentropic level by diabatic descent can be determined by the dependence of the potential temperature (Θ) and the change of temperature (T) in time as follows:

$$\left. \frac{\partial O_3^d}{\partial t} \right|_{\Theta} = \frac{\partial O_3}{\partial \Theta} \frac{\partial \Theta}{\partial T} \frac{\partial T}{\partial t} \quad (2.35)$$

where $\partial O_3/\partial \Theta$ is the derivative of vertical ozone with respect to the potential temperature (Θ). The temperature change is directly proportional to the diabatic heating or cooling rate, $Q = -\partial T/\partial t$. Therefore, the vertical ozone changes on an isentropic surface can be calculated in terms of radiative cooling or heating (e.g., Braathen et al., 1994; Sinnhuber et al., 1998; Eichmann et al., 2002) as follows:

$$\frac{\partial O_3^d}{\partial t} = Q \left(\frac{p_0}{p} \right)^{\kappa} \frac{\partial O_3}{\partial \Theta} \quad (2.36)$$

where p and p_0 are pressure at isentropic level and surface pressure, respectively, and $\kappa = 2/7$ is the ratio of dry air gas constant and the specific heat at constant pressure. Due to the short wavelength absorption of solar radiation, the diabatic heating or cooling rate can be also determined from the derivative of irradiance solar radiation (F) with respect to altitude changes:

$$Q = \frac{1}{\rho c_p} \frac{dF}{dz} \quad (2.37)$$

where ρ is the air density (cm^{-3}) and c_p is the specific heat capacity at constant pressure ($JK^{-1}kg^{-1}$). The solar irradiance F is the incident of solar radiance (I) on a surface intergrating over the solid angle.

$$F = \int_0^{2\pi} I_{\lambda} \mu d\Omega \quad (2.38)$$

where μ is cosine of the solar zenith angle and Ω is the solid angle. The diabatic heating computation must include both the short wavelength absorption by ozone and the long wavelength absorption and emission by water vapor and carbon dioxide. In general, at

high latitude during winter, the infrared cooling is dominated by water vapor and carbon dioxide in the stratosphere (e.g., Rosenfield et al., 1994; Eluszkiewicz et al., 1996; Siskind et al., 1998; Jucks and Salawitch, 2000) leading to diabatic cooling followed by a descent of the air masses (i.e., the diabatic descent) and the solar heating from ozone absorption becomes weak. Both the Brewer-Dobson circulation as well as these thermodynamic processes typically lead to a descent of ozone-rich air into the lower polar stratosphere during winter, and have to be corrected for when estimating the chemical ozone loss in the polar vortex. More details about an appropriate radiative transfer model will be explained in chapter 6.

2.3.2 Potential vorticity as the polar vortex indicator

The potential vorticity (PV) is widely applied in atmospheric research and in particular as a diagnostic tool to describe the extent of the polar vortex.

The PV is the absolute circulation of an air parcel that is enclosed between two isentropic surfaces. The PV value of an air parcel is conserved in the absence of friction and diabatic heating, i.e., on short enough timescales, on the order of days. That means that the potential temperature difference between two isentropic surfaces of an air parcel is conserved along the parcel's trajectory.

The PV can be written in the form of Ertel's potential vorticity as follows:

$$PV = -g(f + \xi) \frac{\partial \Theta}{\partial p} \quad (2.39)$$

where g is the gravitational acceleration, p is pressure, ξ is the relative isentropic vorticity, f is the Coriolis parameter, and Θ is the potential temperature.

The sum $f + \xi$ is called the absolute vorticity. It represents the spin of the planetary vorticity which is represented by the Coriolis parameter f and a contribution from the air parcels motion relative to a coordinate system fixed to the Earth, ξ , which is called relative vorticity. The Coriolis parameter is defined as $f = 2\Omega \sin \Phi$ where Ω is the angular velocity of the Earth's rotation and Φ is the latitude of the point considered. f is on the order of $\sim 10^{-4} s^{-1}$ except near the equator. The relative vorticity can be calculated from:

$$\xi = \frac{1}{a \cos \Phi} \frac{\partial v}{\partial \lambda} - \frac{1}{a \cos \Phi} \frac{\partial (u \cos \Phi)}{\partial \Phi} \quad (2.40)$$

where u is the zonal wind speed (u wind), measured towards the east, v is the meridional wind velocity (v wind), measured towards the north, Φ is the latitude, λ is longitude and a is the Earth's radius.

The potential vorticity is often expressed in $10^{-6}m^2s^{-1}Kkg^{-1}$, referred to as 1 PVU (Holton, 1992). Eq. 2.39 is defined with a minus sign so that its value is positive in the northern hemisphere and negative in the southern hemisphere. The potential vorticity increases rapidly from the troposphere to the stratosphere due to the significant change of the static stability. Typical changes of the potential vorticity within the area of the tropopause are from 1 PVU for the tropospheric air to 4 PVU for the stratospheric air. The PV value is used as an indicator of the vortex. The spacing of PV contours is very wide in the midlatitudes, very tight at the polar vortex edge, and then widens again inside of the vortex. The edge of the vortex is defined to be where the contours of PV are closest together. The area inside of this edge can be determined as the area of the polar vortex.

In Eq. 2.39, the change of potential temperature with pressure level ($\frac{\partial\Theta}{\partial p}$) follows a steep gradient in the atmosphere which leads to an exponential increase of PV with height. Lait (1994) proposed a Modified Potential Vorticity (MPV) defined as Ertels potential vorticity multiplied by a scaling factor $\{\frac{\Theta}{\Theta_0}\}^{9/2}$, where Θ_0 is a constant to make the scaling factor dimensionless.

$$MPV = PV \left\{ \frac{\Theta}{\Theta_0} \right\}^{-\frac{9}{2}} \quad (2.41)$$

This scaling describes the vertical gradient of Θ for an isothermal atmosphere. It is suitable for inspecting vertical cross sections of PV and removes much of the altitude dependence without destroying the structure of PV on a given isentropic surface. Moreover, this scaling preserves both the unit and the conservation properties of PV (Müller and Günther, 2003). The MPV will be used for the investigations in chapter 6 and the Θ_0 is set to 475 K in the calculation.

Chapter 3

SCIAMACHY

3.1 The SCIAMACHY instrument

The Scanning Imaging Absorption SpectroMeter for Atmospheric CartographY (SCIAMACHY) instrument on board the European Environment Satellite (ENVISAT) was launched on 1 March, 2002 on a Ariane-5 rocket from Kourou in French Guiana. The ENVISAT satellite is a near polar sun-synchronous orbit at 799.8 km mean altitude with an inclination angle of 98.55° crossing the equator at 10 a.m. local time in descending node. ENVISAT's orbital period is 100.6 min per orbit resulting in $14\frac{11}{35}$ orbits per day, and it achieves full global coverage in 6 days, and has a ground track repeat cycle of 35 days, i.e., 501 orbits.

SCIAMACHY is a multi-national contribution of Germany, The Netherlands, and Belgium. The SCIAMACHY is an eight-channel passive imaging grating spectrometer instrument. It can measure the reflected, backscattered and transmitted solar radiation upwelling from the top of the atmosphere in the UV-SWIR range between 214 nm and 2386 nm with a spectral resolution varying between 0.24 nm and 1.48 nm (e.g., [Goede et al., 1991](#); [Burrows et al., 1995](#); [Bovensmann et al., 1999](#); [Gottwald et al., 2006](#)).

3.2 SCIAMACHY measurement geometries

The SCIAMACHY measures radiance in three different geometries. The daylight measurements can be performed in the limb and nadir viewing geometries and also in occultation mode by atmospheric transmission of solar and lunar light. Each geometry has its particular advantage.

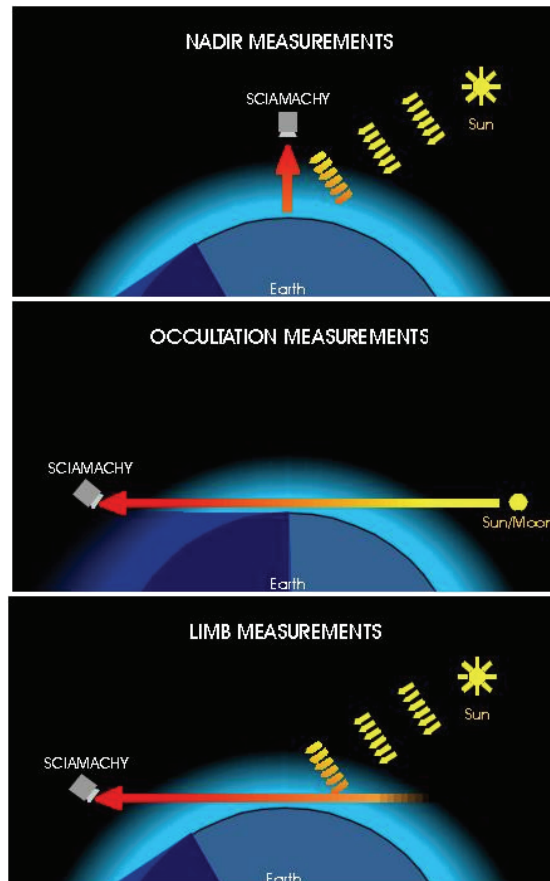


FIGURE 3.1: Schematics of the three different viewing geometries of the SCIAMACHY instrument. (Courtesy of S. Noël, IUP, Bremen)

3.2.1 The nadir viewing geometry

The field of view of the nadir mode faces downward to the Earth's surface, thus the atmospheric column can be directly measured scanning across the sub-satellite track. The nadir mirror scans with a field of view of $25 \text{ km} \times 0.6 \text{ km}$ across the satellite track. The spatial resolution of the scan mode depends on the scan velocity and the integration time of the detectors. The scan velocity along track is determined by the satellite velocity of approximately 7.5 km s^{-1} , and the across track velocity is determined by the

nadir scan mirror rate of approximately 240 km s^{-1} on ground. Thus, the typical spatial resolution is approximately 240 km across track and 30 km along track (see also figure 3.2).

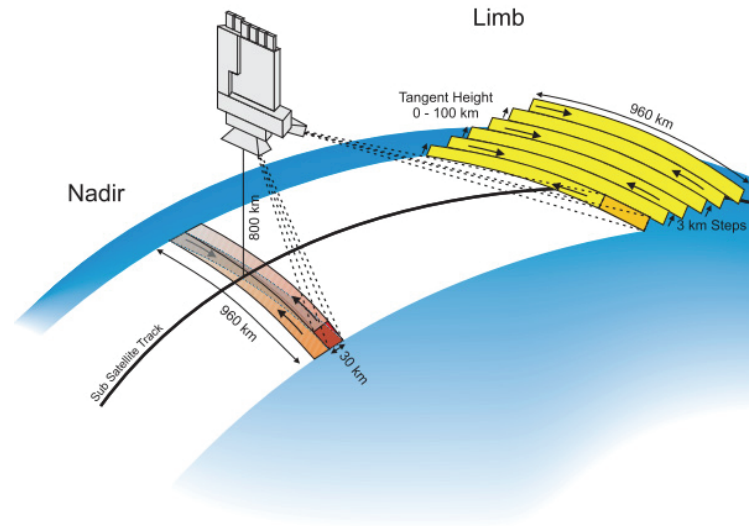


FIGURE 3.2: Illustration of the limb and nadir viewing geometries of the SCIAMACHY instrument. (Courtesy of S. Noël, IUP, Bremen)

3.2.2 The occultation viewing geometry

In occultation mode, SCIAMACHY faces directly to the Sun or the Moon. The solar occultation is performed during sunrise. The lunar occultation is performed during the period from half Moon to full Moon at a fixed azimuthal mirror position. The lunar occultation measurements are performed in the southern hemisphere, between 30° and 90° latitude, during local nighttime. The lunar observations are in principle also possible in the northern hemisphere but these events usually coincide with sunrise. The field of view of occultation measurements is about 30 km in azimuthal and about 2.5 km in elevation direction at the tangent point. The spatial resolution depends on the integration time of 62 ms for solar occultation measurements and about 1 s for lunar occultation measurements.

3.2.3 The limb viewing geometry

In limb mode SCIAMACHY measures the scattered solar radiation above the horizon as a function of tangent height allowing the determination of trace gas profiles. SCIAMACHY's limb mode is a powerful technique to observe the atmosphere with global

coverage and high vertical resolution. In the limb viewing geometry the SCIAMACHY instrument observes the atmosphere in elevation steps of about 3.3 km at each tangent height and then scanning vertically up to the top of the atmosphere (about 100 km tangent height). The field of view is 110 km \times 2.6 km at the tangent point. A typical azimuthal scan resolution (horizontal cross-track) is about 240 km for an integration time of 0.375 s and about 960 km in a wide swath for all the azimuthal scans (see figure 3.2).

Satellite observations of the scattered solar radiation in limb viewing geometry have become one of the standard techniques to measure stratospheric profiles of ozone and other minor constituents (e.g., [McPeters et al., 2000](#); [von Savigny et al., 2003](#); [Haley et al., 2004](#); [Rault, 2005](#)). In limb mode SCIAMACHY observes solar photons scattered in the atmosphere and reflected by the surface. Every single photon takes a different path through the atmosphere. The limb-scatter observation geometry is characterized by a complex radiative transfer, because the multiple scattering or diffuse radiation contribution to the observed limb radiances can be significant ([Oikarinen et al., 1999](#)), and because the sphericity of the atmosphere cannot be neglected. Furthermore, the underlying surface, which may contribute significantly to the diffuse illumination of the sensed air volumes, is not observed directly. This geometry is strongly affected by surface albedo and clouds, especially in the spectral ranges with small gaseous absorption. The effect of tropospheric clouds on the ozone retrievals will be comprehensively described in chapter 5.

A typical orbit starts with a limb measurement of the twilight atmosphere, followed by the solar occultation measurement during sunrise over the north pole and an optimized limb-nadir sequence. If the moon is visible in the southern hemisphere (30°-90°S), lunar occultation measurements are performed every second orbit.

The solar illumination of the atmosphere experiences a seasonal variation. Because limb-scatter measurements are only possible on the day side of Earth, the range of latitudes observable on a given day also changes with season. Some part of the southern hemisphere is in the darkness between around the spring equinox (March) and the autumn equinox (September) with the largest effect around summer solstice (June). Undoubtedly, the dark period also occurs for the northern hemisphere between around the autumn equinox and the spring equinox which the largest effect around winter solstice (December). The orientation of the Envisat orbit plane throughout a year is shown in Fig. 3.3. An example of the geographical coverage of SCIAMACHY limb measurements as a function of month is shown in Fig. 3.4. These locations, data are taken from

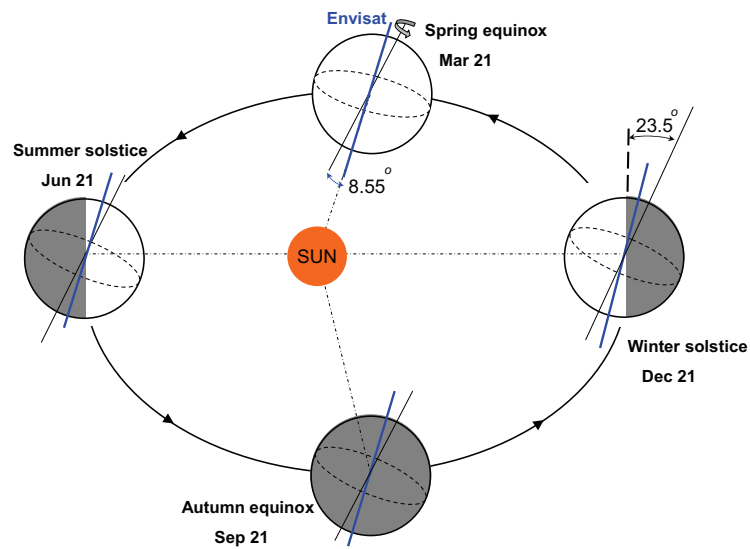


FIGURE 3.3: Orientation of the Envisat orbit plane throughout a year (not to scale and modified from von Savigny (2002)).

the SCIAMACHY limb observations in 2008. As can be seen SCIAMACHY limb measurement do not cover the polar regions during the winter months in each hemisphere.

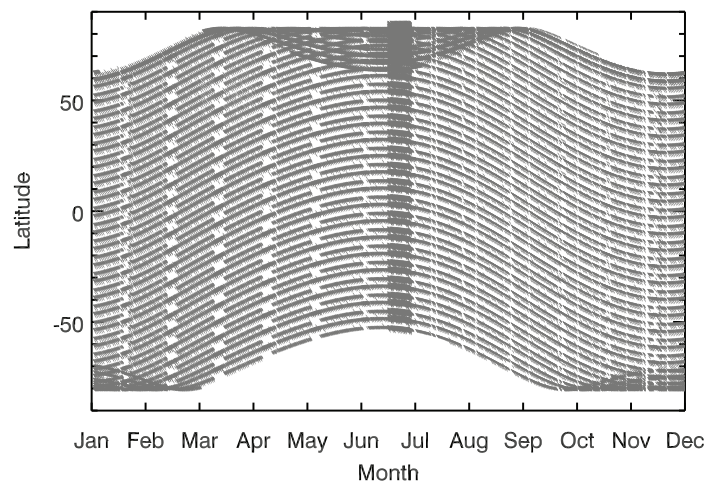


FIGURE 3.4: Latitudinal coverage of SCIAMACHY limb observations as a function of the month.

3.3 The optical configuration of the SCIAMACHY instrument

Figure 3.5 shows the optical setup of SCIAMACHY which collects solar radiation to generate the spectral information. For all measurements, the incoming radiation falls on to the elevation mirror followed by a telescope. Passing the entrance slit, the light is focussed on a pre-disperser prism, weakly dispersing the light and directing fully polarised light into the Polarisation Measurement Device (PMD) which can monitor the polarization of the incident radiation at high spatial resolution. The reflected light is separated depending on the spectral range, using reflective optics and dichroic mirrors. The shorter wavelengths are reflected to UV channels 1 and 2 which are located in level 1 facing in the flight direction (top panel of Fig. 3.5). The longer wavelength channels are located in level 2 (bottom panel of Fig. 3.5) with the visible and near-infrared spectral ranges being reflected to channels 3 to 6. The infrared part of the spectrum is reflected toward channels 7 and 8. Each individual channel has a grating, transmission optics and a diode array detector of the appropriate material. In channels 1 – 5, the detectors are silicon monolithic diode arrays, whereas InGaAs detectors are used for channels 6 – 8 instead because the band gap of silicon is too large to be utilised for detectors in this spectral range. In order to be sensitive to wavelengths beyond 1700 nm, the detector material in the upper part of channel 6 (named channel 6+) and channels 7 – 8 were made with higher amounts of Indium (Gottwald et al., 2006). The SCIAMACHY is able to record a wide spectral range hence the different trace gases can be observed simultaneously. See Table 3.1 for an overview of SCIAMACHY spectral channels including the list of molecules which can be measured with SCIAMACHY.

TABLE 3.1: Overview of the SCIAMACHY spectrometer channels.

Channels	Spectral range (nm)	Resolution (nm)	Detector material	Temperature range (K)	Retrieval targets
1	214-334	0.24	Si	204.5-210.5	O ₃ , ClO, NO, Metals, Noctilucent clouds
2	300-412	0.26	Si	204.0-210.0	NO ₂ , OClO, BrO
3	383-628	0.44	Si	221.8-227.8	O ₃ , NO ₂ , O ₄ , Aerosols
4	595-812	0.48	Si	222.9-224.3	O ₃ , NO ₃ , H ₂ O, Aerosols
5	773-1063	0.54	Si	221.4-222.4	H ₂ O, Aerosols
6	971-1773	1.48	InGaAs	197.0-203.8	H ₂ O, Aerosols
7	1934-2044	0.22	InGaAs	145.9-155.9	H ₂ O, CO ₂
8	2259-2386	0.26	InGaAs	143.5-150.0	H ₂ O, CO ₂ , CO

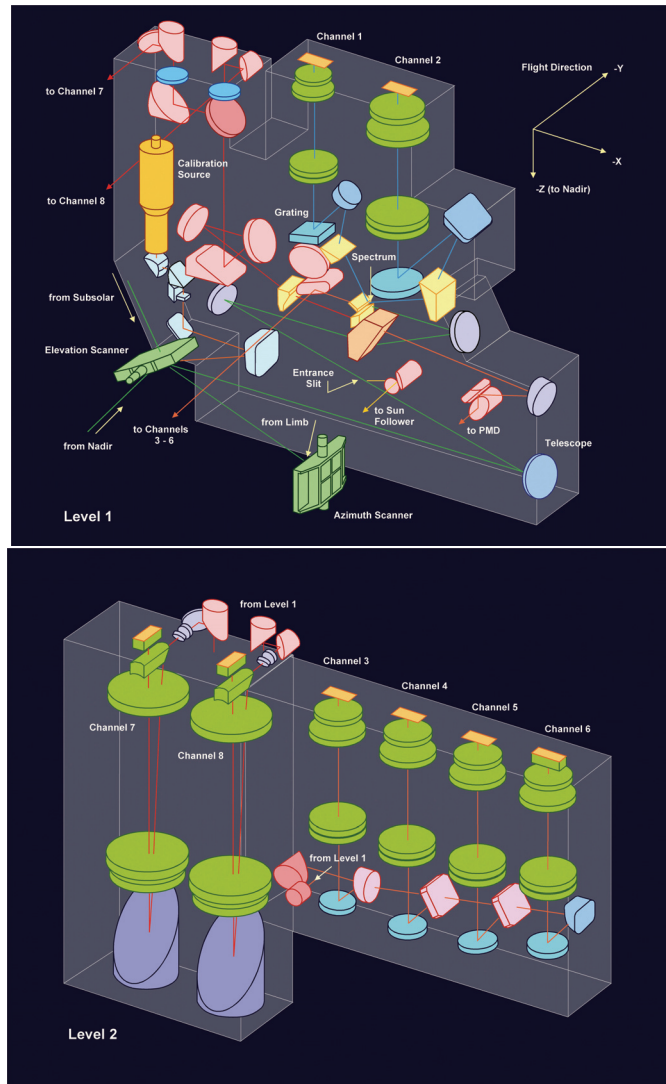


FIGURE 3.5: The optical configuration of SCIAMACHY, (Graphics courtesy of DLR-IMF).

Chapter 4

Radiative transfer and the ozone retrieval algorithm

The ozone profile retrieval requires the use of a radiative transfer model (RTM) – the so-called forward model – modelling the radiation field associated with a specific ozone profile and a set of other relevant parameters (e.g., background density profile, surface albedo, etc.). Radiative transfer models solve the radiative transfer equation (RTE) using one of several established numerical approaches. Therefore, a short description of the radiative transfer equation for the atmosphere is given in the section 4.1. The inverse method and optimal estimation concepts are briefly reviewed in the section 4.2. The SCIATRAN software package, comprised of a radiative transfer code and a retrieval algorithm, is introduced in section 4.3. Section 4.4 presents the ozone retrieval methodology implemented in SCIATRAN for retrieving the vertical ozone concentration profiles. Some results of the retrieved ozone profiles from SCIAMACHY limb measurements and the agreement with the other instruments are shown in the last section.

4.1 Radiative transfer in the atmosphere

The solar radiation that we receive at the Earth's surface is intercepted by the Earth's atmosphere. The solar radiation does not totally reach to the Earth's surface. It is absorbed, reflected or backscattered by the atmospheric processes. The changes in the solar intensity radiation (I) as it passes through an absorbing and scattering medium can be written in radiative transfer equation (Rozanov, 2001).

$$\frac{dI}{ds} = -\alpha(I - J). \quad (4.1)$$

The α term is the extinction coefficient for all the scattering and absorption processes. The J term is the source function given by the following expression.

$$J = \frac{\omega_0}{4\pi} \oint \Phi(\gamma) I(\Omega') d\Omega'. \quad (4.2)$$

Ω' is the scattered solid angle, ω_0 is the single scattering albedo to describes the contribution of scattering and extinction coefficients,

$$\omega_0 = \frac{\sigma}{\alpha} \in [0, 1]. \quad (4.3)$$

σ is the scattering coefficient. $\Phi(\gamma)$ is the phase function which is normalized as follows:

$$\int \Phi(\gamma) \frac{d\Omega}{4\pi} = 1, \quad (4.4)$$

with $d\Omega = 2\pi \sin\gamma d\gamma$, and γ representing the angle between incident and scattered radiation.

The solar radiation can be split into two components: the direct radiation (I_{dir}), which is never scattered in the atmosphere or reflected from the Earth's surface, and the diffuse radiation (I_{dif}), which is scattered or reflected at least once. The net radiation can be written as

$$I = I_{dif} + I_{dir}. \quad (4.5)$$

Therefore, Eq. 4.1 can be written as:

$$\frac{dI}{ds} = -\alpha(I_{dif} + I_{dir} - J). \quad (4.6)$$

The changes in radiative transfer equation for the direct radiation is the homogeneous differential equation,

$$\frac{dI_{dir}}{ds} = -\alpha(I_{dir}), \quad (4.7)$$

having the formal solution which is known as Lambert-Beer's law:

$$I_{dir} = F_0 e^{-\int \alpha(s) ds} \quad (4.8)$$

where F_0 is the incident solar flux.

The exponential attenuation of incoming radiation is due to the extinction by the atmospheric medium as shown in the integral term of Eq. 4.8. This term is also called the optical depth (τ).

The diffuse radiation can be explained by the radiative transfer equation including the source term J in Eq. 4.9 to determine the changes in the specific radiance I_{dif} through an absorbing and emitting medium in the pathlength ds .

$$\frac{dI_{dif}}{ds} = -\alpha(I_{dif} - J). \quad (4.9)$$

The source term in Eq. 4.2 can be reformed as follows,

$$J = \frac{\omega_0}{4\pi} \oint \Phi(\gamma) I_{dif}(\Omega') d\Omega' + \frac{\omega_0}{4\pi} F_0 \Phi(\gamma) e^{-\int \alpha(s) ds}. \quad (4.10)$$

The first term of Eq. 4.10 is the source function from multiple scattering (J_{ms}) and the second term represents the single scattering contribution (J_{ss}). Therefore, Eq. 4.9 can be rewritten in the general form as follows:

$$\frac{dI_{dif}}{ds} = -\alpha(I_{dif} - J_{ms} - J_{ss}) \quad (4.11)$$

The analytical and computational methods to solve the radiative transfer equation are discussed in detail by [Lenoble \(1985\)](#).

4.2 Inverse method and optimal estimation

Retrieving profile information on atmospheric minor constituents from remote sensing observation is a difficult task. Often the inverse problem is formally ill-posed, i.e., it has no mathematically unique solution. Therefore, an optimal estimation approach is used to find the appropriate criteria which determine the best solution from all the possible

ones which are consistent with the observation. It is helpful to separate the problem into two parts. Firstly, the inverse method is used to find a simplified solution. Secondly, the optimal estimation method is applied to iteratively find the best retrieval profile.

In this section, the mathematics of the inverse method and optimal estimation solving for an atmospheric parameter is briefly introduced. The comprehensive details on this method are described in [Rodgers \(1971, 1976, 1990, 1998, 2000\)](#).

Sometimes the remote sensing retrieval problem is linear,

$$y = Ax + \epsilon. \quad (4.12)$$

y is the m -element measurement vector with measurement error ϵ . x is an n -element vector containing the quantities to be retrieved, where n has to be chosen adequately to represent the possible atmospheric variations. x is also called “state vector”. A is a forward model operator to characterize the dependence of the measurement y on the state vector x . The solution can be statistically evaluated using *a priori* information to be the typical ozone distributions, i.e. state vector x_0 . For evaluating information content, the nonlinear problem can be written as a generalization of the linear problem (Eq. 4.12) using a Taylor series expansion of the forward model operator A in form of the linear forward model operator K_0 .

$$Ax \simeq Ax_0 + \frac{\delta A}{\delta x}(x - x_0) \quad (4.13)$$

$$y \simeq y_0 + K_0(x - x_0). \quad (4.14)$$

As shown in 4.13, the operator $K_0 = \frac{\delta A}{\delta x}$ also describes the sensitivity of the measurements to changes in the state and is determined by perturbation of each state vector quantity. K_0 is called weighting function matrix. To yield an optimized solution in the linear inverse problem, the following condition has to be minimized:

$$\|(y - y_0) - K_0(x - x_0)\|^2 S_y^{-1} + \|(x - x_0)\|^2 S_a^{-1} \rightarrow Min \quad (4.15)$$

where S_a is the *a priori* covariance matrix and S_y is the covariance matrix of the measurement error. The off-diagonal elements of S_y are set to zero, that is the measurement errors at different wavelengths are assumed to be uncorrelated. Through the minimization in Eq. 4.15, the retrieval solution can be obtained:

$$x = x_0 + (K_0^T S_y^{-1} K_0 + S_a^{-1})^{-1} K_0^T S_y^{-1} (y - y_0) \quad (4.16)$$

Since the problem is a non-linear function, the first retrieval solution is not accurate enough. The retrieval solution has to be solved by using the Newtonian iteration method, that linearizes the problem and evaluates the linearized solution iteratively. The optimal estimation result at iteration step $i + 1$ can be written as

$$x_{i+1} = x_0 + (K_i^T S_y^{-1} K_i + S_a^{-1})^{-1} K_i^T S_y^{-1} (y - y_i + K_i(x_i - x_0)) \quad (4.17)$$

After convergence has occurred according to a chosen convergence criterion in the last iteration, the retrieval solution, \hat{x} , is evaluated. The retrieved state covariance matrix in the last iteration step is given by Rodgers [1976] as follow:

$$\hat{S} = (\hat{K}^T S_y^{-1} \hat{K} + S_a^{-1})^{-1} \quad (4.18)$$

\hat{S} describes the error due to the measurement noise (\hat{S}_n) and the smoothing error caused by using the *a priori* information (\hat{S}_s), which is regarded as the covariance of a climatology, see, for example in Hoogen et al. (1999). The explanation of \hat{S}_n and \hat{S}_s can be found in Rodgers (1990). The retrieval errors of the state vector elements are correlated which is rather difficult to visualize. The common practice is to use the standard deviations, i.e., the square roots of the diagonal elements of \hat{S} to assign error bars of the solution. The *a priori* covariances are approximated as follow:

$$S_a^{l'l''} = \sigma_{a,l'} \sigma_{a,l''} \exp\left(-\frac{\|r_{l'} - r_{l''}\|}{r_c}\right) \quad (4.19)$$

where $\sigma_{a,l'}$ and $\sigma_{a,l''}$ correspond to the variances at altitude l' and l'' respectively. r_c is the correlation radius which is set to 1.5 km over the whole atmosphere.

A very important diagnostic tool is the averaging kernel matrix (\hat{A}) which represents the change of the retrieved state \hat{x} with respect to the true state x_t :

$$\hat{A} = \frac{\delta \hat{x}}{\delta x_t}. \quad (4.20)$$

The width of the averaging kernels are a measure for the vertical resolution of the retrieval. Furthermore, the trace of \hat{A} corresponds to the number of degrees of freedom of the solution. Following Rodgers [1990], the \hat{A} can be written for the optimal estimation in algebraic form:

$$\hat{A} = (K_i^T S_y^{-1} K_i + S_a^{-1})^{-1} K_i^T S_y^{-1} \hat{K}. \quad (4.21)$$

The retrieval solution, Eq. 4.17 can be expressed in \hat{A} as follow:

$$\hat{x} = x_0 + \hat{A}(x_t - x_0) \quad (4.22)$$

4.3 The SCIATRAN software

The software package SCIATRAN 2.2 (Rozanov et al., 2005b, Rozanov, 2008) incorporates the highly sophisticated and versatile radiative transfer model and the retrieval algorithm routinely run at the Institute of Environmental Physics of the University of Bremen in order to analyze SCIAMACHY limb, nadir and occultation observations.

The SCIATRAN software package has been validated with respect to other radiative transfer codes (Kurosu et al., 1997; Loughman et al., 2004; Hendrick et al., 2006; Wagner et al., 2007) and successfully employed to retrieve atmospheric trace gases from measurements of scattered solar radiation in the Earth's atmosphere by satellite, ground-based, or airborne measurements in UV-Vis-NIR spectral region. SCIATRAN was successfully employed to retrieve vertical profiles of atmospheric trace gases from measurements of the scattered solar radiation performed by the SCIAMACHY instrument in limb viewing geometry (Bracher et al., 2005; Rozanov et al., 2005a; von Savigny et al., 2005b; Butz et al., 2006; Rozanov et al., 2007). In this study, the SCIATRAN code was extended and optimized to retrieve the vertical distributions of ozone in the stratosphere and the lower mesosphere from SCIAMACHY limb observations.

The forward modeling is performed in an approximative spherical mode employing the combined differential-integral (CDI) approach (Rozanov et al., 2001). With this approach the outgoing radiance is calculated integrating the contributions from both single and multiple scattering along the instrument line of sight intersecting a spherical shell atmosphere. The singly scattered solar radiation is considered fully spherically whereas the multiple scattering contribution is approximated for each point at the line

of sight solving the pseudo-spherical radiative transfer equation for the proper atmospheric location and illumination. The pseudo-spherical solution is obtained employing the discrete-ordinate method similar to that described by [Siewert \(2000\)](#). The weighting functions are calculated employing the forward-adjoint technique as described by [Roazanov \(2006\)](#).

4.4 The ozone profile retrieval methodology

The vertical distribution of ozone number density in the Earth's atmosphere is commonly retrieved using limb-scatter measurements in the UV-Visible spectral range by exploiting the Hartley, Huggins, or Chappuis absorption bands. The Hartley bands in the UV have been employed by [Rusch et al. \(1983\)](#) to retrieve lower mesospheric ozone profiles from measurements with the UV spectrometer on SME (Solar Mesosphere Explorer). More recently, the Hartley bands were used by [Rohen et al. \(2006\)](#) to retrieve ozone profiles in the upper stratosphere and lower mesosphere from SCIAMACHY limb scatter measurements. Ozone absorption in the Huggins bands was exploited for profile retrievals from limb-scatter measurements with the Shuttle Ozone Limb Scattering Experiment/Limb Ozone Retrieval Experiment (SOLSE/LORE) flown on the space shuttle in 1997 and 2003 ([Flittner et al., 2000](#); [McPeters et al., 2000](#)). The Chappuis bands in the visible have been used by [Flittner et al. \(2000\)](#), [McPeters et al. \(2000\)](#), [von Savigny et al. \(2003\)](#), [Haley et al. \(2004\)](#), [Rault \(2005\)](#), [Roazanov et al. \(2007\)](#) and [Roth et al. \(2007\)](#) to retrieve ozone profiles in the stratosphere from measurements with SOLSE/LORE, the Optical Spectrograph and InfraRed Imager System (OSIRIS) on Odin, the Stratospheric Aerosol and Gas Experiment (SAGE III) on Meteor-3, and SCIAMACHY. In this study, we combine the observations in the Hartley and Chappuis absorption bands to retrieve the vertical distributions of ozone in both the stratosphere and the lower mesosphere. A similar approach was recently applied to OSIRIS limb scatter measurements ([Degenstein et al., 2009](#)), combining spectral information from the Hartley, Huggins and Chappuis bands in a simultaneous ozone profile retrieval. Furthermore, [Tukiainen et al. \(2008\)](#) recently presented retrievals of ozone profiles (and several other atmospheric parameters) from OSIRIS limb scatter observations that also combined spectral information from the UV and visible ozone absorption bands.

In the Hartley absorption band, where the measured limb radiance is mostly sensitive to the ozone amount in the 35 – 70 km altitude range, a discrete set of wavelengths is

selected similarly to Rohen et al. (2006) avoiding Fraunhofer lines and dayglow emissions, namely, 264, 267.5, 273.5, 283, 286, 288, 290, and 305 nm. The UV wavelengths are measured in SCIAMACHY channels 1 and 2. To increase the signal to noise ratio the limb radiance is averaged over 2 nm spectral intervals around each central wavelength. The UV wavelength set used in this study is somewhat smaller as compared to Rohen et al. (2006), in particular, we have skipped the three shortest (250, 252, and 254 nm) and the two longest (307 and 310 nm) wavelengths. The former do not change the information content of the entire data set much and are strongly noise-contaminated whereas the latter are substantially affected by the multiple scattering and surface reflection. To reduce the impact of instrument calibration errors as well as of light scattering in the lower atmospheric layers, the limb radiance profiles at each wavelength are normalized by the limb radiance measured at an upper tangent height which is commonly referred to as the reference tangent height:

$$I_N(\lambda_k, h_i) = \frac{I(\lambda_k, h_i)}{I(\lambda_k, h_r)}. \quad (4.23)$$

Here, $I(\lambda_k, h_i)$ and $I(\lambda_k, h_r)$ denote the limb radiance at 8 wavelengths listed above, $\lambda_k, k \in \{1, \dots, 8\}$ at the current, h_i , and the reference, h_r , tangent heights, respectively. At each wavelength only limb radiances observed in a selected tangent height range are used. Table 4.1 shows the lowest, h_{low} , and the reference, h_r , tangent heights for each wavelength whereas the highest tangent height is always defined by the uppermost tangent height below the reference.

TABLE 4.1: The lowest (h_{low}) and reference (h_r) tangent heights for the wavelengths used.

Wavelength (nm)	264	267.5	273.5	283	286	288	290	305	525	602	675
h_{low} (km)	52	52	52	45	45	45	45	35	9	9	9
h_r (km)	71	71	71	68	65	65	61	55	41	41	41

The spectral information obtained in the visible spectral range is treated employing the triplet approach following Flittner et al. (2000) and von Savigny et al. (2003) which exploits the limb radiance profiles at three wavelengths: $\lambda_1 = 525$ nm at a relatively weak ozone absorption in the short-wavelength wing of the Chappuis band, $\lambda_2 = 602$ nm at a strong ozone absorption near the center of the Chappuis band, and $\lambda_3 = 675$ nm at a weaker ozone absorption in Chappuis bands. The Chappuis band wavelengths are measured in channels 3 and 4 of SCIAMACHY. Similarly to the UV wavelengths the limb radiance is averaged over 2 nm spectral intervals around each central wavelength

and normalized by the limb radiance at the reference tangent height. The lowest, h_{low} , and the reference, h_r , tangent heights for the visible wavelengths are also listed in Table 4.1. Furthermore, the normalized limb radiance profiles are combined resulting in the so-called Chappuis triplet:

$$I_{Ch}(h_i) = \frac{I_N(\lambda_2, h_i)}{\sqrt{I_N(\lambda_1, h_i) I_N(\lambda_3, h_i)}}. \quad (4.24)$$

Both the normalized limb radiances at UV wavelengths and the Chappuis triplet as given by Eqs. (4.23) and (4.24), respectively, will be denoted further as $y(h_i)$.

Employing the SCIATRAN radiative transfer model, the limb radiance profiles for the considered wavelengths and tangent height ranges are determined as required by the inversion routine. The *a priori* profile required for the optimal estimation retrieval is used to be the first guess in the forward model to evaluate the retrieval vector. The *a priori* ozone volume mixing ratios are taken from the climatology provided by Prather and Remsberg (1993) containing monthly and latitudinally dependent, ozone profiles, as well as pressure and temperature vertical distributions. The diagonal elements of the *a priori* covariance matrix are set to standard deviations of 1000 % to ensure that the retrieval is completely independent to the *a priori* information. The off-diagonal elements of the *a priori* covariance matrix are determined assuming a correlation length of 1.5 km over the whole atmosphere. The diagonal elements of the measurement covariance matrix are calculated from the squares of the measured radiance random errors.

4.5 Ozone profile retrieval results

For this study, version 2.0 of the ozone profile data set retrieved since August, 2002 from SCIAMACHY limb-scatter observations at IUP Bremen is employed. This data product provides the vertical variation of ozone concentration (in molecules cm^{-3}) on a regular 1 km altitude grid. It should also be noted that SCIAMACHY Level 1 version 6.03 data is used as a basis for the analysis in this study including the most recent tangent height correction scheme. An example of the ozone profile data product presented here is provided as monthly averages and shown in Fig. 4.1. In this figure, the monthly averaged ozone in 2003, 2005, 2006 and 2007 during January (northern winter and southern summer), April (northern spring and southern autumn), August (northern summer and southern winter), and October (northern autumn and southern spring) were selected in the regions of the Arctic zone above 60°N and the Antarctic zone below 60°S . Note, that

the months were selected depending on the availability of SCIAMACHY observations as explained in section 3.2.3.

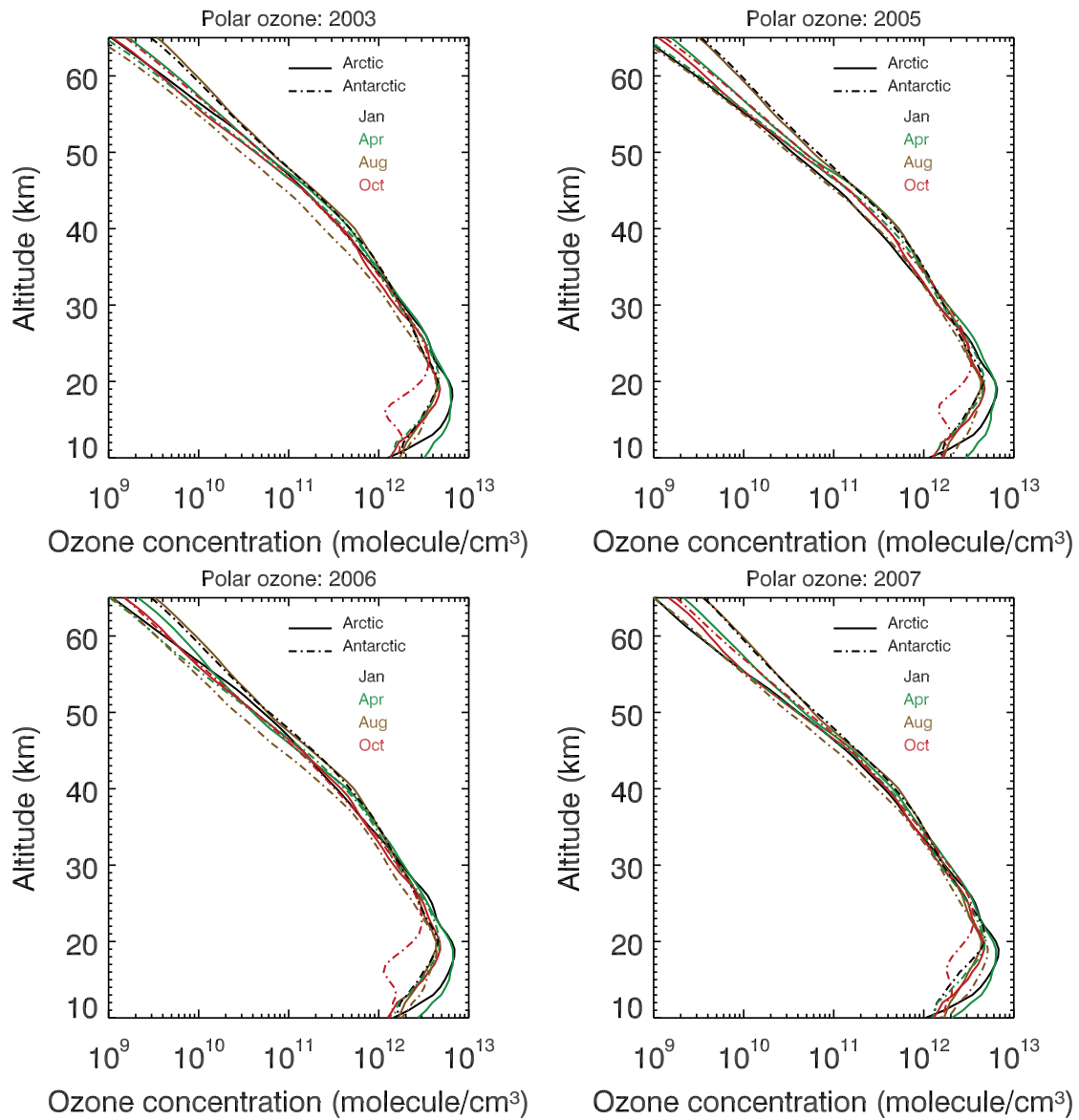


FIGURE 4.1: Samples of monthly averaged ozone profiles retrieved from SCIAMACHY limb-scatter observations for selected months and years in the Arctic (solid line) and Antarctic (dashed line) regions for latitudes poleward of 60° .

Considering Fig. 4.1 for the Antarctic region, the ozone concentrations dramatically decrease in spring time (October, the dashed-red line) of every year and return to normal levels in summer. For the Arctic region, the change in ozone concentrations is not as obvious as in the Antarctic region. Of course, from this figure one cannot tell whether the variation of polar ozone is due to dynamic influences or catalytic ozone destruction. We will concentrate on this topic again in Chapter 6.

This SCIAMACHY ozone data product has been validated and compared with other space-borne instruments, e.g., the Stratospheric Aerosol and Gas Experiment II (SAGE II) instrument on the Earth Radiation Budget Satellite (ERBS) and the Halogen Occultation Experiment (HALOE) instrument on the Upper Atmosphere Research Satellite (UARS).

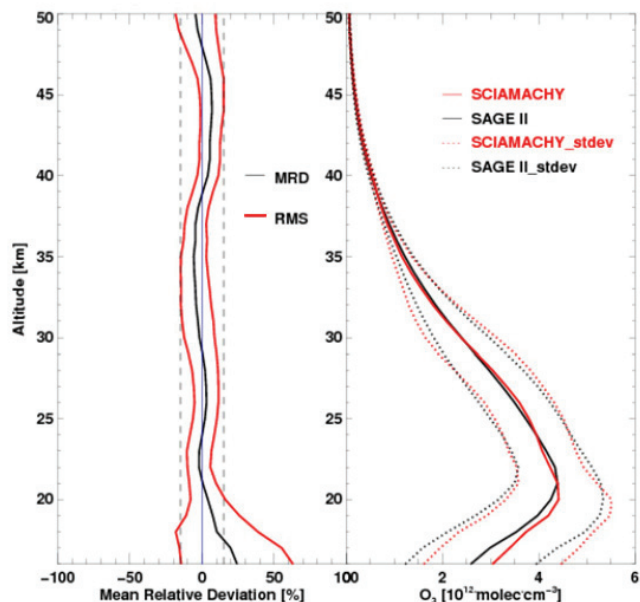


FIGURE 4.2: Sample validation result for the vertical ozone profiles retrieved from SCIAMACHY and SAGE II instruments at the co-located observations in 2005 (Amekudzi et al., 2008).

Amekudzi et al. (2008) have presented the validation of this ozone product (see Fig. 4.2 for an example). The solid red and black lines in the right panel Fig. 4.2 show the averaged vertical ozone profiles for all co-located SCIAMACHY and SAGE II observations, respectively, in 2005. The dotted lines of the same panel report the standard deviation of the vertical ozone profiles. The mean relative deviation (MRD) of the SCIAMACHY ozone product is shown in the left panel of Fig. 4.2 (black line). The MRD is within -6 % to +10 % between 20 and 50 km. The root mean square (RMS) values of the MRD are within 5-16 % in the same altitude range.

The ozone profiles from SCIAMACHY limb observations are also compared with HALOE observations. Figure 4.3 shows the measured ozone concentrations at latitudes between 40°N and 60°N measured with the HALOE instrument during 1992–2005 (blue) and from SCIAMACHY since 2002 (red) at 25 km (bottom) and 40 km (top) altitudes. This figure shows that the ozone observations from the two instruments are in good agreement as can be seen from the observation overlap during the period 2002–2005. The

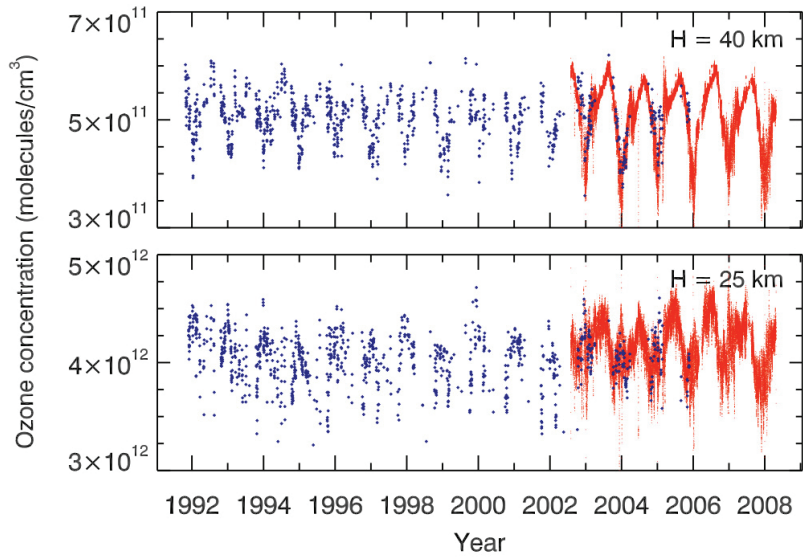


FIGURE 4.3: Time series of retrieved ozone concentrations from SCIAMACHY and HALOE instruments between $40^{\circ}\text{N} - 60^{\circ}\text{N}$ latitudes. The top panel shows the ozone concentration at an altitude of 40 km and the bottom panel for an altitude of 25 km.

comparison of limb ozone profiles from SCIAMACHY observations with the other instruments is also discussed in Ebojie (2009) showing good correspondence of ozone profiles from SCIAMACHY measurements and from HALOE and SAGE II observations. From the validation and comparison results, we conclude, that this novel SCIAMACHY ozone profile data product is of high quality and can be used for scientific analysis.

Chapter 5

Cloud sensitivity studies for the ozone profile retrievals from limb measurements

Clouds play an important role in the Earth's atmosphere. The tropospheric cloud coverage is about 50% at any given time and 7% of the total tropospheric volume is occupied by clouds (Lelieveld et al., 1989; Pruppacher and Jaenicke, 1995; Mace et al., 2007). Clouds interact with incoming solar radiation and long wavelength radiation emitted by the Earth, thus affecting the atmospheric energy budget and atmospheric photochemistry. Tropospheric clouds affect the scattering and penetration of solar photons in the atmosphere (e.g., Vanbauce et al., 2003; Rozanov and Kokhanovsky, 2004). The scattering process impacts trace gas retrievals from satellite instruments or ground-based measurements (e.g., Erle et al., 1995; Rozanov and Kokhanovsky, 2004; Rozanov and Kokhanovsky, 2008 and references therein).

Satellite observations of the scattered solar radiation in limb viewing geometry have become one of the standard techniques to measure stratospheric profiles of ozone and other minor constituents (e.g., McPeters et al., 2000; von Savigny et al., 2003; Haley et al., 2004; Rault, 2005). The limb-scatter observation geometry is characterized by a complex radiative transfer, because the multiple scattering or diffuse radiation contribution to the observed limb radiances can be significant (Oikarinen et al., 1999), and because the sphericity of the atmosphere cannot be neglected. Furthermore, the underlying surface, which may contribute significantly to the diffuse illumination of the sensed air volumes, is not observed directly. This geometry is strongly affected by surface albedo

and clouds, especially in the spectral ranges with small gaseous absorption. Although several recent studies presented detailed error analyses for stratospheric ozone profile retrievals from limb-scatter measurements (Haley et al., 2004; Loughman et al., 2005; von Savigny et al., 2005a), the effect of tropospheric clouds on the retrievals has not yet been comprehensively described or has been approximated by a high surface albedo in combination with an elevated Earth surface (e.g., Haley et al., 2004). In terms of stratospheric NO₂ profile retrievals from satellite limb-scatter observations, Sioris et al. (2003) performed some sensitivity studies on the effect of clouds on the retrievals.

The structure of this chapter is as follows. The methodology to investigate the cloud sensitivity of the ozone profile retrieval is summarized in section 5.1. Section 5.2 provides an introductory discussion of the ozone retrieval error caused by neglecting clouds in the retrieval process. An approximate approach to estimate the retrieval errors is introduced in section 5.3. The atmospheric, surface and cloud scenarios employed throughout the study are described in section 5.4. Section 5.5 discusses the reduction in cloud sensitivity of ozone profile retrievals if a wavelength triplet is used rather than single wavelengths. In section 5.6, the influence of tropospheric clouds on the ozone profiles retrieved from limb-scatter measurements in both the Hartley and Chappuis absorption bands is investigated. The sensitivity studies are shown in terms of relative percentage errors of ozone profiles retrieved assuming a cloud-free atmosphere, although the (synthetic) measurements are made in a cloudy atmosphere. Finally, all results are summarized in the last section.

5.1 Methodology

Due to a lack of detailed information on cloud properties in the observed part of the Earth's atmosphere only qualitative investigations of the impact of tropospheric clouds on the accuracy of the ozone vertical profile retrieval are possible when real measured data are used. In this study we employ an end-to-end numerical simulation technique allowing us to quantify the impact of tropospheric clouds of different kinds on the retrieval accuracy of ozone profiles in the stratosphere and lower mesosphere. The conceptual flow of our investigations is as follows:

1. We formulate the main scenario for the clear and cloudy atmosphere including typical vertical profiles of pressure, temperature, ozone number density, and surface albedo.

2. We formulate different cloud scenarios with various cloud parameters.
3. Using the radiative transfer code, we calculate the limb radiance spectra for these scenarios in the Hartley and Chappuis spectral absorption bands.
4. The simulated limb radiance spectra for cloudy conditions are considered as synthetic experimental data.
5. The vertical profile of ozone concentration is obtained ignoring cloudiness employing the retrieval algorithm as described in chapter 4.
6. The retrieval errors are obtained for each cloud scenario by taking the difference between the retrieved ozone profile and the ozone profile used for the forward simulations (the true profile).

The described end-to-end approach requires the usage of appropriate algorithms to simulate the limb radiance spectra and to retrieve the ozone vertical profile. For this purpose we have employed the software package SCIATRAN 2.2 (Rozanov et al., 2005b; Rozanov, 2008) to retrieve the vertical distributions of ozone in the stratosphere and the lower mesosphere from SCIAMACHY limb measurements.

Throughout this study, the forward modeling is performed in an approximative spherical mode employing the combined differential-integral (CDI) approach (Rozanov et al., 2001). With this approach the outgoing radiance is calculated integrating the contributions from both single and multiple scattering along the instrument line of sight intersecting a spherical shell atmosphere. The single scattered solar radiation is calculated fully spherically whereas the multiple scattering contribution is approximated for each point at the line of sight solving the pseudo-spherical radiative transfer equation for the proper atmospheric location and illumination. The pseudo-spherical solution is obtained employing the discrete-ordinate method similar to that described by Siewert (2000). The weighting functions are calculated employing the forward-adjoint technique as described by Rozanov (2006).

Employing the SCIATRAN radiative transfer model, limb radiance spectra are generated in a cloudy and cloud-free atmosphere for all considered wavelengths and tangent heights. The vectors containing the limb radiances (normalized limb radiance profiles for the UV wavelengths and the Chappuis triplet) will be denoted as y_c for cloudy, and y_f for cloud-free conditions.

5.2 Errors associated to clouds

Obviously, the limb radiance in the considered spectral range depends on the vertical distribution of ozone in the atmosphere. Thus, any variation of the ozone number density in the altitude range where the applied measurement technique is sensitive, leads to a variation of the limb radiance detected by the instrument. Let us assume that $y'_{c,f}(h_i)$ is obtained as a combination of measured limb radiances corresponding to the true ozone profile $n'(z)$. Then applying the Taylor series expansion, $y'_{c,f}(h_i)$ can be written as follows:

$$y'_{c,f}(h_i) = y_{c,f}(h_i) + \int_0^H \varpi_{c,f}(h_i, z) \delta n(z) dz + \varepsilon. \quad (5.1)$$

Here, $y_{c,f}(h_i)$ are the limb radiances calculated for a cloudy (subscript c) or for a cloud-free (subscript f) atmosphere using the a priori ozone vertical profile $n(z)$, H is the top of atmosphere altitude, $\delta n(z) = n'(z) - n(z)$ is the variation of the ozone number density profile, $\varpi_{c,f}(h_i, z)$ is the variational derivative of the appropriate limb radiance combination, as given by Eq. (4.23) or (4.24), with respect to the ozone number density, which is commonly referred to as the weighting function (see [Rozanov \(2006\)](#) for further details):

$$\varpi_{c,f}(h_i, z) = \frac{\delta y_{c,f}(h_i)}{\delta n(z)}, \quad (5.2)$$

and ε is the linearization error containing the contributions of higher-order terms of the Taylor series. We note that the weighting function for the gaseous absorber concentration as given by Eq. (5.2) is always negative because increasing the absorber concentration leads to an increase in light absorption and, hence, to an decrease in the limb radiance.

If the cloudiness in the Earth's atmosphere is treated properly, the true vertical profile of ozone can formally be obtained from the corresponding radiances as follows:

$$\hat{n}'_c(z) = n(z) + \mathcal{R}_c[y'_c(h_i) - y_c(h_i)], \quad (5.3)$$

where $\hat{n}'_c(z)$ is the estimation of the true ozone vertical profile and \mathcal{R}_c is the inverse operator whose explicit form depends on the applied retrieval algorithm. In particular, a nonlinear Newtonian iterative retrieval approach of the optimal estimation ([Rodgers, 1976](#)) type is employed throughout this study. The diagonal elements of the a priori covariance matrix were set to standard deviations of 1000 % to ensure that the retrieval

is completely independent to the a priori information. The off-diagonal elements were determined assuming a correlation length of 1.5 km.

In a common retrieval process, $y'_c(h_i)$ in Eq. (5.3) is obtained as a combination of the measured limb radiances whereas $y_c(h_i)$ is simulated with the forward model using the a priori profile $n(z)$. However, due to a lack of information about the cloud parameters in the observed scene it is usually impossible to simulate $y_c(h_i)$ and \mathcal{R}_c properly. The easiest way to avoid this problem is to neglect the clouds in the retrieval process assuming a cloud-free atmosphere when simulating the limb radiances and obtaining the inverse operator. This results, however, in a different estimation (compared to Eq. 5.3) for the true vertical distribution of ozone:

$$\hat{n}'_f(z) = n(z) + \mathcal{R}_f[y'_c(h_i) - y_f(h_i)] , \quad (5.4)$$

where, in contrast to \mathcal{R}_c , the inverse operator \mathcal{R}_f is employed assuming a cloud-free atmosphere. Obviously, the absolute error in the retrieved vertical distributions of ozone occurring due to this approximation can be estimated as follows:

$$\Delta n(z) = \hat{n}'_f(z) - n'(z) , \quad (5.5)$$

where $n'(z)$ is the true vertical profile of ozone which is known since the numerical simulation technique is used. For simplicity reasons, the numerical experiments are performed throughout this study assuming that the true ozone number density profile is the same as the a priori one, i.e., $n'(z) = n(z)$ and $\delta n(z) = 0$. Hence, as follows from Eq. (5.1), $y'_c(h_i) = y_c(h_i)$, and Eq. (5.4) results in

$$\hat{n}'_f(z) = n(z) + \mathcal{R}_f[y_c(h_i) - y_f(h_i)] . \quad (5.6)$$

Substituting $\hat{n}'_f(z)$ as given by Eq. (5.6) into Eq. (5.5) and taking into account that $n'(z) = n(z)$, we obtain

$$\Delta n(z) = \mathcal{R}_f[y_c(h_i) - y_f(h_i)] . \quad (5.7)$$

Here, $\Delta n(z)$ characterizes the absolute retrieval error (retrieved minus true ozone number density) caused by neglecting the cloudiness in the retrieval process. In the following sections, we consider the relative error of the ozone vertical profile retrieval as given

by

$$r(z) = \frac{\Delta n(z)}{n(z)} = \frac{1}{n(z)} \mathcal{R}_f \left[y_c(h_i) - y_f(h_i) \right]. \quad (5.8)$$

5.3 Approximate approach to estimate the retrieval errors

In the previous section, we have described an approach allowing us to calculate the error in the retrieved ozone profiles associated with neglecting clouds in the retrieval process. Unfortunately, the final expression for this error, Eq. (5.7), contains the inverse operator, \mathcal{R}_f , which, for the problem under consideration, does not have an analytical representation. Thus, for each considered atmospheric scenario the inverse problem needs to be solved numerically. Furthermore, the complicated relationship between the observed limb radiance and the retrieved concentrations does not allow the obtained results to be easily explained. In this section, we derive an approximate expression which establishes a simple relationship between the observed quantities and the retrieval error of the ozone profiles allowing the latter to be estimated without solving the inverse problem.

One of the objectives of our discussion below is to illustrate how the normalization and combination of the limb radiances into the Chappuis triplet affects the sensitivity of the retrieval error to the tropospheric clouds. For this reason, in addition to the Chappuis triplet, we consider also the absolute limb radiance (i.e., not normalized) when discussing the approximate approach to estimate the retrieval error. On the other hand, it is clear that, because of the stronger extinction of the atmosphere, much less light penetrates down to the troposphere in the UV spectral region as compared to the visible range. Thus, the expected sensitivity of limb observations to tropospheric clouds is much weaker in the UV spectral range. For this reason, we do not consider the UV wavelengths when discussing the approximate retrieval error. Please note that the UV wavelengths are considered when calculating the error employing the end-to-end numerical approach according to Eq. (5.7) or (5.8). For further considerations, let us introduce a new notation, $S_{c,f}(h_i)$, which will denote the Chappuis triplet, absolute limb radiance or normalized limb radiance for a cloudy and a cloud-free atmosphere, respectively. Further in the scope of this work, $S_{c,f}(h_i)$ will be referred to as the limb signal.

Generally, retrieval errors due to neglect of clouds occur because the presence of clouds in the atmosphere causes changes in the limb signal similar to perturbations in the ozone vertical distribution. These retrieval errors can be estimated employing Eq. (5.1). To this end let us rewrite this equation with the limb signals $S_c(h_i)$ and $S_f(h_i)$ corresponding to the cloudy and the cloud-free atmosphere on the left-hand and right-hand sides of Eq. (5.1), respectively. Eq. (5.1) results in

$$S_c(h_i) = S_f(h_i) + \int_0^H \varpi_f(h_i, z) \delta n(z) dz \quad (5.9)$$

or

$$\Delta S(h_i) = \int_0^H w_f(h_i, z) r_\delta(z) dz . \quad (5.10)$$

Here, $\Delta S(h_i) \equiv S_c(h_i) - S_f(h_i)$ is the variation of the limb signal caused by the cloud only because $S_c(h_i)$ and $S_f(h_i)$ were calculated using the same the a priori ozone vertical density $n(z)$, $r_\delta(z) = \delta n(z)/n(z)$ is the relative variation of the ozone number density caused by neglect of the cloud and $w_f(h_i, z)$ is the corresponding weighting function that is usually referred to as the relative weighting function. Clearly, the relationship between the relative and absolute weighting functions is given by

$$w_{c,f}(h_i, z) = \varpi_{c,f}(h_i, z) n(z) . \quad (5.11)$$

Please note that, though the same notation is used, the weighting functions for the absolute limb radiance and for the Chappuis triplet are different.

It is worth noting that Eq. (5.9) states that the limb signal for a cloudy atmosphere and the a priori ozone profile $n(z)$ is related to the limb signal for a perturbed ozone profile, i.e., $n(z) + \delta n(z)$, and a cloud-free atmosphere. We emphasize that the perturbation of ozone vertical profile $\delta n(z)$ or $r_\delta(z)$ is a parameter to be found solving Eq. (5.9) or (5.10), respectively. Approximating the relative variation of the ozone number density $r_\delta(z)$ in Eq. (5.10) by an altitude independent value $\bar{r}_\delta(h_i)$ as follows:

$$\bar{r}_\delta(h_i) = \frac{\int_0^H w_f(h_i, z) r_\delta(z) dz}{\int_0^H w_f(h_i, z) dz} , \quad (5.12)$$

it can be seen that Eq. (5.10) results in:

$$\bar{r}_\delta(h_i) = \frac{\Delta S(h_i)}{W_f(h_i)}, \quad (5.13)$$

where $W_f(h_i)$ is the vertically integrated weighting function defined by

$$W_f(h_i) = \int_0^H w_f(h_i, z) dz. \quad (5.14)$$

Thus, as follows from Eq. (5.13), the approximate relative error in the ozone vertical distributions retrieved neglecting clouds in both forward model and the retrieval approach is proportional to the difference between the limb signals in a cloudy and a cloud-free atmosphere. This conclusion is in line with the results of the end-to-end numerical treatment given by Eq. (5.8).

A further simplification can be obtained using an approximate representation for $\Delta S(h_i)$ in Eq. (5.13). To obtain this approximation let us first expand the limb signal in a Taylor series similar to Eq. (5.1) restricting our consideration to linear terms:

$$S_{c,f}(n') = S_{c,f}(n) + \int_0^H w_{c,f}(z) \frac{\delta n(z)}{n(z)} dz. \quad (5.15)$$

Assuming that in the perturbed state no ozone is present in the atmosphere, i.e., the perturbed vertical profile, $n'(z)$, is equal to zero, the relative variation of the ozone concentration is written as

$$\frac{\delta n(z)}{n(z)} = \frac{0 - n(z)}{n(z)} = -1 \quad (5.16)$$

and Eq. (5.15) results in

$$S_{c,f}(0) = S_{c,f}(n) - \int_0^H w_{c,f}(z) dz, \quad (5.17)$$

where $S_{c,f}(n)$ and $S_{c,f}(0)$ are the limb signals with and without ozone absorption, respectively. Employing Eq. (5.17), the difference between the limb signals in a cloudy and a cloud-free atmosphere can be expressed as follows:

$$S_c(n) - S_f(n) = [S_c(0) - S_f(0)] + [W_c - W_f]. \quad (5.18)$$

or

$$\Delta S(n) = \Delta S(0) + \Delta W . \quad (5.19)$$

The first term on the right-hand side of Eq. (5.19) describes the variation of the limb signal due to the enhanced reflection of solar radiation by clouds in a non-absorbing atmosphere. The second term represents the variation of the gaseous absorption caused by changes in photon path lengths in a cloudy atmosphere. We will refer to these terms hereafter as the scattering and absorption terms, respectively. Substituting $\Delta S(n)$ as given by Eq. (5.19) into Eq. (5.13), the following expression for the approximate retrieval error is obtained:

$$\hat{r}_\delta(h_i) = \frac{\Delta S(h_i; 0) + \Delta W(h_i)}{W_f(h_i)} . \quad (5.20)$$

Although this equation provides a very convenient tool to analyze the retrieval error and allows the absorption by atmospheric trace gases and the reflection of light by clouds to be considered independently, it is affected by the quite strong limitation of the assumed linearity. In Section 5.5, we will consider a few examples showing that under certain conditions this limitation can lead to completely wrong results when estimating the retrieval error using Eq. (5.20).

5.4 Atmospheric and cloud scenarios

Throughout this study, the limb radiance is simulated in selected spectral intervals considering Rayleigh scattering, ozone absorption, and scattering of light by clouds. The surface reflection is assumed to be Lambertian and the ground albedo is set to 0.1, 0.3, 0.5, and 0.9. As only the cloud effect on the ozone profile retrieval will be focused on here, no aerosols are taken into account. The vertical profiles of pressure, temperature and ozone number density were taken from [Prather and Remsberg \(1993\)](#).

In the Earth's atmosphere clouds occur in three different thermodynamic states: water, ice, and mixed states. Unlike the water clouds, the microphysical properties of the ice clouds cannot be characterized by a single shape and particle-size distribution, because the size, shape, orientation and internal structure of the ice particles in crystalline clouds can be very different (e.g., [Kokhanovsky, 2004](#)). Fortunately our preliminary investigations have shown that the ozone profile retrieval is mainly affected by the cloud optical

thickness rather than by the thermodynamic state of the cloud. Therefore, only water clouds are considered here. Furthermore, the cloud droplets are assumed to be spherical and Mie calculations are used to establish the scattering phase functions and scattering coefficients. The clouds are considered to be homogeneous.

The classification of water clouds in this study is based on the definitions of the International Satellite Cloud Climatology Project (ISCCP) and depends on the cloud optical thickness and cloud top pressure (Rossow and Schiffer, 1999). In this work, the cloud top pressure is converted to the cloud top height using the pressure profiles mentioned above. For simplicity reasons, the top and bottom heights resulting from this transformation for each cloud type were shifted up- and downwards, respectively, to match the internal altitude grid levels of the forward model. As a result, in the cloud classification used throughout this study, shown in Table 5.2, the clouds of different types overlap in altitude, which is not the case in the original ISCCP classification. However, for our study there are no disadvantages associated with this overlap.

TABLE 5.1: Cloud classification by top and bottom heights and optical thickness, τ . The τ values are the same as in the ISCCP classification.

τ	Low clouds 1-3 km	Middle clouds 2-7 km	High clouds 6-15 km
0-3.6	cumulus	altocumulus	cirrus
3.6-23	stratocumulus	altostratus	cirrostratus
23-379	stratus	nimbostratus	deep convection

Table 5.2 provides an overview of the sets of cloud parameters used for each considered cloud scenario. The following abbreviations are used in the table and in the text below: τ is the cloud optical thickness, r_e denotes the effective radius of water droplets, A is used for the Lambertian surface albedo, and the viewing geometry is defined by the solar zenith angle (SZA) and the solar azimuth angle (SAA). The angles are defined at the tangent point.

5.5 Absolute radiance vs. Chappuis triplet

In this section, we employ the approximate relationships for the retrieval error obtained in Section 5.3 to analyze how the combination of the limb radiances in the Chappuis

TABLE 5.2: Cloud parameter sets used in this study. The varied parameters are marked with (\checkmark).

Sections/Studied tests	Cloud parameter						Figs.
	Cloud extension (km)	τ	r_e (μm)	SZA	SAA	A	
Absolute radiance vs. Chappuis triplet	4-7	10	8	30	90	0.3	Fig. 5.1, Fig. 5.2
	4-7	10	8	30	90	0.9	Fig. 5.3
Investigation of the retrieval errors	4-7	10	8	30	90	0.3	Fig. 5.4
Cloud types							
• Low cloud	1-3	\checkmark	8	30	90	0.3	Fig. 5.5a
• Middle cloud	2-7	\checkmark	8	30	90	0.3	Fig. 5.5b
• High cloud	6-15	\checkmark	8	30	90	0.3	Fig. 5.5c, Fig. 5.5d
Effective radius of water droplets	2-7	10	\checkmark	30	90	0.3	Fig. 5.7a
Cloud geometries							
• Clouds top height	\checkmark	10	8	30	90	0.3	Fig. 5.8a
• Cloud geometrical thickness	\checkmark	10	8	30	90	0.3	Fig. 5.8b
Ground albedo	2-7	10	8	30	90	\checkmark	Fig. 5.9a, Fig. 5.10
	2-7	2	8	30	90	\checkmark	Fig. 5.9e
Viewing angles							
• SZA	2-7	10	8	\checkmark	90	0.3	Fig. 5.11a
• SAA	2-7	10	8	30	\checkmark	0.3	Fig. 5.11b
• SCIAMACHY limb-scan	2-7	10	8	\checkmark	\checkmark	0.3	Fig. 5.13a
• OSIRIS limb-scan	2-7	10	8	\checkmark	\checkmark	0.3	Fig. 5.13b
Frequent cloud	4-7	10	8	\checkmark	\checkmark	0.3	Fig. 5.14

triplet affects the sensitivity of the ozone profile retrievals to tropospheric clouds. Furthermore, the validity of the linearity assumption employed to separate the contributions of the atmospheric absorbers and the reflection of solar light by clouds, see Eq. (5.20), is investigated.

As seen from Eq. (5.20), the magnitude and sign of the retrieval error depends on the relationship between the terms $\Delta S(h_i; 0)$ and $\Delta W(h_i)$ which can be significantly different for the absolute limb radiance and for the Chappuis triplet. This is illustrated in Fig. 5.1. The upper left and right panels of the figure show the contributions of the scattering term $\Delta S(h_i; 0)/W_f(h_i)$ and absorption term $\Delta W(h_i)/W_f(h_i)$ to the total retrieval error for the absolute and normalized limb radiance at 602 nm, respectively, whereas the lower panel shows the same for the Chappuis triplet. The calculations were performed for the parameter set given in Table 5.2. It follows that for the absolute limb radiance, as shown in the upper left panel of Fig. 5.1, the contribution of the absorption term is positive whereas the contribution of scattering term is negative and it dominates.

The obtained results can be easily explained. Indeed, on the one hand the appearance of a cloud in the atmosphere leads usually to an increase in the reflected limb radiance as compared to the cloud-free case and, hence, to the positive value of $\Delta S(h_i; 0)$. The only way for the cloud-free model to match the enhanced limb radiance is to decrease the ozone concentration. This results in the negative ozone retrieval error for the scattering term. On the other hand, the presence of a cloud leads to increased absorption and,

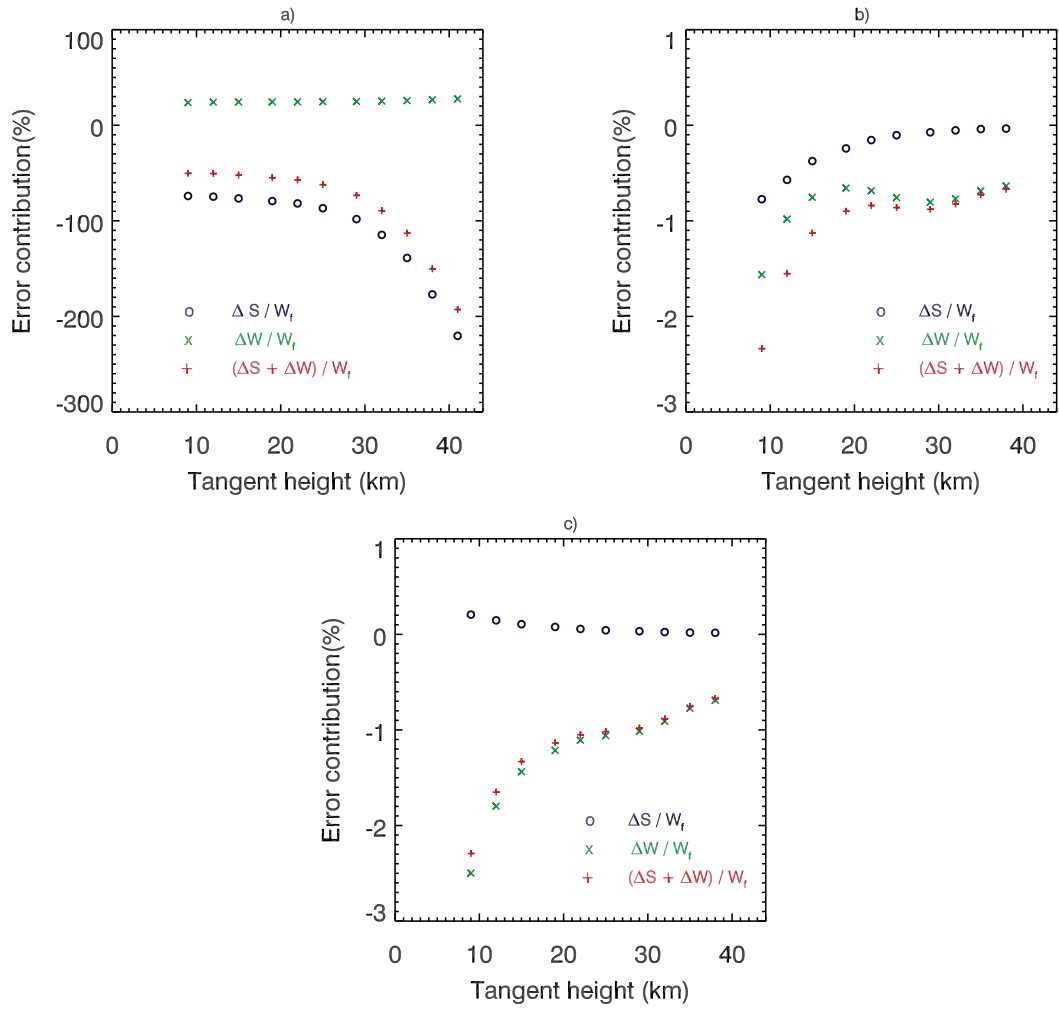


FIGURE 5.1: Contribution of the terms $\Delta S(h_i; 0)/W_f(h_i)$ and $\Delta W(h_i)/W_f(h_i)$ to the linearized approximate retrieval error obtained according to Eq. (5.20). Panel a shows the results for the absolute limb radiance at 602 nm, panel b for the normalized limb radiance at 602 nm and panel c for the Chappuis triplet. The calculations were performed using the parameters given in Table 5.2.

therefore, to a decreased limb radiance. In this case, the absorption error term is positive because the cloud-free model needs larger ozone concentrations to match the increased path-absorption. Thus, in the case of the absolute limb radiance the enhanced reflection of the solar light in a cloudy atmosphere is the main source of error in the retrieved ozone profile occurring due to neglecting tropospheric clouds in the retrieval process.

On the contrary, the contribution of the scattering term is significantly smaller for the normalized limb radiance and for the Chappuis triplet, as shown in the upper right and in the lower panel of Fig. 5.1. In these cases, the error in the retrieved ozone profiles is mainly due to the differences in the gaseous absorption associated with changes in

photon path lengths in a cloudy atmosphere. Comparing the contribution of the absorption term to the ozone retrieval error in the case of the absolute and normalized limb radiances shown in the upper left and upper right panels of Fig. 5.1, respectively, one can see that this term changes its sign. This can be explained by the fact that, although in the presence of a cloud the limb radiance decreases due to an enhancement of path-absorption at all relevant tangent heights, the relative decrease at the reference tangent height is stronger. Therefore, in the presence of a cloud, the normalised limb radiance increases due to additional path-absorption as compared to a cloud-free atmosphere. Thus, the cloud-free model needs lower ozone concentrations to match the increased normalised limb radiance and the corresponding ozone retrieval error becomes negative.

As can be clearly seen, the impact of clouds is much larger for the absolute limb radiance as compared to the normalized one, and compared to the Chappuis triplet. Moreover, employing the normalized limb radiance or the Chappuis triplet in the framework of cloud-free model, one can expect a systematic underestimation of the retrieved ozone profile.

Figures 5.2 and 5.3 illustrate the impact of the linearity assumption used to derive the linearized representation for the approximate retrieval error as given by Eq. (5.20). The results are shown for the absolute limb radiance at 602 nm (panel a), the normalized limb radiance at 602 nm (panel b), and for the Chappuis triplet (panel c) for different values of surface albedo. Figure 5.2 shows the approximate error of the ozone profile retrieval calculated with and without linearity assumption according to Eqns. (5.20) and (5.13), respectively, for a surface albedo of 0.3 and the same cloud parameters and viewing geometry as described above. Figure 5.3 shows the same errors but for a surface albedo of 0.9. As seen from the plots, under certain conditions (e.g., high surface albedo) the linearization error for the Chappuis triplet is so high that not even the correct sign of the approximate error is reproduced.

The obtained results demonstrate that using the combination of the limb radiances in the Chappuis triplet leads to a significant decrease of the cloud impact on the retrieval process. On the other hand, this combination can increase the non-linearity of the problem making the linear representation for the approximate error as given by Eq. (5.20) unusable. Therefore, this representation is not used in the discussion below. Instead, the dependence of the retrieval error on the cloud parameters is discussed in the next section employing the much more robust expression for the approximate error as given by Eq. (5.13).

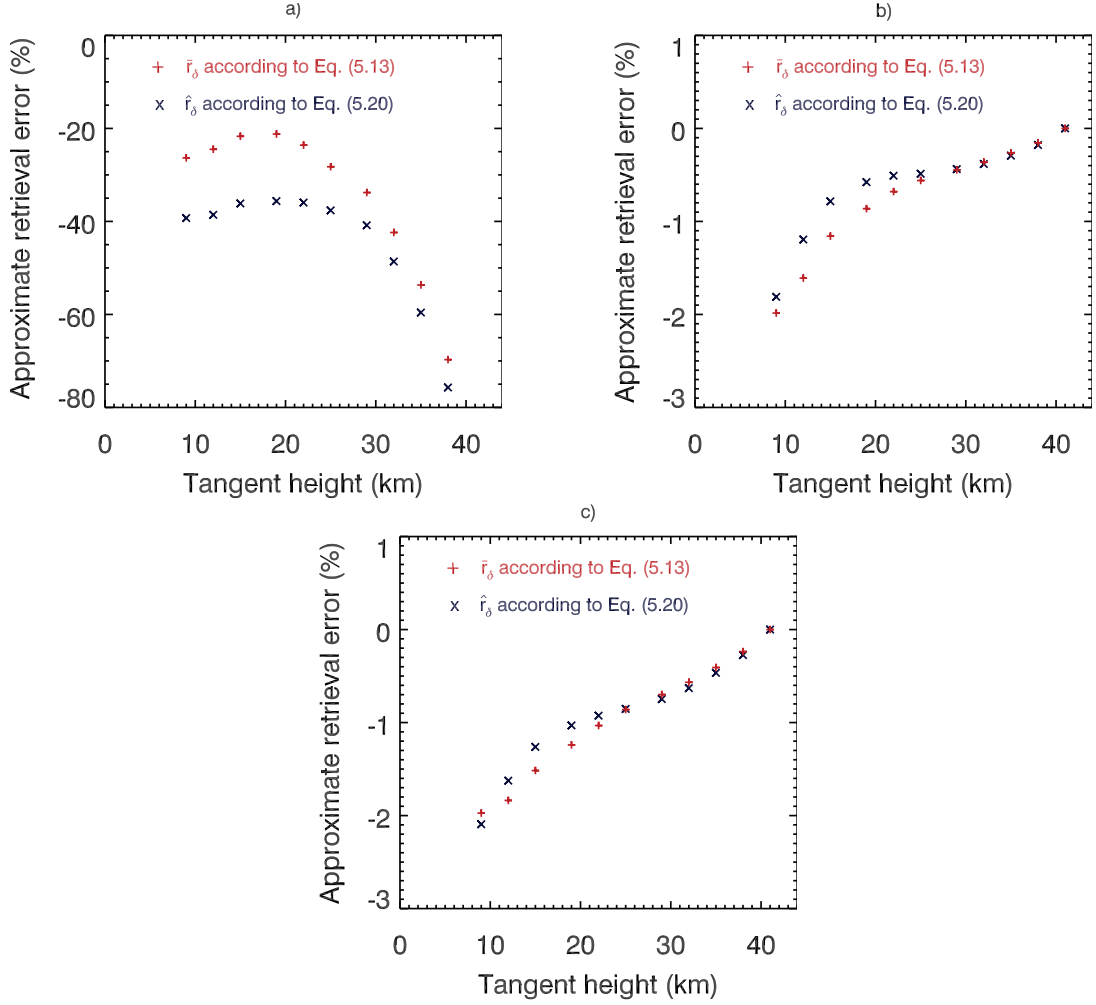


FIGURE 5.2: Comparison of the approximate errors of the ozone profile retrieval calculated with and without linearity assumption according to Eqns. (5.20) and (5.13), respectively. Panel (a) shows the results for the absolute limb radiance at 602 nm, panel (b) for the absolute normalized limb radiance at 602 nm, and panel (c) for the Chappuis triplet. The calculations were performed for the same set of parameters as in Fig. 5.1.

5.6 Investigation of the retrieval errors

In this section, the errors in the retrieved vertical distributions of ozone occurring due to neglecting tropospheric clouds in the retrieval process are analyzed employing the full end-to-end numerical approach for different cloud scenarios and viewing geometries. The obtained results are explained using the approximate representation of the retrieval error obtained above (see Eq. (5.13)).

An example of the ozone vertical profile obtained neglecting tropospheric clouds in the retrieval process, as described by Eq. (5.6), is shown in Fig. 5.4 in comparison with the

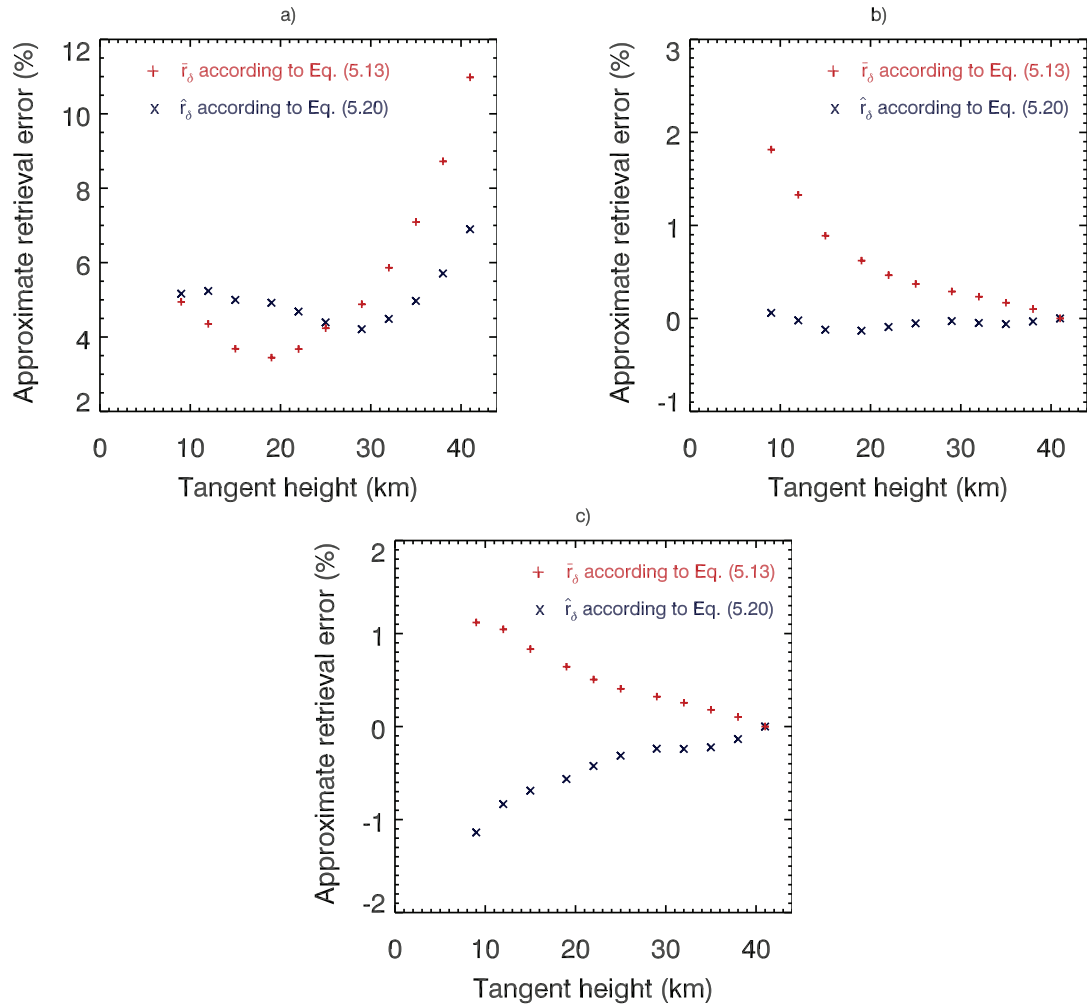


FIGURE 5.3: Same as Fig. 5.2 but for a surface albedo of 0.9.

true vertical distribution of ozone. The cloud parameters and the observation geometry are the same as in Fig. 5.1. As the plot shows, the effect of the tropospheric clouds appears as a small underestimation of the ozone number density in the altitude region below 30 km whereas in the upper layers, where most of the information originates from the UV wavelengths, the ozone retrieval is relatively insensitive to clouds. As shown below, this low bias in the retrieved ozone concentrations at lower altitudes is typical for neglecting tropospheric clouds in the retrieval process for most cloud scenarios.

5.6.1 Cloud optical thickness

Figure 5.5 shows the sensitivity of ozone profile retrievals to tropospheric clouds for different τ and different altitudes of the cloud layer. The SZA and SAA are set to 30°

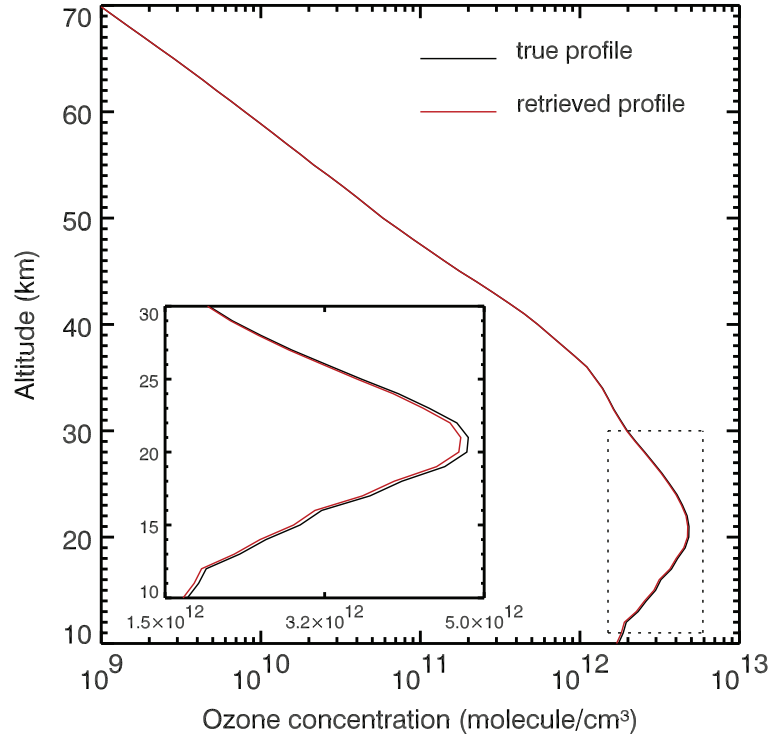


FIGURE 5.4: An example of the ozone vertical profile obtained neglecting the tropospheric clouds in the retrieval process, as described by Eq. (5.6), in comparison with the true vertical distribution of ozone. The calculations were performed for the same set of parameters as in Fig. 5.1.

and 90° , respectively. The sensitivity is expressed in terms of the relative percentage error according to Eq. (5.8). Panels a and b of Fig. 5.5 show the retrieval errors for the low and middle clouds, respectively, according to the classification given in Table 5.2. As seen from the plot, when being neglected in the retrieval process, low and middle clouds with the same τ cause similar errors in the retrieved ozone profiles. Generally, the retrieval error caused by this type of clouds is up to about 5% at 10 km altitude decreasing with increasing altitude and with decreasing τ . The results for the high clouds are shown in panel c and d of Fig. 5.5. Panel c shows the results for the standard tangent height range, as given in Table 4.1, where the cloud is in the instrument field of view. Panel d shows the results for the lowest tangent height set to 19 km. As an investigation of the retrieval error within the cloud is outside the scope of this study, the results for high clouds are shown only for the altitudes above the cloud layer, i.e., above 18 km. As clearly seen from the plots, the retrieval error reaching 17% at 18 km for the standard tangent height range ($h_{low} = 9$ km) decreases to less than 3.5% if the lines of sight are rejected, for which the cloud is in the field of view of the instrument ($h_{low} = 19$ km). In future versions of the ozone profile retrieval from SCIAMACHY

limb measurements cloud top height information – also retrieved from SCIAMACHY limb observations with a colour-index approach similar to the PSC detection described in von Savigny et al. (2005b) – will be employed to limit the range of tangent heights used.

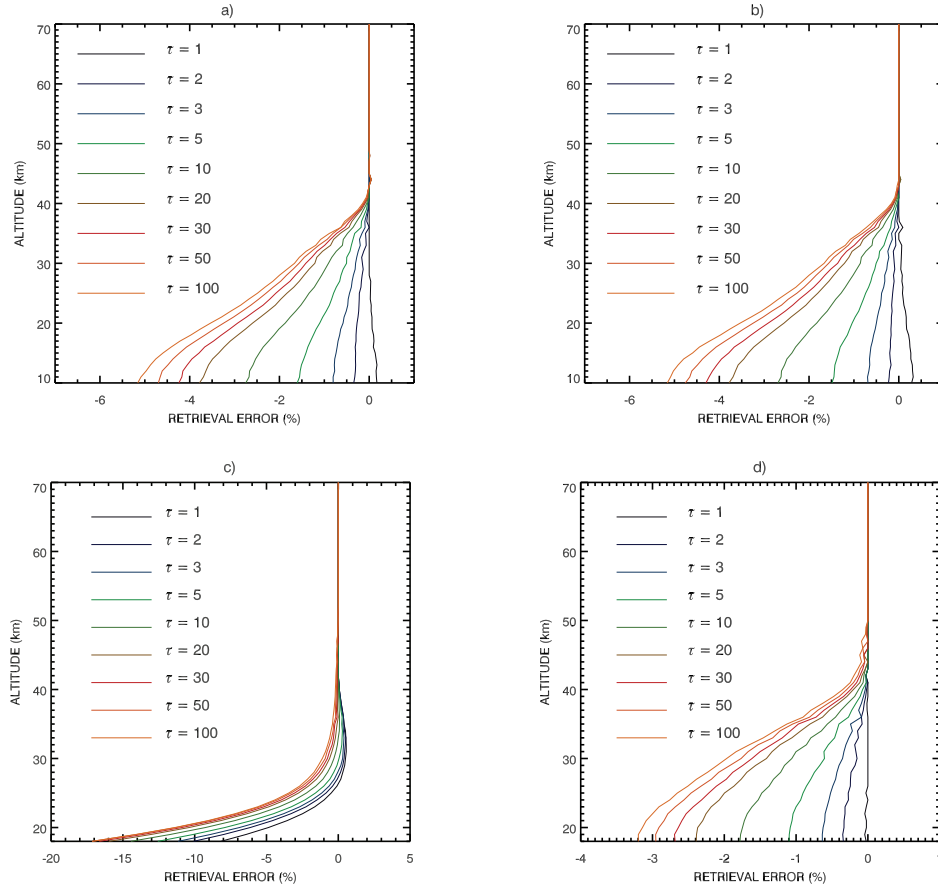


FIGURE 5.5: Relative errors in the retrieved ozone profiles due to neglect of clouds in the retrieval process. Results are shown for different altitudes of the cloud layer and for different cloud optical thicknesses τ : (a) low clouds (1 – 3 km), (b) middle clouds (2 – 7 km), (c) high clouds (6 – 15 km) for the standard tangent height range, i.e., $h_{low} = 9$ km is the lowest tangent height included in the retrieval, (d) high clouds for the reduced tangent height range, $h_{low} = 19$ km.

For all cloud layer altitudes, the retrieval errors shown in Fig. 5.5 are mostly negative and decrease with increasing altitude as well as with decreasing τ . Thus, most typically, the ozone concentrations are underestimated if the tropospheric clouds are neglected in the retrieval process. However, for a small τ , the retrieval error can change its sign and become positive, as for example for low and middle clouds at $\tau = 1$. These general dependencies can be explained considering the approximate retrieval error as given by Eq. (5.13).

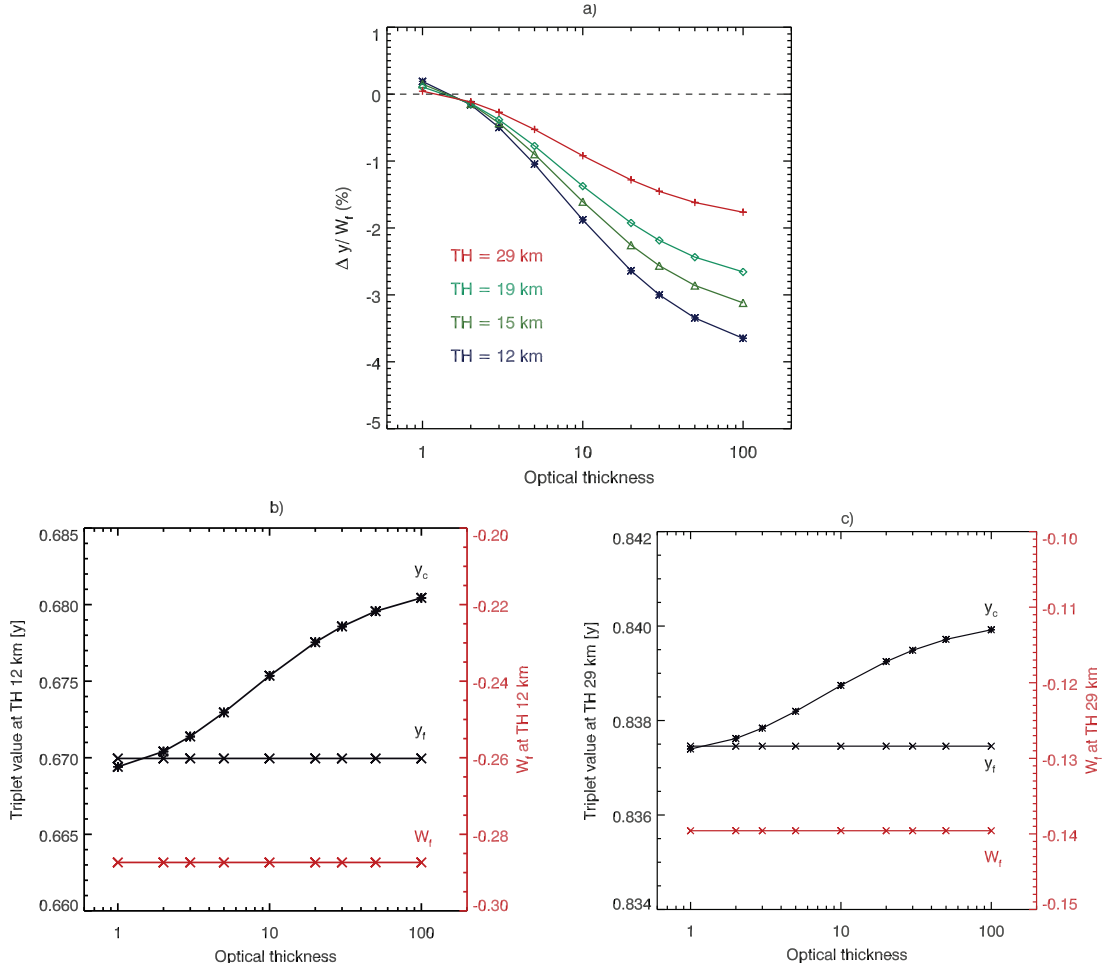


FIGURE 5.6: Panel a: approximate retrieval error according to Eq. (5.13) at tangent heights of 12 km, 15 km, 19 km and 29 km as a function of the cloud optical thickness. Panel b and panel c: Chappuis triplet for a cloudy and a cloud-free atmosphere as well as integrated weighting function at a tangent height of 12 km and 29 km respectively. The calculations were performed for a middle cloud (the same scenario as in Fig. 5.5b). Please note that the subscripts “c” and “f” refer to a cloudy and a cloud-free atmosphere, respectively.

Panel a of Fig. 5.6 shows the approximate retrieval error at different tangent heights calculated for a middle cloud (as in Fig. 5.5b). As can be seen from the plots, the approximate retrieval errors shown in Fig. 5.6a are in good qualitative agreement with the errors obtained using the full end-to-end numerical approach presented in Fig. 5.5b. In particular, the retrieval errors in both Figs. 5.5b and 5.6a change the sign between $\tau = 1$ and $\tau = 2$ and increase with increasing optical thickness of the cloud for $\tau \geq 2$. As, according to Eq. (5.13), the approximate retrieval error is proportional to the difference in the limb signals for a cloudy and a cloud-free atmosphere, the dependence of the retrieval error on the cloud optical thickness can be analyzed considering the corresponding values of the Chappuis triplet. Panels b and c of Fig. 5.6 show the Chappuis triplet

for a cloudy atmosphere (for the same scenario as in Fig. 5.5b) as a function of the τ as well as the Chappuis triplet and the integrated weighting function for a cloud-free atmosphere at 12 km and 29 km tangent height, respectively. Obviously, the Chappuis triplet in a cloudy atmosphere, y_c , increases with increasing τ . Consistently with Fig. 5.6a, the Chappuis triplet value for a cloudy atmosphere at $\tau = 1$ is smaller than the cloud-free value leading to a positive retrieval error (note that the integrated weighting function is negative) whereas the opposite behavior is observed for $\tau \geq 2$.

The dependence of the ozone retrieval errors on the optical depth of tropospheric clouds discussed above can be explained using the findings of Roebeling et al. (2005) and Liou (1973) who have discovered that the reflected solar radiation at visible wavelengths (630 nm and 700 nm, respectively) increases with increasing τ , i.e., optically thicker clouds reflect more solar light. As demonstrated in Appendix A, a variation of cloud parameters causing an increase in the reflected solar radiation also leads to an increase in the Chappuis triplet values. Thus, the enhanced reflection due to optically thick clouds causes an increase in limb radiance leading, in turn, to larger values of the Chappuis triplet which results then in smaller ozone concentrations when retrieving the profiles neglecting the clouds. Clearly, optically thicker clouds reflecting more solar light affect the retrievals more strongly. This provides an explanation for the typical dependence of ozone profile retrieval errors on τ and the general underestimation of ozone concentrations retrieved from limb-scatter observations neglecting tropospheric clouds in the retrieval process.

5.6.2 Effective radius of water droplets

In this section, the dependence of the ozone profile retrieval error on the effective radius of water droplets within the cloud is investigated. The effective radius of water droplets, r_e , is defined as the ratio of the third moment to the second moment of the droplet size distribution (Hansen and Travis, 1974). The comparison is performed for a middle cloud and the parameter set given in Table 5.2. Since the τ is fixed, the water droplet scattering phase function is the only parameter changing when the r_e is varied.

The sensitivity of the ozone vertical profile retrievals, performed neglecting tropospheric clouds, to the r_e within the cloud is illustrated in panel a of Fig. 5.7. This figure demonstrates that the impact of clouds with small water droplets is slightly higher than for larger droplets. However, as the difference in the relative errors between the large (20 μm) and small (4 μm) water droplets is less than 0.5%, one can conclude that the

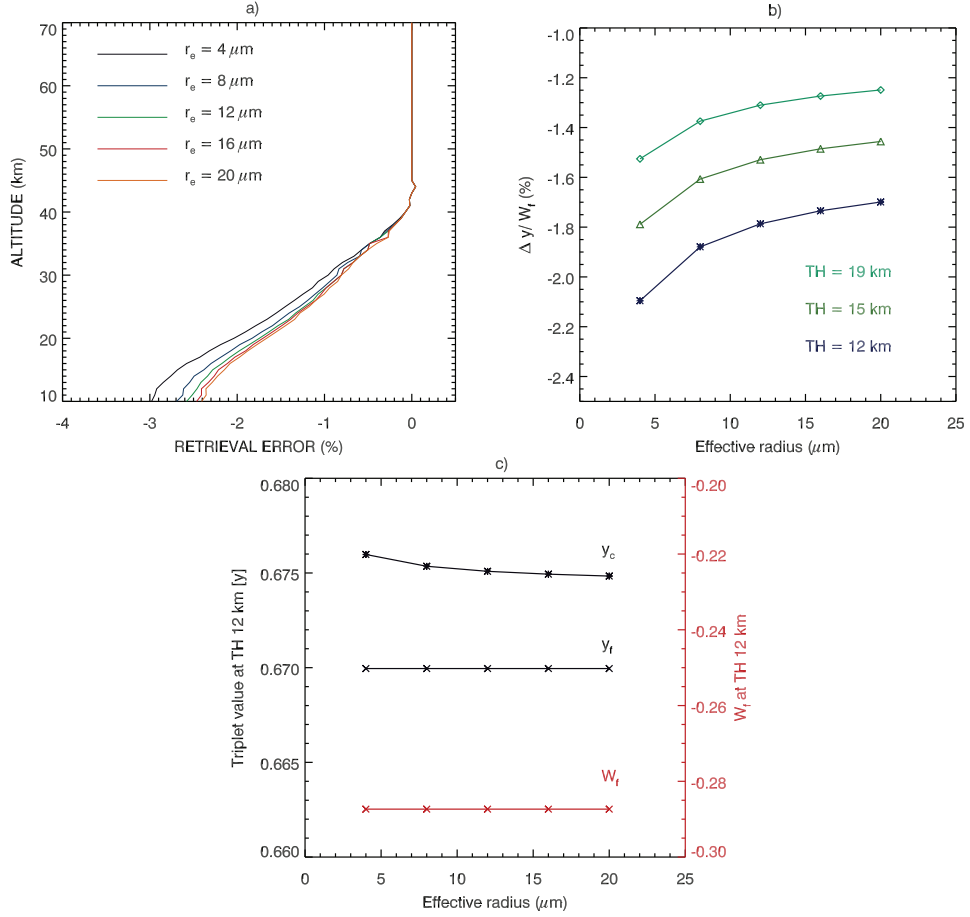


FIGURE 5.7: Panel a: relative errors in the retrieved ozone profiles due to neglect of clouds in the retrieval process for different r_e . Panel b: approximate retrieval error according to Eq. (5.13) at tangent heights of 12 km, 15 km, and 19 km as a function of the r_e . Panel c: Chappuis triplet for a cloudy and a cloud-free atmosphere as well as integrated weighting function at a tangent height of 12 km. The calculations were performed for a middle cloud and the parameter set given in Table 5.2.

overall influence of the r_e on the ozone profile retrieval is rather small. Similar to the previous section, this dependence can be qualitatively explained considering the approximate retrieval error as given by Eq. (5.13). Panel b of Fig. 5.7 shows the approximate retrieval error as a function of r_e for three different tangent heights. It can be clearly seen, that the retrieval error decreases with increasing r_e which is in line with the results presented in Fig. 5.7a. Panel c of Fig. 5.7 shows the Chappuis triplet for a cloudy atmosphere as a function of the r_e as well as the Chappuis triplet and the integrated weighting function for a cloud-free atmosphere. As clearly seen, the Chappuis triplet for a cloudy atmosphere decreases with increasing r_e getting closer to cloud-free values which results in smaller retrieval errors.

As shown by e.g., Kokhanovsky (2001), clouds having smaller water droplet effective radii reflect more solar radiation as compared to clouds consisting of larger water

droplets if all other cloud parameters are identical. This can be explained by the fact that the scattering phase function of larger water droplets is peaked much more strongly in the forward direction as compared to the smaller droplets. Thus, the probability of backward scattering (i.e., of the reflection) is lower for larger water droplets. As, according to our findings in Appendix A, for the typical atmospheric/observation conditions the Chappuis triplet has a similar behavior as the reflected solar radiation, one can conclude that the results shown in Fig. 5.7 are in agreement with the finding of Kokhanovsky (2001). We note, however, that because of a different viewing geometry and a combination of the limb radiances into the Chappuis triplet, the impact of the r_e observed in this study is much smaller compared to the results presented by Kokhanovsky (2001).

5.6.3 Cloud top height and geometrical thickness

Other cloud parameters that can affect the retrieval error include the geometrical thickness and cloud top height. As shown by Rozanov and Kokhanovsky (2008) (and references therein) these parameters play a major role when retrieving the vertical columns of ozone from the measurements of backscattered solar radiation in nadir viewing geometry. In this section, we analyze the impact of the cloud geometrical thickness and cloud top height on ozone vertical profiles retrieved from limb-scatter measurements. The calculations are performed for the parameter set given in Table 5.2. The left panel

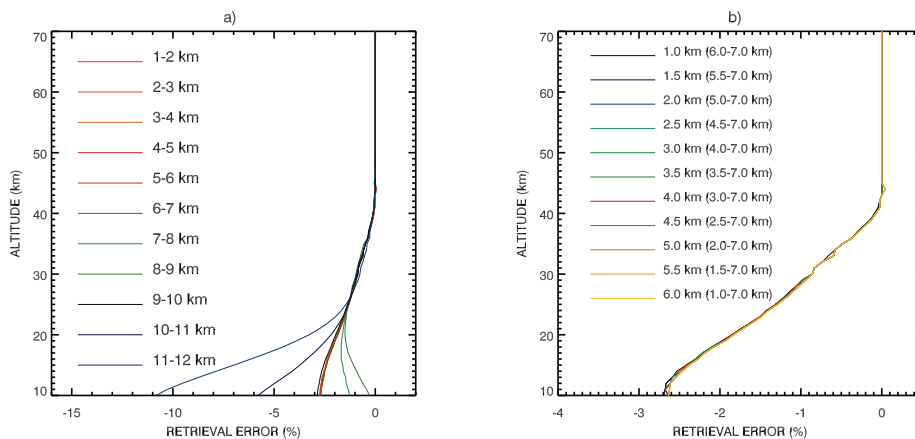


FIGURE 5.8: Relative errors in the retrieved ozone profiles due to neglect of clouds in the retrieval process. The results are shown for different cloud top heights and geometrical thicknesses of the cloud. Left panel: different cloud top heights for a fixed cloud geometrical thickness (1 km). Right panel: different cloud geometrical thicknesses for a fixed cloud top height (7 km). The calculations were performed for the parameter set given in Table 5.2.

of Fig. 5.8 illustrates the ozone profile retrieval errors due to neglect of clouds in the retrieval process for different cloud top heights. The results are obtained for a fixed cloud geometrical thickness of 1 km. As seen from the plot, the dependence of the retrieval error on the cloud top height is insignificant for cloud layers below 7 km. Because of a finite field of view the instrument directly observes the atmosphere down to about 7.5 km altitude at the lowest tangent height included in the retrieval (9 km). Thus, the reason for an increased dependence of the retrieval errors on cloud top height for the cloud layers above 7 km is that these clouds are already in the field of view of the instrument.

The right panel of Fig. 5.8 shows the ozone profile retrieval errors due to neglecting clouds in the retrieval process for different geometrical thicknesses of the cloud. In this comparison, the cloud top height is fixed to 7 km. As clearly seen, in contrast to nadir observations considered by [Rozanov and Kokhanovsky \(2008\)](#) the retrieval error for limb-scatter measurements is almost independent of the geometrical thickness of the cloud. Please note that the τ is fixed in this comparison, i.e., it does not change with a changing geometrical thickness of the cloud. The main reasons for the differences with respect to nadir observations are the combination of the limb radiances in the Chappuis triplet suppressing the overall impact of clouds.

5.6.4 Ground albedo

All results presented above are obtained assuming a constant surface albedo of 0.3 in both forward model and the retrieval algorithm. In this section, we investigate the influence of the surface albedo on the ozone vertical profiles retrieved neglecting the tropospheric clouds. For the first set of sensitivity studies presented in this section, the surface albedo is assumed to be known and the retrievals are performed using the correct values of the albedo, i.e., the surface albedo is the same when modeling the limb observations and when retrieving the profiles. Later we also discuss the effect of an incorrect surface albedo value on the ozone profile retrievals. The calculations are performed for a middle cloud with $\tau = 10$, and the other parameters as given in Table 5.2.

Panel a of Fig. 5.9 shows the relative error in the retrieved vertical distributions of ozone occurring for different surface albedo values when neglecting clouds in the retrieval process. As can be clearly seen, the impact of the surface albedo on the retrieval error is quite strong. In particular, the ozone concentrations are underestimated by up to 6.5% at 10 km altitude when neglecting clouds over dark surfaces ($A \sim 0.1$) whereas over bright surfaces ($A \sim 0.9$) an overestimation by up to 1.5% at 10 km is observed. Similar to all

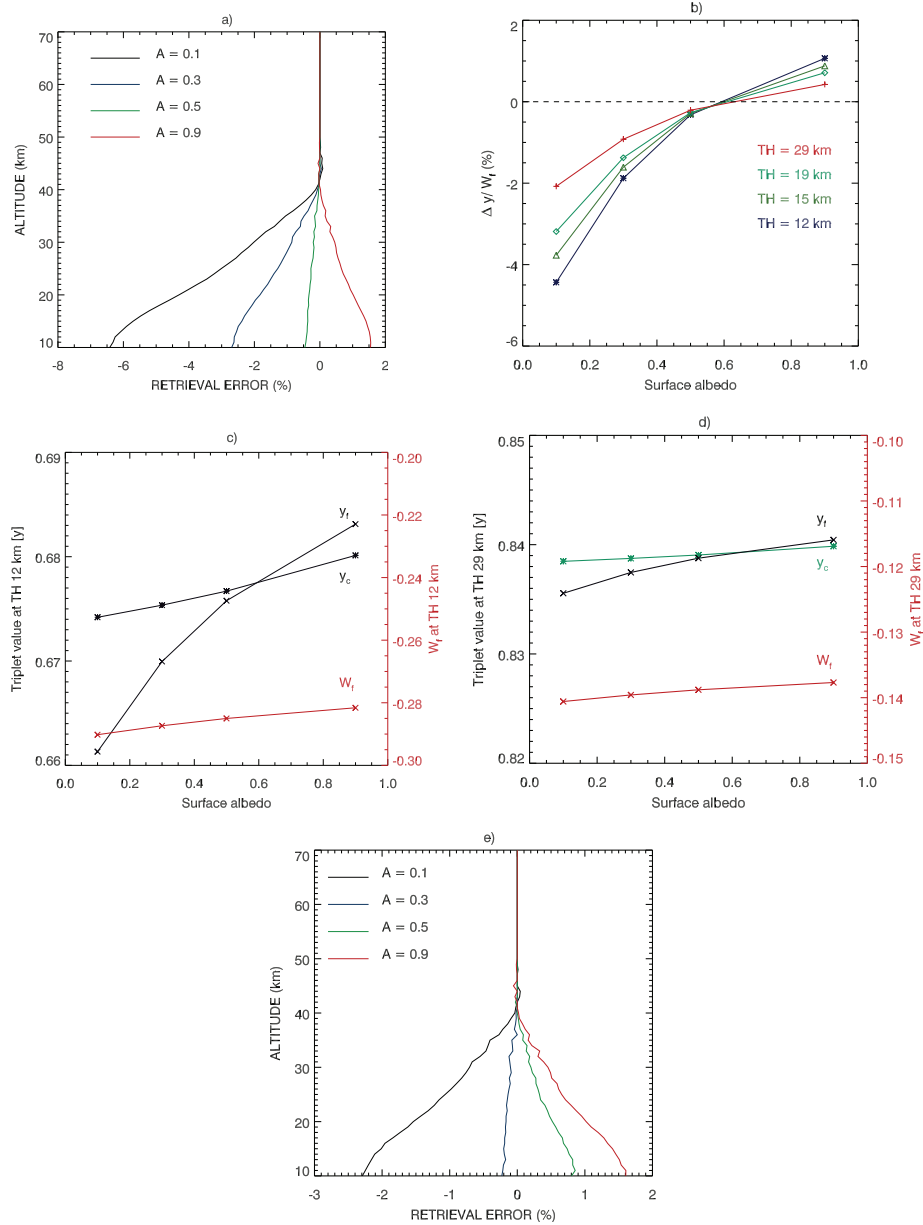


FIGURE 5.9: Panel a: relative errors in the retrieved ozone profiles due to neglect of clouds in the retrieval process for different surface albedos. Panel b: approximate retrieval error according to Eq. (5.13) at tangent heights of 12 km, 15 km, 19 km and 29 km as a function of the surface albedo. Panels c and d: Chappuis triplet for a cloudy and a cloud-free atmosphere as well as integrated weighting function at a tangent height of 12 km and 29 km respectively. The calculations were performed for a middle cloud, $\tau = 10$, and the parameter set given in Table 5.2. Panel e: same as the left top panel but τ of 2.

previous results, the retrieval error decreases with increasing altitude. In the considered case, the largest retrieval errors occur over the dark surfaces and the smallest effect is observed for a surface albedo of 0.5.

Similar to previous discussions, the obtained results can be explained considering the

approximate retrieval error as given by Eq. (5.13). Panel b of Fig. 5.9 shows the approximate retrieval error as a function of surface albedo for four different tangent heights. We observe that the approximate error shows the same behavior as the retrieval errors resulting from the full end-to-end numerical approach shown in panel a of the figure. Looking at Eq. (5.13), it is obvious that the behavior of the retrieval error can be analyzed considering the limb signals for a cloudy and a cloud-free atmosphere. Panels c and d of Fig. 5.9 show the Chappuis triplet for a cloudy and a cloud-free atmosphere as well as the integrated weighting function for a cloud-free atmosphere as functions of surface albedo for a tangent height of 12 km (panel c) and 29 km (panel d). It can be clearly seen, that both the Chappuis triplet for a cloudy and a cloud-free atmosphere increase with increasing surface albedo. However, the dependence for cloud free conditions is stronger. As, according to our findings in Appendix A, for the typical atmospheric/observation conditions the Chappuis triplet has a similar behavior as the reflected solar radiation, it is clear that it should increase with increasing surface albedo because more solar light is reflected and this increase should be smaller for a cloudy atmosphere because the surface is partially screened by the cloud.

For the case under consideration, $y_f < y_c$ for low surface albedo leading to negative retrieval errors whereas $y_f > y_c$ for high surface albedo resulting in positive retrieval errors (note that the integrated weighting function is negative). Thus, there is an albedo value at which the Chappuis triplets for a cloudy and a cloud-free atmosphere are equal and vertical profiles of ozone are retrieved without any error. However, the Chappuis triplet for a cloudy atmosphere, y_c , depends not only on the surface albedo but also on τ (see Fig. 5.6). Therefore, the curves representing y_c in Figs. 5.9c and 5.9d will be shifted upwards or downwards for clouds having τ greater or less than 10, respectively. Panel e of Fig. 5.9 shows the relative retrieval errors for different surface albedos and the same parameters as in the top left panel, except that the τ is 2. The maximum errors are lower than for a τ of 10. This panel clearly shows that the albedo leading to essentially zero retrieval errors is smaller than for $\tau = 10$, in agreement with the dependencies shown in the panels c and d of Fig. 5.9.

Taking into account that the Chappuis triplet for a cloud-free atmosphere, y_f , is independent of τ , one can conclude that the surface albedo value where $y_f \approx y_c$ (and the retrieval is done error-free) depends on τ . This consideration shows that the retrieval error caused by neglecting clouds can be decreased by including an effective surface albedo in the retrieval process. We note, that the mitigation of the impact of clouds on

the ozone profile retrievals by fitting an effective ground albedo has been considered in, e.g., [Rault \(2005\)](#) and [Roth et al. \(2007\)](#).

Now we discuss several cases where the actual surface albedo value is not exactly known, unlike the studies discussed earlier in this section. Panel a of Fig. 5.10 shows ozone profile retrieval errors assuming different albedo values in the forward simulation and an albedo of $A_r = 0.3$ for the retrievals. Panel b of the same figure shows the obtained retrieval errors based on a fixed surface albedo of $A_f = 0.3$ in the forward simulation of the synthetic observations, and different values for the surface albedo in the cloud-free retrieval. We note that the retrieval errors in panel b of Fig. 5.10 are very similar to the errors shown in the panel a of Fig. 5.9 for the same values of the albedo assumed in the retrievals. This finding is easily explained by panels c and d of Fig. 5.9 showing that the Chappuis triplet y_c for the cloudy case is only weakly dependent on surface albedo, whereas the triplet for the cloud-free case y_f shows a much stronger dependence. In other words, under cloudy conditions the effect of surface albedo on the Chappuis triplet is rather small compared to a cloud-free scenario. The ozone profile retrieval errors depend more strongly on the albedo value assumed in the cloud-free retrievals. This also explains, why the differences in retrieval errors between the different cases shown in panel a of Fig. 5.10 are smaller than in panel b. Finally, we note that the relative differences between the cases shown in panels a and b of Fig. 5.10 are consistent with the dependence of the cloudy and cloud-free Chappuis triplet values shown in the panels c and d of Fig. 5.9, and can be qualitatively derived immediately from these panels.

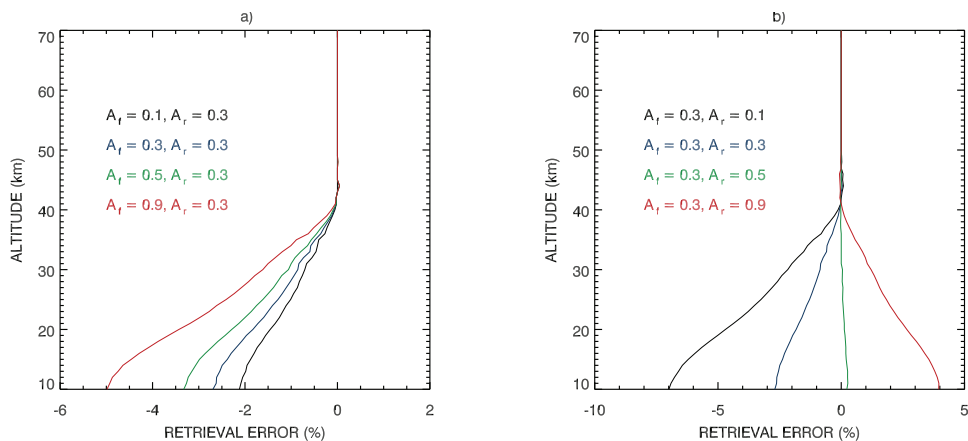


FIGURE 5.10: Relative ozone profile retrieval errors for different surface albedo values A_f in the forward simulations, but a fixed albedo $A_r = 0.3$ assumed in the retrievals (panel a), and a constant albedo of $A_f = 0.3$ in the forward simulations and varying albedo A_r used for the retrievals (panel b). The calculations were performed for the parameter set given in Table 5.2.

It is also noteworthy that for typical measurements over land and ocean the surface albedo is low and, thus, the retrieved ozone concentrations are generally underestimated if tropospheric clouds are not considered in the retrieval process (see Fig. 5.9a). This may be one of the reasons for the low bias observed in the vertical distributions of the stratospheric ozone retrieved from the OSIRIS limb-scatter observations when comparing to POAM III (von Savigny et al., 2005a) and ACE (Dupuy et al., 2009) solar occultation measurements.

5.6.5 Solar zenith and azimuthal angles

In this section, we discuss the influence of the viewing geometry, defined by the SZA and SAA, on the vertical distributions of ozone retrieved neglecting tropospheric clouds. Similar to previous investigations, all calculations are performed for the parameter set given in Table 5.2.

In Fig. 5.11, the relative errors in the retrieved ozone profiles for different SZAs and a fixed SAA of 90° are shown in the left panel. The right panel of Fig. 5.11 shows the retrieval errors for different SAAs and a fixed SZA of 30° . As can be clearly seen, the retrieval error increases with increasing SZA for $SZA < 75^\circ$ and then starts to decrease for $SZA > 80^\circ$. For a SZA of 85° the retrieval errors of similar magnitude as for 50° are observed. The maximum retrieval error of about 8% at 10 km altitude occurs for SZAs of 75° . Between 30° and 75° SZA the retrieval error changes by about 5% at 10 km altitude. The influence of the SAA on the ozone vertical profiles retrieved when neglecting tropospheric clouds is smaller than for the SZA and the maximum effect is observed at about 25 km altitude. For larger SAAs, the errors in the retrieved ozone profiles are smaller.

Similar to the discussion in the previous sections, the observed dependencies can be explained considering the approximate retrieval error as given by Eq. (5.13). The left panel of Fig. 5.12 shows the approximate retrieval error as a function of the SZA at different tangent heights. We clearly observe, that the retrieval error is always negative and shows a maximum (in absolute values) between 70° and 80° SZA decreasing for lower and higher Sun which is in line with the results presented in Fig. 5.11a. A further analysis can be done considering the dependence of the Chappuis triplets on the SZA for a cloudy and for a cloud-free atmosphere as well as of the cloud-free integrated weighting function as shown in the right panel of Fig. 5.12. As clearly seen, both the Chappuis triplet for a cloudy and for a cloud-free atmosphere decrease with increasing SZA. The

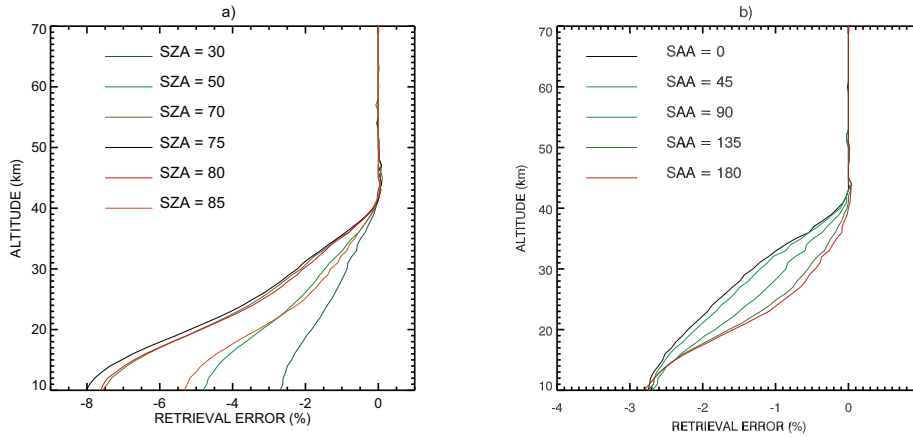


FIGURE 5.11: Relative errors in the retrieved ozone profiles due to neglect of clouds in the retrieval process for different viewing geometries. Left panel: retrieval errors for different SZAs and a fixed SAA of 90° . Right panel: retrieval errors for different SAAs and a fixed SZA of 30° . The calculations were performed for the scenario as given in Table 5.2.

Chappuis triplet for a cloudy atmosphere is always larger than that for a cloud-free atmosphere resulting in an underestimation of the ozone concentrations retrieved neglecting the tropospheric clouds (the retrieval error is negative because of the negative integrated weighting function). As follows from the results presented among others by Liou (1973) and Kokhanovsky (2001) for the reflection function of clouds in the visible spectral range, the reflected solar radiation in a cloudy atmosphere decreases with increasing SZA. This explains the observed dependencies for the Chappuis triplet taking into account that, according to our findings in Appendix A, for the typical atmospheric/observation conditions the Chappuis triplet has a similar behavior as the reflected solar radiation.

In addition, we investigated the ozone profile retrieval errors occurring when neglecting tropospheric clouds for the viewing geometries typical for the Scanning Imaging Absorption Spectrometer for Atmospheric CHartography (SCIAMACHY) and the Optical Spectrograph and InfraRed Imager System (OSIRIS) instruments. A detailed description of the instruments was presented by Bovensmann et al. (1999) and Llewellyn et al. (2004), respectively. Both Envisat carrying the SCIAMACHY instrument and Odin with the OSIRIS instrument on board are in sun-synchronous polar orbits. SCIAMACHY/Envisat observes scattered, reflected and transmitted solar radiation in nadir, limb-scatter, and solar/lunar occultation modes whereas OSIRIS/Odin performs only limb-scatter observations. The comparison is performed for the viewing conditions of seven SCIAMACHY limb observations (orbit 27746 on 21 June 2007) and for nine

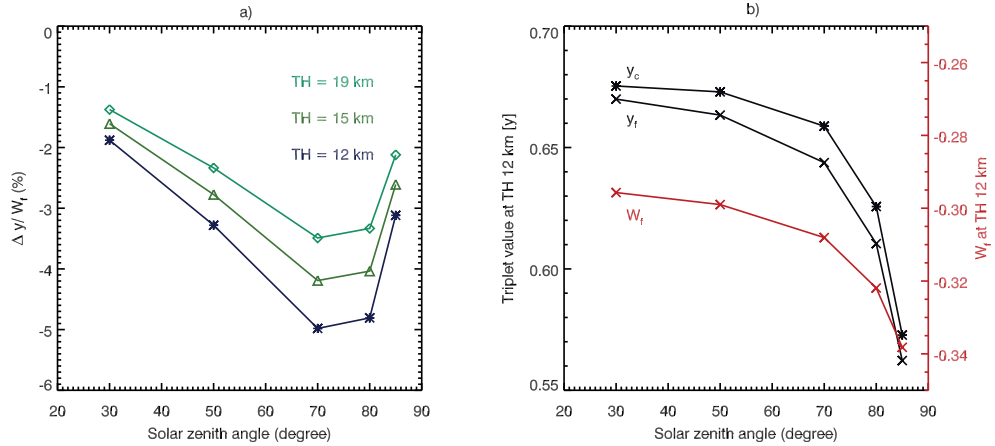


FIGURE 5.12: Left panel: approximate retrieval error according to Eq. (5.13) at tangent heights of 12 km, 15 km, and 19 km as a function of the SZA. Right panel: Chapuis triplet for a cloudy and a cloud-free atmosphere as well as integrated weighting function at a tangent height of 12 km. The calculations were performed for a middle cloud (the same scenario as in Fig. 5.11).

combinations of the SZA and SAA which roughly cover the full range of the angles typical for the OSIRIS observations. It is also worth noting that the viewing geometry of the OMPS (Ozone Mapping and Profiler Suite) instrument which will fly on the next generation of US operational polar-orbiting satellites, the National Polar-orbiting Operational Environmental Satellite System (NPOESS), is very similar to that of SCIAMACHY limb-scatter observations.

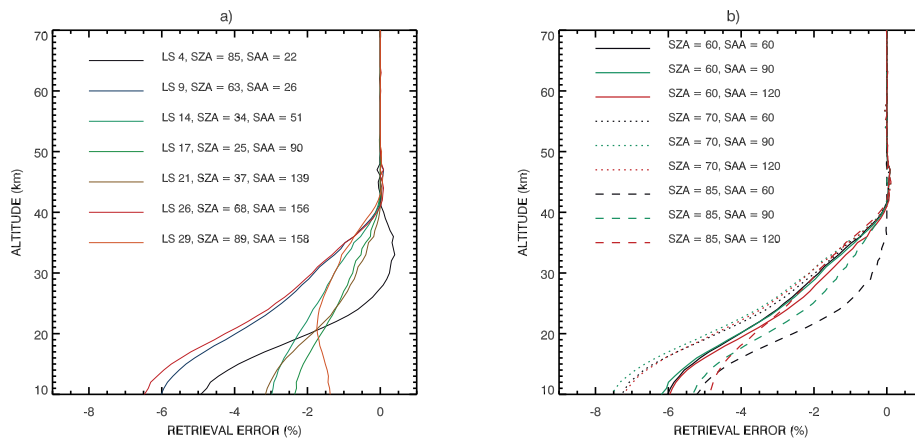


FIGURE 5.13: Relative errors in the retrieved ozone profiles due to neglect of clouds in the retrieval process for viewing geometries typical for SCIAMACHY (left panel) and OSIRIS (right panel) measurements. The calculations were performed for a middle cloud (the same scenario as in Fig. 5.11).

The relative retrieval errors for the SCIAMACHY viewing geometry are shown in the left panel of Fig. 5.13. In agreement with the results shown in Fig. 5.11, the largest

retrieval errors occur at SZAs close to 70° . For the considered Envisat orbit, the worst viewing conditions in terms of the sensitivity of the ozone vertical profile retrievals to tropospheric clouds are at $SZA = 68^\circ$ and $SAA = 156^\circ$ corresponding to observations at southern mid-latitudes and the second worst conditions at $SZA = 63^\circ$ and $SAA = 26^\circ$ correspond to observations at high northern latitudes. The smallest retrieval errors are observed for $SZA = 25^\circ$ and $SAA = 90^\circ$ corresponding to measurements in the tropical region.

The relative retrieval errors for the OSIRIS viewing geometry are shown in the right panel of Fig. 5.13. As expected from Fig. 5.11, the largest retrieval errors occur for a SZA of 70° getting smaller for the lower and higher Sun. The dependence on the SAA is weaker as compared to the SZA and is only significant for $SZA = 85^\circ$.

5.6.6 Most frequent clouds

In this section, we investigate the relative retrieval errors occurring for the most frequent clouds observed in the Earth's atmosphere. The comparisons are performed for three typical viewing geometries of the SCIAMACHY instrument corresponding to a high, moderate, and low sensitivity of the ozone profile retrievals to the tropospheric clouds (see Sec. 5.6.5). According to the results published by [Rozanov and Kokhanovsky \(2006\)](#), tropospheric clouds typically extend from 0.5 to 7.5 km with most frequent values of the geometrical thickness of about 3 km. As demonstrated in previous sections, the ozone profile retrievals exhibit similar sensitivity to low and middle clouds. Therefore, in this study a cloud extending from 4 to 7 km altitude is considered to be representative for the most frequent clouds in the Earth's atmosphere. Based on the results published by [Trishchenko et al. \(2001\)](#) and [Kokhanovsky \(2006\)](#), respectively, values of $\tau = 10$ and $r_e = 8 \mu\text{m}$ are considered to be representative for the most frequent clouds. As before, the calculations are performed for a surface albedo of 0.3.

The ozone vertical profile retrieval errors for the most frequent clouds are shown in Fig. 5.14 for three typical SCIAMACHY limb observations having low, moderate, and high sensitivity to tropospheric clouds. During the northern hemispheric summer these viewing conditions occur in the tropical region ($SZA = 25^\circ$ and $SAA = 90^\circ$), at northern high latitudes ($SZA = 85^\circ$ and $SAA = 22^\circ$), and at southern mid-latitudes ($SZA = 68^\circ$ and $SAA = 156^\circ$). The obtained results are summarized in Table 5.3.

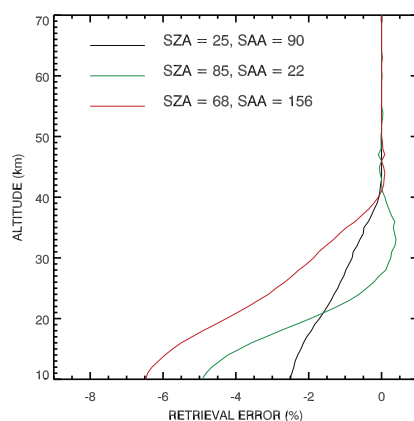


FIGURE 5.14: Relative errors in the retrieved ozone profiles due to neglect of clouds in the retrieval process for most frequent clouds for typical viewing geometries of the SCIAMACHY instrument. The calculations were performed with the scenario as given in Table 5.2.

TABLE 5.3: Overview of the sensitivity of ozone vertical profile retrievals to the tropospheric clouds (relative retrieval error in % is shown) for the most frequent clouds¹ for typical viewing geometries of the SCIAMACHY instrument.

Viewing geometries	15 km	20 km	30 km	40 km	50 km	60 km
² SZA = 25°, SAA = 90°	<2.5	<2	<1	<0.5	<0.1	<0.1
³ SZA = 85°, SAA = 22°	<4	<2	<1	<0.5	<0.1	<0.1
⁴ SZA = 68°, SAA = 156°	<6	<5	<2	<0.5	<0.1	<0.1

¹ cloud extension 4 – 7 km, $\tau = 10$, $r_e = 8 \mu\text{m}$, ² Low sensitivity, ³ Moderate sensitivity, ⁴ High sensitivity

5.7 Concluding remarks on the cloud sensitivity of ozone profile retrievals

This chapter has presented the sensitivity of stratospheric and lower mesospheric ozone retrievals from limb-scattered radiance measurements to tropospheric clouds using the SCIATRAN radiative transfer model and retrieval package. The outgoing radiance observed by the instrument is much more sensitive to tropospheric clouds in the visible spectral range than in the UV. Thus, the retrievals are mostly affected by the changes of the Chappuis triplet in a cloudy atmosphere. The maximum retrieval errors are observed in the lower stratosphere. The retrieval errors decrease with increasing altitude and become negligible at about 40 km for all considered scenarios.

The surface albedo, τ , and SZA are found to have the strongest effect on the retrieved ozone profiles whereas the impact of the r_e , SAA, cloud geometrical thickness, and

cloud top height is rather small. The latter however, is only the case if the clouds are outside the field of view of the instrument and the cloud optical thickness is not changed when changing the geometrical thickness of the cloud or the effective radius of water droplets. For the most frequent clouds, the ozone vertical profile retrieval error is below 6% at 15 – 20 km altitudes and less than 5% above 20 km for typical viewing geometries of the SCIAMACHY instrument.

Beside the investigation of the ozone retrieval errors, we have introduced an approximate method, see Eq. (5.13), which can be used to estimate the ozone retrieval errors due to neglecting clouds in the retrieval process without solving the full inverse problem.

Chapter 6

Retrieval of the polar chemical ozone loss using SCIAMACHY limb measurements

Stratospheric ozone depletion through catalytic chemistry is one of the global issues for atmospheric research. This chapter presents the quantification of ozone depletion by chemical processes derived from the SCIAMACHY limb ozone profile data product described in chapter 4. The SCIAMACHY instrument has been operational since August, 2002; hence, the following results deal with the chemical ozone loss over the Arctic from 2003–2009 and Antarctic from 2002–2008 during winter–spring time. The ozone depletion is largely confined to altitudes from 12–25 km. The ozone depletion at the 450 K – 600 K isentropic levels or about 18–25 km will be focused on in this work, as the validation of the ozone profile data product has shown (see section 4.5) good agreement of the SCIAMACHY ozone profiles with independent measurements in the 18–25 km range

This chapter is divided into 5 sections as described in the following. A brief summary of four methods to quantify chemical ozone loss is given in the first section. Of these, the polar vortex averaging method is chosen to determine the chemical ozone loss from SCIAMACHY limb observations. Section 2 presents the potential vorticity in the Arctic and Antarctic stratospheres as the indicator of polar vortex air. Section 3 shows the chemical ozone loss results in the polar Arctic and Antarctic stratospheres, respectively. The derived chemical ozone loss results and polar stratospheric cloud appearances are shown in section 4. Section 5 presents a comparison of the chemical ozone loss derived

from SCIAMACHY limb measurements with other instruments/techniques. Finally, the conclusions are provided in the last section.

6.1 The chemical ozone loss algorithms

The current knowledge on the catalytical ozone loss processes in the polar stratosphere was briefly summarized in section 2.1. The quantification of the stratospheric ozone loss resulting from the catalytical processes was widely studied in recent years. However, no direct observations of the chemical ozone loss exist. The chemical loss must be inferred from measurements of the ozone with consideration of dynamical processes. In order to determine the variation of ozone due solely to chemical processes, the dynamical and chemical variations must be separated in the observed ozone fields. The methods to quantify the photochemical loss have been divided by Singleton et al. (2005) into four techniques, as summarized below.

1. The Match technique quantifies photochemical ozone loss by simulating the forward trajectory of an air parcel that has been probed by an ozone measurement (e.g., by an ozonesonde or satellite instrument) and finding a second ozone measurement close to this trajectory. Such an event is called a "match". The rate of chemical ozone destruction can be obtained by a statistical analysis of several tens of such match events (e.g., Rex et al., 2003; Lehmann et al., 2005 and references therein).
2. The Tracer Correlation technique removes the effect of transport by comparing the pre-winter and post-winter ratios between ozone volume mixing ratio and an inert tracer, such as nitrous oxide (N_2O) or methane (CH_4) inside the vortex (Profitt et al., 1990, Müller et al., 1997; Müller et al., 2001). This method assumes that the ozone/tracer relationship is constant and any post-winter deviations from the pre-winter relationship are interpreted as chemically induced.
3. The Passive Subtraction technique, i.e., ozone is simulated as a passive tracer. The passive ozone is subtracted from ozone measurements to quantify the change in ozone due to chemistry (e.g., Manney et al., 1995a; Manney et al., 1995b).
4. The Vortex Average technique quantifies dynamical variation for an average ozone profile inside the vortex by calculating vortex average descent rates using a radiative transfer model. The dynamical contribution to ozone change inside the

vortex is assumed to be dominated by diabatic descent. It is assumed that mixing between vortex and extra-vortex air is minimal; therefore, only vertical transport is considered (e.g., [Knudsen et al., 1998](#); [Eichmann et al., 2002](#); [Hoppel et al., 2002](#)).

The vortex average approach is used in this work and we now briefly explain the algorithms used to determine the chemical ozone loss inside the polar vortices. The algorithm used for calculating the chemical ozone loss is the SODD (SCIAMACHY Ozone and Diabatic Descent) program package. SODD is based on the FUDD (FUrm ozone and Diabatic Descent - where FURM stands for FULL Retrieval Method ([Hoogen et al., 1999](#)) program suite that has initially been developed to calculate the chemical ozone loss from GOME (Global Ozone Monitoring Experiment) ozone profile retrievals ([Eichmann et al., 2002](#)). In this work, the SODD program package was extended to calculate the chemical ozone loss in the Antarctic polar vortex. The SODD program package is used to calculate the chemical ozone loss in the polar vortex by considering the United Kingdom Meteorological Office (UKMO) stratospheric assimilation data¹ and the SCIAMACHY ozone profiles described in sections 4.4 and 4.5. The algorithm used for calculating the chemical ozone loss by the SODD program consists of 4 parts.

1. The extent of the polar vortex is determined from potential vorticity (PV) values (as described in section 2.3.2) using the UKMO meteorological analysis, i.e., pressure, temperature, zonal and meridional wind data on pressure levels.
2. At all locations inside the polar vortex corresponding to the SCIAMACHY observation locations, the daily ozone concentration changes at the considered isentropic level due to diabatic descent are computed as described in section 2.3.1. The temporal change in ozone mixing ratio on an isentropic level caused by vertical transport is computed following Eq. 2.36. Based on the MIDRAD radiative transfer model ([Shine, 1991](#)), the diabatic heating rate is computed in the SODD program that uses temperature and pressure profiles taken from the UKMO stratospheric assimilation. MIDRAD is run for the conditions at the geolocations of all SCIAMACHY observations on a given day. Information on the short wavelength

¹ UK Met Office provides sets of 3-dimensional gridpoint data. The data files contain temperature, geopotential height and wind components. The data assimilation system is a development of the scheme used at the Meteorological Office for operational weather forecasting, which has been extended to cover the stratosphere. From October 1991 to March 2006, data are provided on standard UARS pressure levels (22 layers) from 1000 hPa to 0.316 hPa and on a 2.5° latitude by 3.75° longitude global grid. Since March 2006, data have been provided at increased resolution from 1000 hPa to 0.1 hPa pressure levels (26, 27, or 30 depending on variable) and on a 0.5625° latitude by 0.375° longitude global grid.

absorption by ozone and the long wavelength absorption and emission by water vapor and carbon dioxide in the stratosphere are required for the calculation. The CO₂ mixing ratio is assumed to be constant at a value of 378 ppmv and the water vapour profiles are taken from the UARS/HALOE climatology (Randel et al., 1998) as in Eichmann et al. (2002). Because during winter/spring most of high latitude regions are covered with ice and snow, the surface albedo is set to 0.7 in the model. Note that, a test run was performed with an albedo of 0.9, and the resulting model output was only negligibly different from the run with an albedo of 0.7. In this work, the chemical ozone loss at isentropic levels of 450 K - 600 K potential temperature in 25 K intervals are computed.

3. The accumulated ozone abundances from the daily diabatic ozone descent are calculated at each isentropic level starting from a chosen date.
4. The chemical ozone loss is calculated by subtracting the dynamically accumulated ozone from the observed ozone mixing ratios following Eq. 2.34. This implies that the approach is based on the assumption, that the vortex air masses are well contained inside the polar vortex, i.e., transport across the vortex boundaries is neglected.

6.2 Polar vortex position

As explained in section 2.3.2, the PV value is used to establish the extent of the polar vortex. In this study, the modified potential vorticity (MPV) unit with $\Theta_0 = 475$ K is used as described in Eq. 2.41. Different studies have used different MPV thresholds for the identification of vortex air; for example, Christensen et al. (2005) used MPV values between 28 and 40 MPVU depending on Θ levels and studied periods, Eichmann et al. (2002) used 38 PVU for $\Theta = 475$ K. In this work, the $MPV > 38$ MPVU is used for all Θ levels. By employing the assimilated UKMO data, the MPV values are calculated at seven isentropic levels that are $\Theta = 450, 475, 500, 525, 550, 575,$ and 600 K. The MPV values at the 475 K isentropic level (about 18 km) were selected to be shown here.

Fig. 6.1 and Fig. 6.2 show the daily and zonally averaged (Fig. 6.1) and maximum (Fig. 6.2) modified potential vorticity values averaged over 5° latitude bins in the Arctic stratosphere region sampled at the geolocations of the SCIAMACHY observations and at the 475K isentropic level for the periods October to April, 2003–2009. SCIAMACHY typically starts sampling the polar vortex in late December/early January as

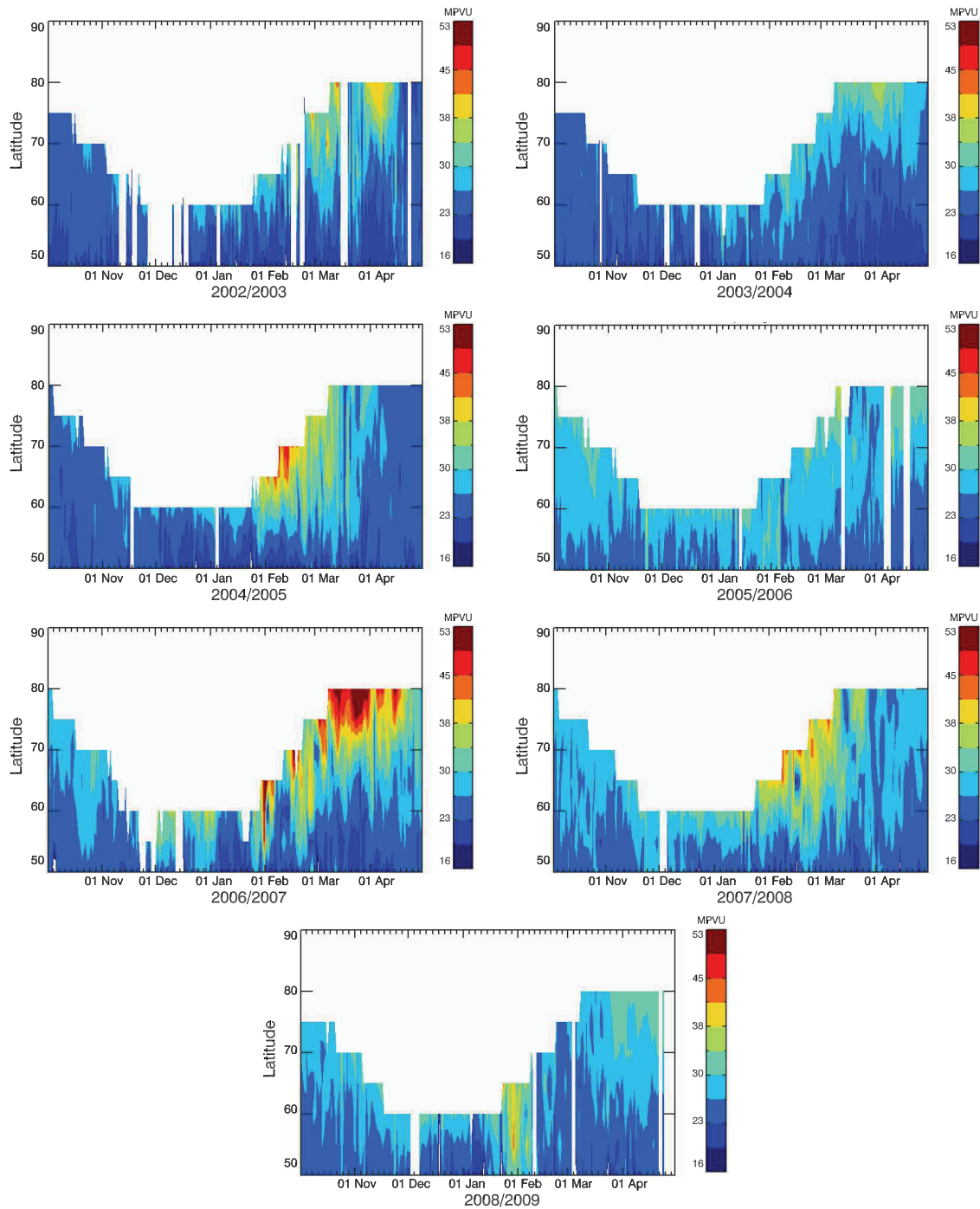


FIGURE 6.1: The daily and zonally averaged modified potential vorticity at the 475 K isentropic level in the Arctic stratosphere for latitudes of SCIAMACHY observations in 2002 – 2009 during winter – spring (given in modified potential vorticity unit (MPVU)). Data were averaged over 5° latitude bins.

can be seen in Fig. 6.2. The daily maximum potential vorticity in Fig. 6.2 shows that the polar vortex dominated at latitudes above 50°N . The existence of the polar vortex – at the locations sampled by SCIAMACHY – occurred during November – December as can be seen from the daily maximum potential vorticity in Fig. 6.2. A strong polar

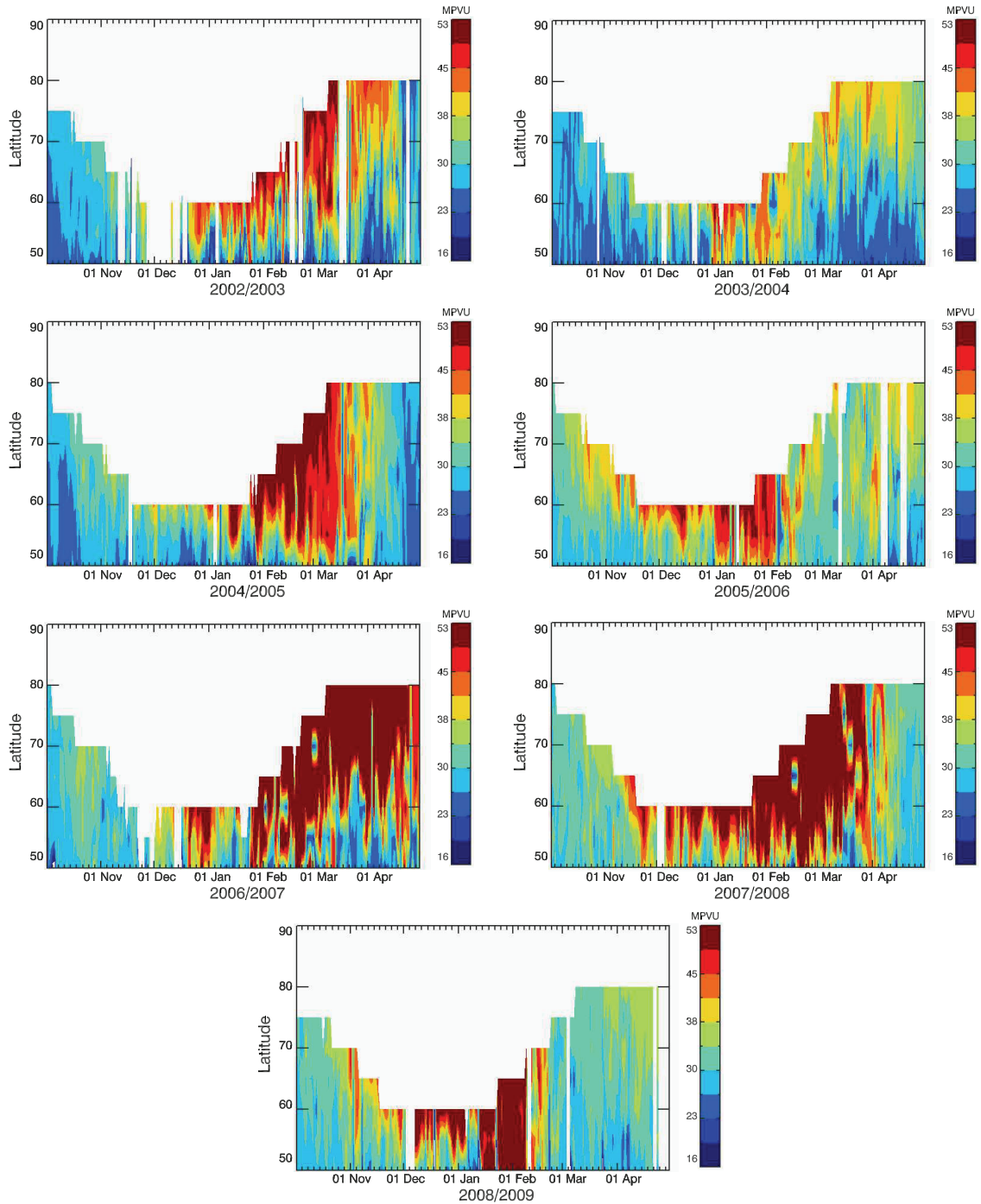


FIGURE 6.2: The daily and zonal maximum modified potential vorticity at the 475 K isentropic level in the Arctic stratosphere for the latitudes of SCIAMACHY observations in 2002 – 2009 during winter – spring.

vortex did not form in every year as can be clearly seen the modified potential vorticity values shown in Fig. 6.1. The colder winters 2002/2003, 2004/2005, 2006/2007,

and 2007/2008 show relatively large averaged modified potential vorticity values compared to the warmer winters 2003/2004 and 2005/2006. The appearance of high potential vorticity is in good correspondence with stratospheric temperature data. Temperature observations with the Sounding of the Atmosphere using Broadband Emission Radiometry (SABER) instrument (version 01.07) are shown for the polar northern winters 2002/2003 – 2008/2009 in Fig. 6.3. The long periods of low temperature in the lower stratosphere, around 18 – 20 km, were observed during northern winters 2002/2003, 2004/2005, 2006/2007 and 2007/2008.

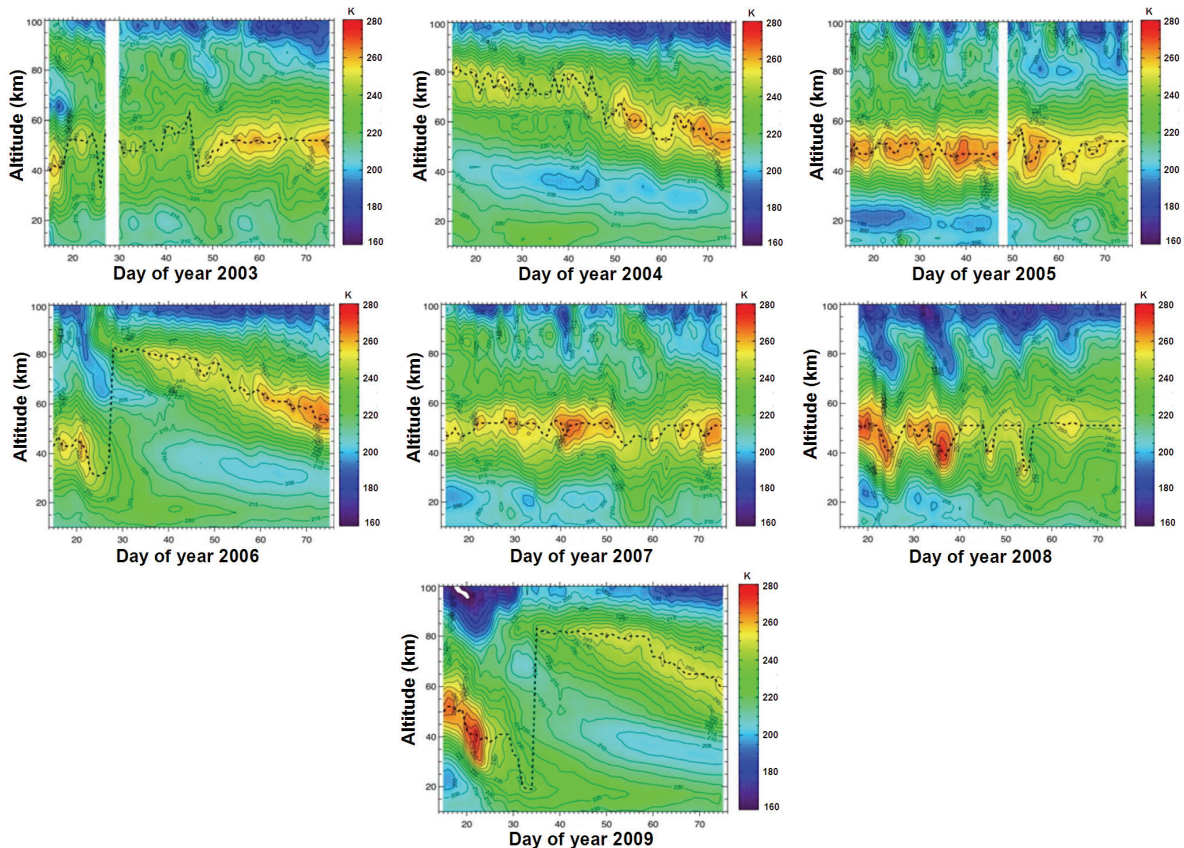


FIGURE 6.3: SABER V01.07 temperature data over the Arctic region (70°N – 90°N) in the winters of 2003–2009. The dashed line illustrates the daily highest temperature. (The figure is taken from the presentation of Fussen, D. from the Atmospheric science conference, Barcelona, 2009.)

In 2005/2006 and 2008/2009 major stratospheric sudden warmings (SSWs) occurred, as can be seen from the dashed line in Fig. 6.3. These events correspond to the sudden drop in enhanced potential vorticity occurring in the first half of February in 2006 and 2009. The major SSWs penetrated from the middle stratosphere to the lower stratosphere and broke up the polar vortex which has been reported by, e.g., [Manney et al. \(2005a, 2009\)](#), and [Sathishkumar et al. \(2009\)](#).

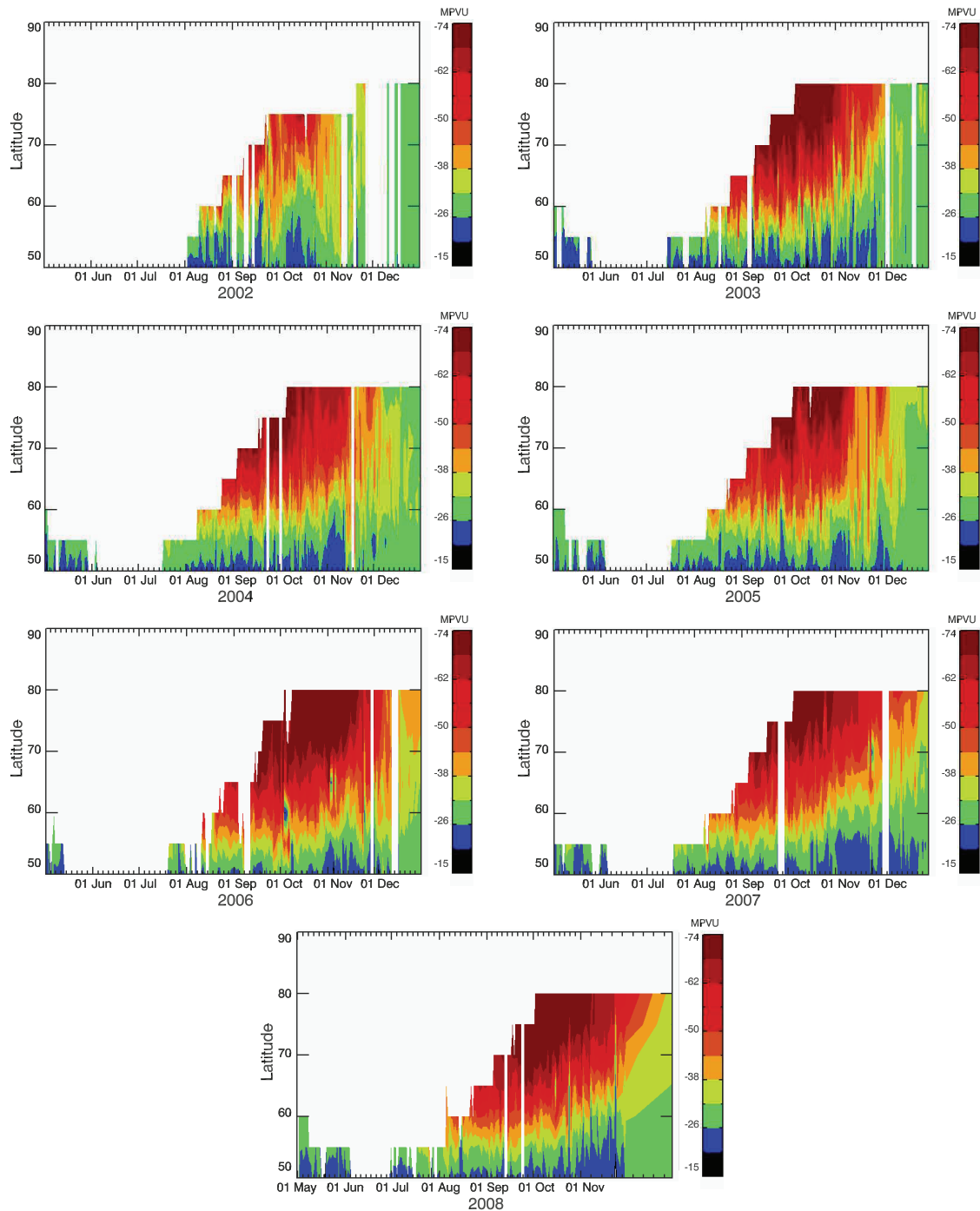


FIGURE 6.4: The daily and zonally averaged modified potential vorticity at the 475 K isentropic level in the Antarctic stratosphere for the latitudes of SCIAMACHY observations in 2002 – 2008 during winter – spring.

Fig. 6.4 and Fig. 6.5 show the daily and zonally averaged as well as the minimum modified potential vorticity values in the Antarctic stratosphere at the 475K isentropic level corresponding to geolocations of SCIAMACHY observations and the period May to December 2003–2009. The daily averaged and minimum modified potential vorticity

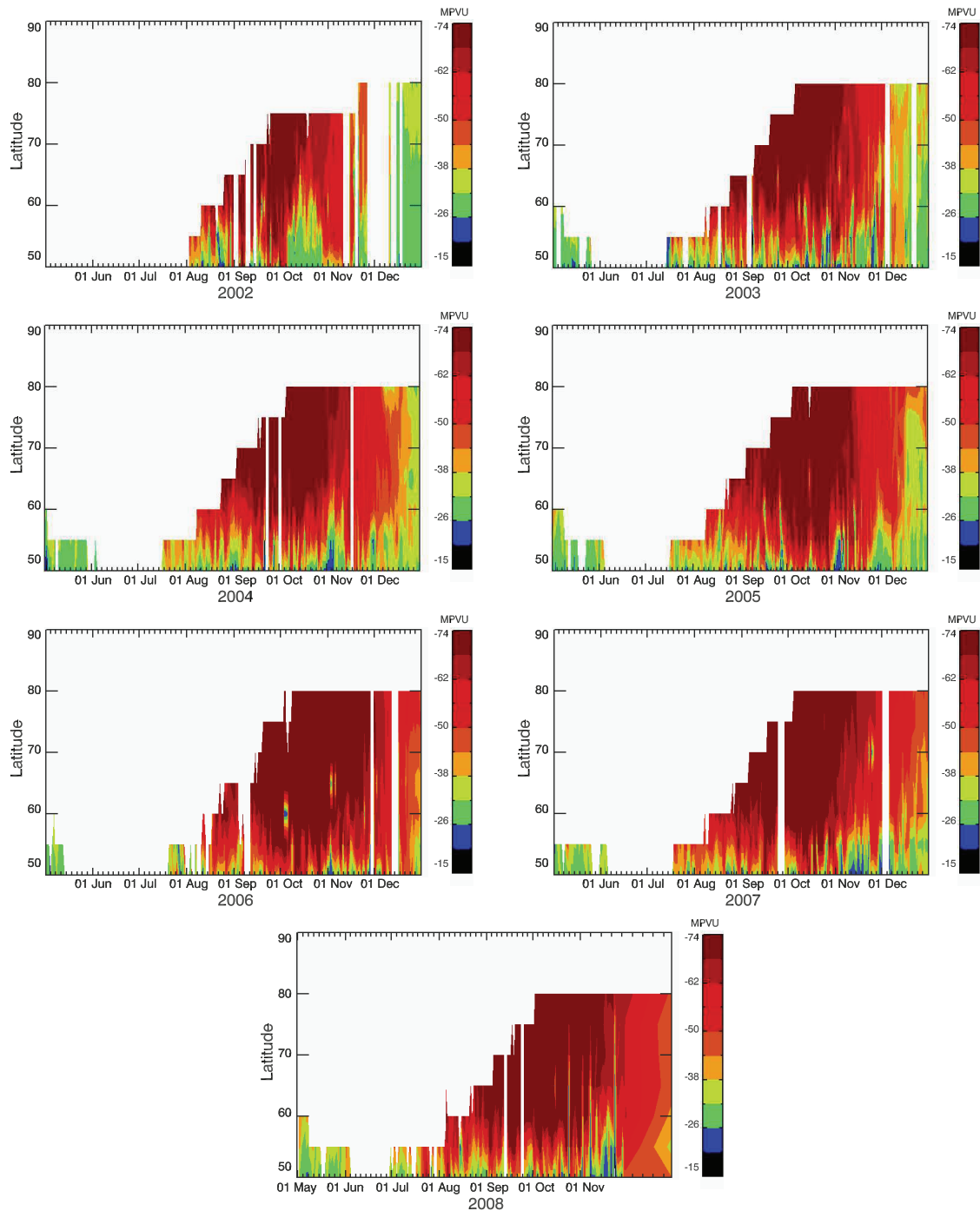


FIGURE 6.5: The daily and zonal minimum modified potential vorticity at the 475 K isentropic level in the Antarctic stratosphere for the latitudes of SCIAMACHY observations in 2002 – 2008 during winter – spring.

values in Fig. 6.4 and Fig. 6.5 show that the polar vortex is essentially limited to latitudes above 50° – 55° S. These figures indicate much less interannual variability in the southern polar winter stratosphere as compared to the northern hemisphere. Note, that SCIAMACHY can not observe the Antarctic region at high latitudes during June to

July as explained in section 3.2.3, thus the initial formation of the polar vortex cannot be seen in Fig. 6.4 or Fig. 6.5.

In general, the two hemispheres exhibit significant differences in terms of the dynamical situation of the polar winter stratosphere. The polar vortex over the Arctic region has been sampled by SCIAMACHY in the cold winters where the lower stratosphere was very cold and a stable vortex prevailed from November to March. By mid-April the influence of several warmings typically leads to the perturbation and break-up of vortex in the Arctic. The Antarctic vortex is characterized by a longer duration, larger extent, and higher stability as compared to the Arctic (e.g., Solomon, 1999; Weber et al., 2003). This is because the Rossby wave activity, which is driven by zonal land-sea contrasts and topography, is generally stronger and more variable in the northern hemisphere than in the southern hemisphere.

6.3 The chemical ozone loss from the vortex average method

Using the vortex average approach, only the ozone mixing ratio inside the polar vortex is employed to be averaged on a certain isentropic level. This section presents the ozone depletion focusing on both the Arctic and Antarctic stratospheric regions and the 450–600 K isentropic levels.

6.3.1 Arctic chemical ozone loss

Fig. 6.6a shows daily averaged ozone mixing ratios at the 475 K isentropic level derived from SCIAMACHY limb measurements inside the polar vortex over the Arctic. The 1σ statistical error bar is shown only for the selected year 2005. Days with missing data and days where the SCIAMACHY instrument did not sample the vortex have been filled in with a spline interpolation. The solid lines show the time series smoothed with a 3-day boxcar function. Because the dynamical situation in the Arctic is much more variable than in the southern hemisphere, the reference date for the determination of the accumulated ozone loss inside the vortex was chosen individually for every season as given in Table 6.1. The beginning day of the studied period is selected as the first spike in ozone mixing ratio in January of each year. This choice is arbitrary to a certain

extent, and will affect the derived total relative ozone losses somewhat, but it does not affect the main conclusions of this study.

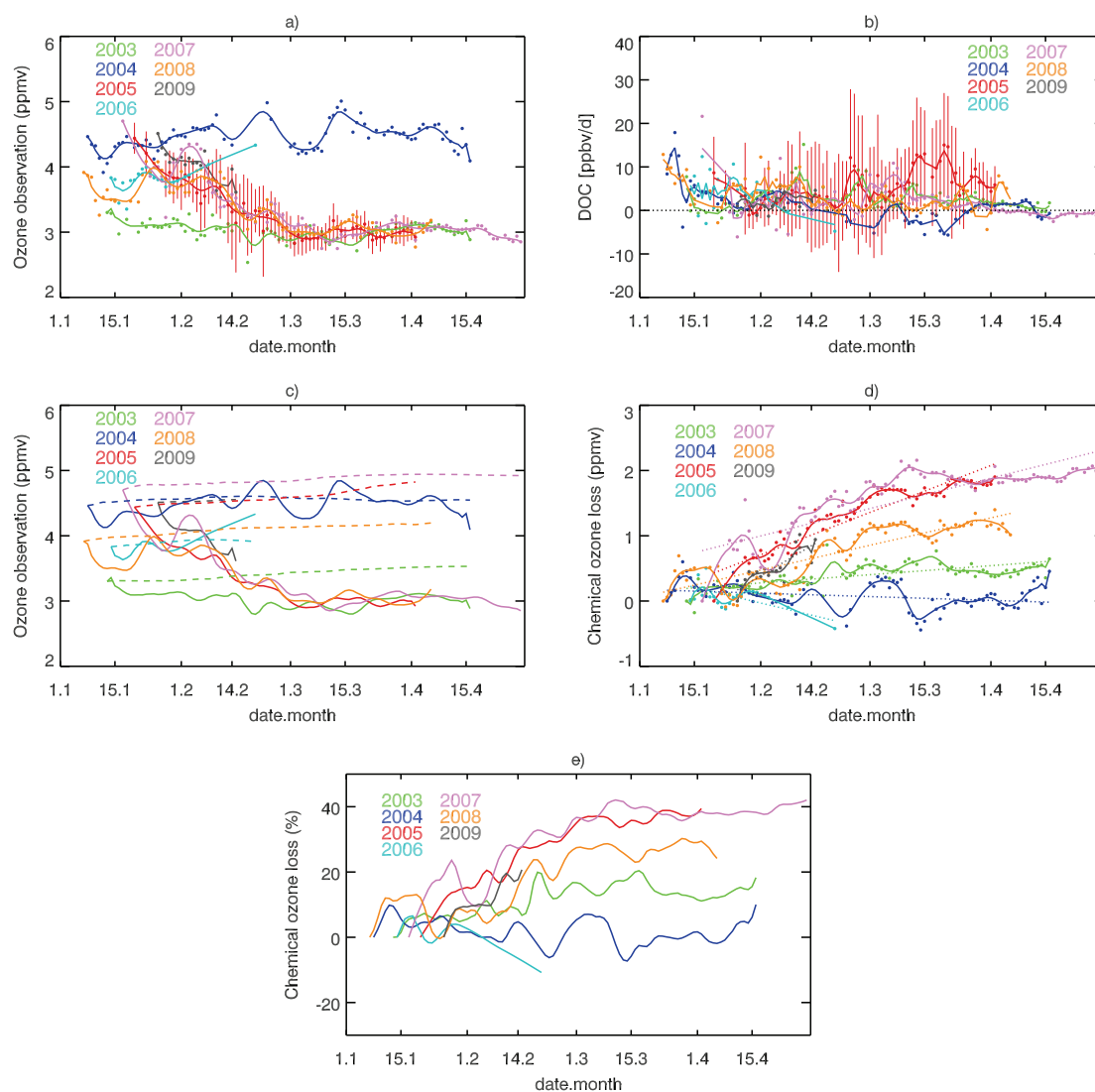


FIGURE 6.6: Panel a): observed changes in ozone mixing ratio, panel b): daily change in ozone mixing ratio due to diabatic descent determined with MIRAD model simulations, panel c): accumulated ozone mixing ratio from daily diabatic descent (dashed line) and the observed ozone mixing ratio (solid line), panel d): chemical ozone loss in ppmv (solid line) and the linear fit to the chemical ozone loss (dashed line), and panel e): chemical ozone loss in percent from SCIAMACHY observations at the 475 K isentropic level in the Arctic stratosphere in 2003 – 2009 during winter – spring.

The daily changes of ozone mixing ratio due to vertical transport associated with diabatic cooling are determined at each isentropic level. The computed daily ozone change (DOC) rate due to diabatic descent (or ascent) in ppbv/day for the Arctic region at the 475 K isentropic level are shown in panel b of Fig. 6.6. Apparently the daily ozone change rates inside the Arctic vortex vary from year to year. Especially in March of

2005, unusual dynamically induced ozone changes at the 475 K isentropic level were observed (panel b of Fig. 6.6). An episode with negative diabatic ozone change values was detected in 2004 (in dark blue line). This period corresponds to the unique characteristics of a stratospheric warming as described by Manney et al. (2005a). The diabatic ozone change rate inside the vortex was large during early January of 2004. The major warming during January and February led to unusual variability of the diabatic ozone descent rate.

The accumulated diabatic ozone change was calculated from the beginning of the studied period and is displayed as a dashed line in panel c of Fig. 6.6 for the Arctic polar vortex. The chemical ozone loss inside the vortex is then determined by subtracting the observed vortex average ozone mixing ratio from the accumulated diabatic ozone descent. The resulting chemical ozone loss time series are shown as solid lines in panel d. The dotted lines in the same panel represent linear fits to the chemical ozone loss time series. Panel e of Fig. 6.6 presents the relative chemical ozone loss in percent established from the solid line of panel d – relative to the start dates listed in Table 6.1.

The chemical ozone losses inside the polar vortex in the Arctic stratosphere exhibit a strong inter-annual variability. The maximum absolute ozone loss derived for the winters 2002/2003 to 2008/2009 inside the Arctic vortex is about 2 ppmv (corresponding to relative losses of 40%) and occurred in March of the years 2005 and 2007. In March 2008 an absolute loss at the 475 K isentropic level inside the Arctic vortex of about 1 ppmv is retrieved (20 - 30%), and for spring 2004 and 2006 no indications for significant chemical ozone losses were observed.

The derived daily chemical ozone loss rates for the Arctic polar vortex are summarized in Table 6.1. The daily ozone loss rates were determined in two different ways: (a) by taking the average loss rate over the periods considered (4th column in Table 6.1); and (b) from the linear fits shown in panel d of Fig. 6.6 (5th column in Table 6.1). The results in Table 6.1 show that the calculated chemical ozone loss rates from the linear fit and from the start-end days of the studied period may differ by several ppbv per day, but they are more or less consistent, especially in terms of their inter-annual differences.

The highest chemical ozone loss rate over the Arctic stratospheric region is observed in 2009. However, it occurred only in the short period during the end of January and the first half of February. This is because the lower stratosphere was cold. At the end of January, a SSW occurred and limited the chemical ozone depletion processes. The stratospheric temperature changes of this year are also shown in Fig. 6.3. A SSW event

TABLE 6.1: The chemical ozone loss rate in the Arctic during 2003–2009 at the 475 K isentropic level between the start and end dates listed.

Year	Studied period of each year		Chemical O ₃ loss	
	Start date	End date	ppbv/day ¹	ppbv/day ²
2003	13	106	- 6.87	- 4.48
2004	8	106	- 4.59	+ 1.86
2005	20	92	-26.05	-23.19
2006	14	51	+11.10	+14.23
2007	17	119	-20.09	-15.01
2008	7	96	-11.26	-13.57
2009	26	46	-44.88	-35.57

¹ calculated from the studied period, ² linear fit from dashed line of Fig. 6.6d

also occurred in 2006 but it affected the lower stratosphere not as strongly as in 2009. Significant chemical ozone losses over the Arctic region were found in 2005, 2007, 2008 and 2003 with the years being listed in decreasing order in terms of ozone losses.

The chemical ozone losses were also computed at different isentropic levels (450 K - 600 K, in 25 K steps) using the vortex average method. The ozone depletions in mixing ratio versus time and isentropic levels for the Arctic are presented as contour plots Fig 6.7. The individual start day of each season is listed in Table 6.1.

The substantial ozone losses in the 2005 and 2007 Arctic winter stratospheres are obvious in Fig. 6.7. According to the panels of this figure, the peak ozone loss is > 1.4 ppmv in March of both years in the lower stratosphere between the 450 K and 525 K isentropic levels. The ozone depletion at these levels involves chlorine chemistry in the polar vortex (e.g., Solomon, 1999; Dufour et al., 2006), with chlorine being released from both of the reservoir gases, HCl and ClONO₂. When the sun reappears in spring the catalytic ozone destruction chains begin as explained in the section 2.1. From the peak of maximum ozone depletion upwards the ozone losses gradually decrease with increasing isentropic level. Then the ozone depletion increases again towards the 575 K – 600 K isentropic level as can be seen at end of the studied period in every year. The ozone loss above the 550 K isentropic level can be attributed to catalytic ozone destruction due to NO_x that has been reported in several earlier studies (Groß et al., 2005; Groß and Müller, 2007; Konopka et al., 2007). Konopka et al. (2007) suggested that the substantial ozone loss in the upper part of the polar vortex is caused by the horizontal transport of the NO_x from the subtropics rather than the descent of NO_x-rich air masses from the mesosphere.

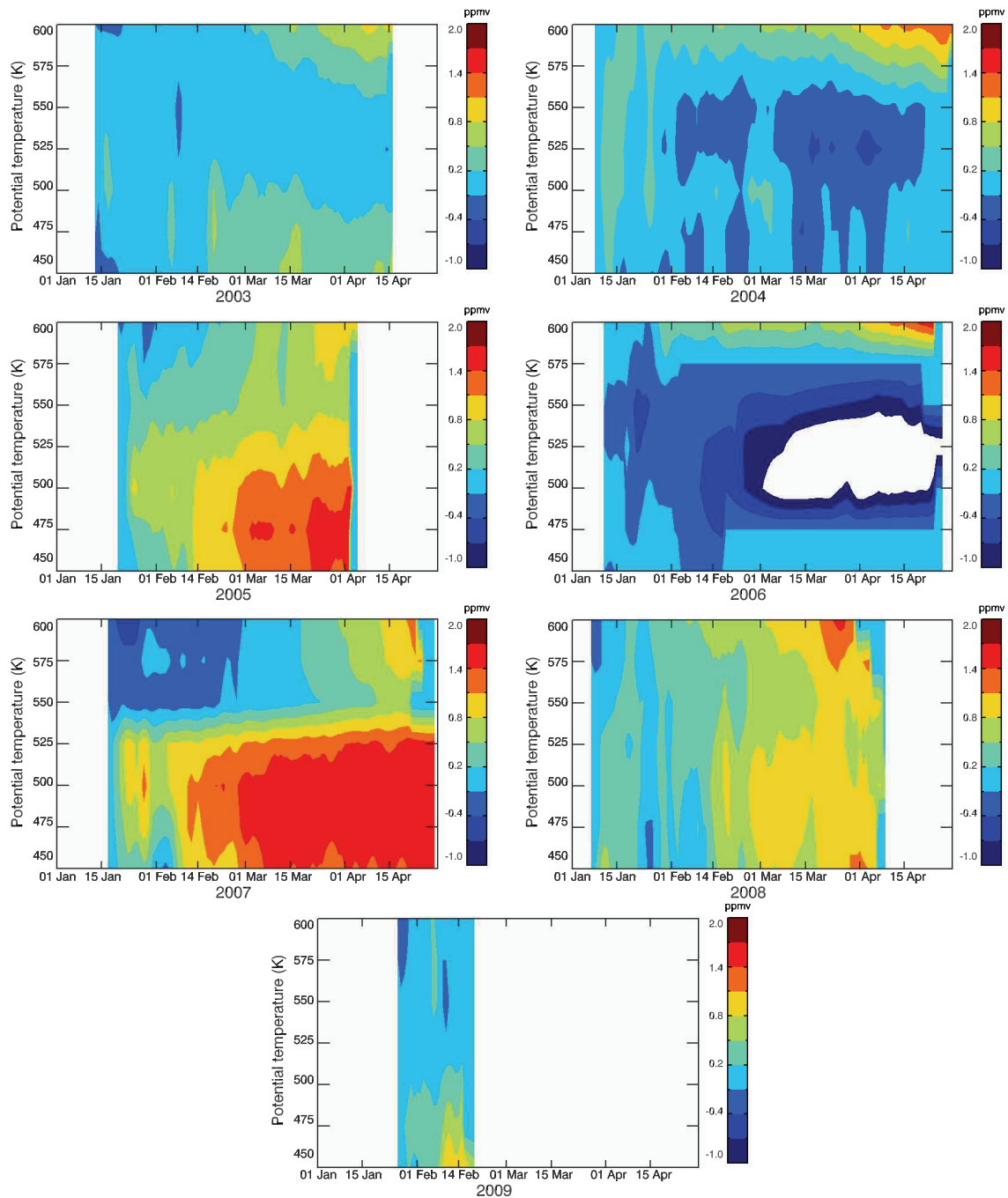


FIGURE 6.7: The vortex average ozone loss versus time and potential temperature between the 450 K and 600 K isentropic levels in the Arctic stratosphere derived from SCIAMACHY limb observations for the years 2003-2009.

Indications for significant ozone depletion cannot be detected in 2003/2004 and 2005/2006 polar vortices in the northern hemisphere. The data gap in 2006 between the 500 K and 550 K isentropic levels starting in early March is due to the fact that no SCIAMACHY observations are available inside the polar vortex defined by the MPV criterion introduced in section 6.2.

6.3.2 Antarctic chemical ozone loss

The results for the Antarctic polar vortex are presented in Fig. 6.8 in a similar way as the results for the Arctic vortex shown in Fig. 6.6. Because the overall polar vortex situation is stable in the southern hemisphere, the accumulated ozone loss is computed over the same period between August, 15 and November, 15 of every year.

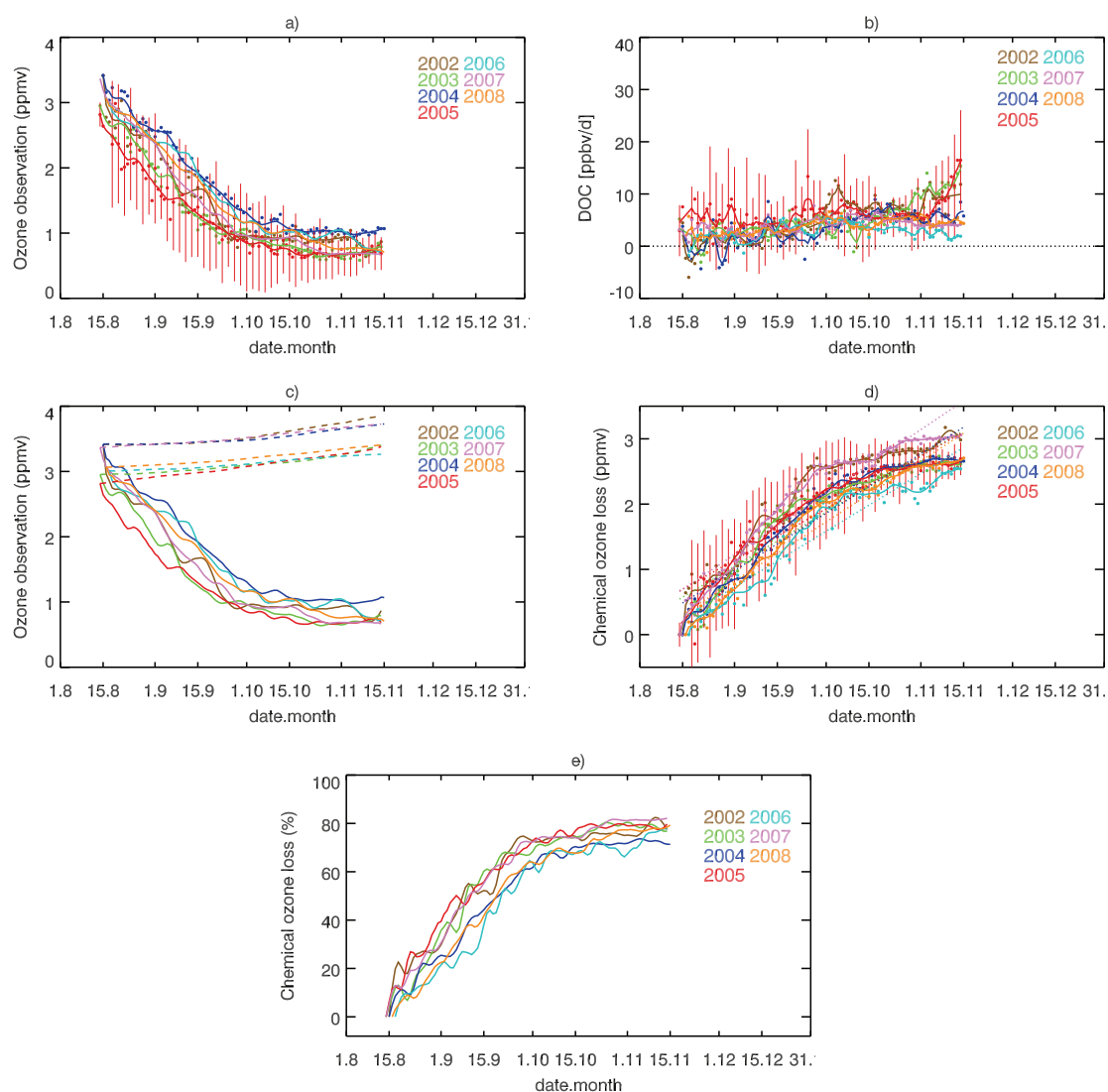


FIGURE 6.8: Panel a): observed changes in ozone mixing ratio, panel b): daily change in ozone mixing ratio due to diabatic descent determined with MIRAD model simulations, panel c): accumulated ozone mixing ratio from daily diabatic descent (dashed line) and the observed ozone mixing ratio (solid line), panel d): chemical ozone loss in ppmv (solid line) and the linear fit to the chemical ozone loss (dashed line), and panel e): chemical ozone loss in percent from SCIAMACHY observation at the 475 K isentropic level in the Antarctic stratosphere in 2002 – 2008 during winter – spring.

Fig. 6.8a shows the averaged ozone mixing ratio inside the Antarctic vortex at the 475 K potential temperature level. The diabatic daily ozone change (DOC) rates in the Antarctic stratosphere are shown in panel b of Fig. 6.8. The diabatic ozone descent in the Antarctic polar vortex is similar in all years during the studied period. Panel d of Fig. 6.8 shows that the ozone loss rates are larger in August and September than in October, when a stagnation in the chemical ozone loss is observed. The seasonally averaged daily chemical ozone loss rates inside the Antarctic polar vortex are summarized in Table 6.2.

TABLE 6.2: The chemical ozone loss rate over Antarctica between 15 August and 15 November in 2002–2008 at the 475 K isentropic level.

Year	Chemical O ₃ loss	
	ppbv/day ³	ppbv/day ⁴
2002	- 32.43	- 28.96
2003	- 28.08	- 27.74
2004	- 28.60	- 29.28
2005	- 28.97	- 26.16
2006	- 28.21	- 28.50
2007	- 32.89	- 31.40
2008	- 29.40	- 30.02

³ calculated from the studied period,

⁴ linear fit from dashed line of Fig. 6.8d

The chemical ozone loss during the 3–month period from August 15 to November 15 reaches 2 - 3 ppmv or 28 - 33 ppmv/day (averaged over the 3-month period) every year as shown in panel d of Fig. 6.8 and Table 6.2, respectively. The relative ozone losses are shown in Fig. 6.8e and amount to about 70 - 80% at the 475 K level by the end of October, and relative to August 15. The ozone loss rates for 2002 to 2008 show little inter–annual variability and are between 26 and 32 ppbv per day. The calculated average ozone loss rate maximizes at about 32 ppbv per day in 2007.

It is worthy to be noted here that the southern spring 2002 was characterized by a very unusual phenomenon, i.e., the first observed mid–winter major stratospheric warming in the southern hemisphere (e.g., Hoppel et al., 2003; Konopka et al., 2005; Manney et al., 2005b; Ricaud et al., 2005; von Savigny et al., 2005b). This early spring warming resulted from anomalously strong dynamical wave activity in the southern hemisphere which caused the splitting of the polar vortex into two parts associated with a splitting of the ozone hole. The overall size of the ozone hole in late September 2002 was only about 10% of its usual value (Stolarski et al., 2005). However, the ozone loss inside

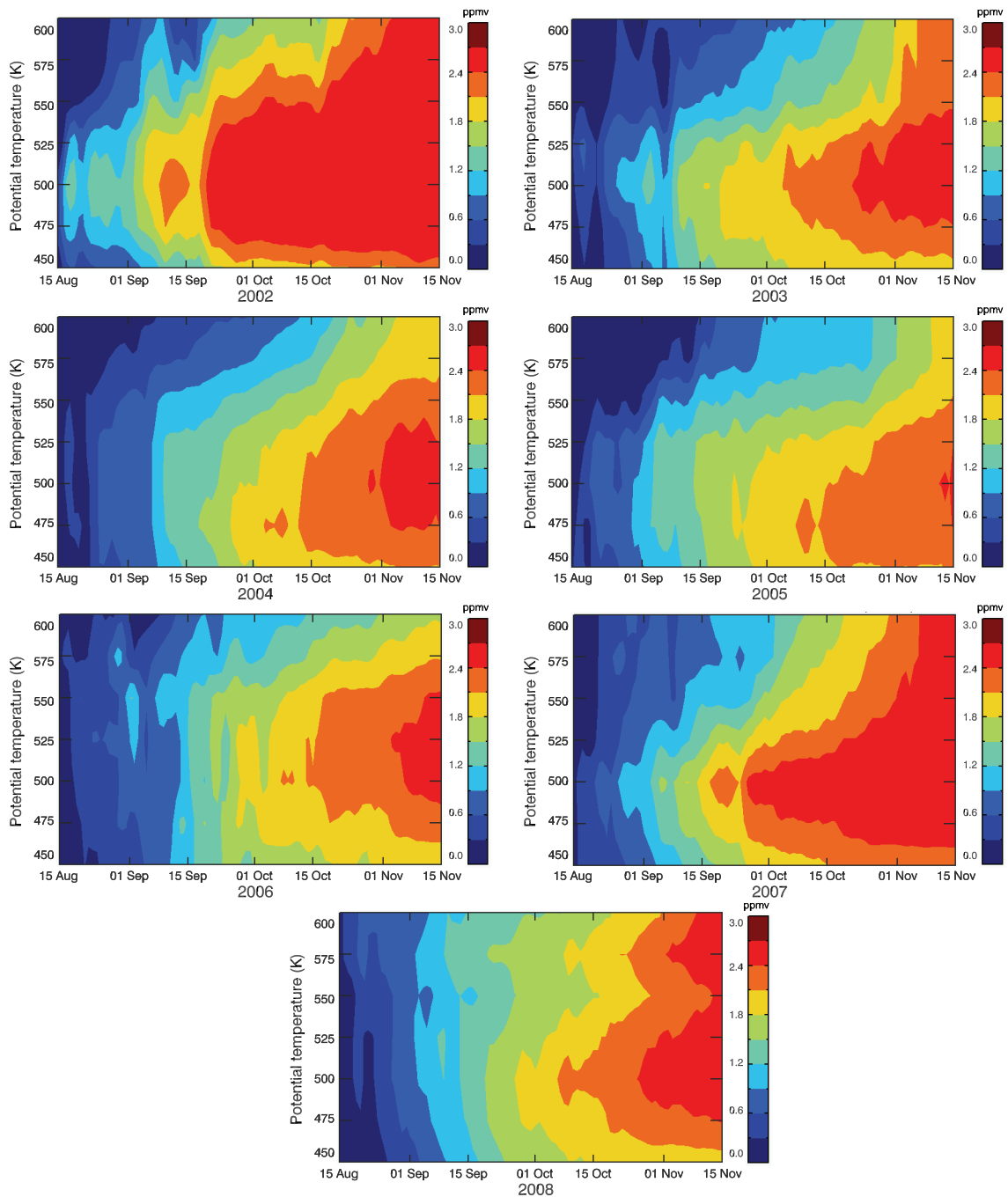


FIGURE 6.9: The vortex average ozone loss versus time and potential temperature between the 450 K and 600 K isentropic levels in the Antarctic stratosphere derived from SCIAMACHY limb observations between 15 August and 15 November 2002–2008.

the polar vortex in 2002, as presented in Fig. 6.8, is essentially the same as in all other years considered. This result differs somewhat from the study of Hoppel et al. (2003), who found the ozone loss in the Antarctic vortex about 20% smaller than for the other years analyzed (1994 - 2001).

Another noteworthy result of the present analysis is the fact, that the relative ozone losses between 450 K and 500 K do not exceed 80%, while many other studies report ozone losses of more than 90% at these levels (e.g., [Hoppel et al. \(2003\)](#)). This apparent discrepancy can be attributed to the more limited vertical resolution of the SCIAMACHY ozone profiles of about 4.5 km (given by the FWHM (Full Width at Half Maximum) of the averaging kernels).

Fig. 6.9 presents contour plots of the Antarctic ozone loss as a function of time and potential temperature - similar to Fig. 6.7 for the northern hemisphere - for the period August 15 to November 15 of each year. Obviously the Antarctic polar vortex is affected by more severe chemical ozone loss compared to the Arctic vortex and is characterized by a rather small inter-annual variability in chemical ozone loss. As depicted in Fig. 6.9, the maximum absolute ozone loss in terms of mixing ratio occurs near the 500 K isentropic level, but the entire potential temperature range studied is affected by substantial ozone losses, particularly towards the end of the period considered.

6.4 The correlation of chemical ozone loss and polar stratospheric clouds as observed from SCIAMACHY limb measurements

The ozone depletion in the polar winter stratosphere is caused by heterogenous chemistry on polar stratospheric clouds (PSCs) that activate large amounts of chlorine to catalytically destroy ozone inside the winter polar vortex ([Solomon, 1999](#)). A high correlation between PSC volume integrated over the winter and the amount of the chemical loss of column ozone (at 380 – 550K) in the Arctic polar vortex has been found by [Rex et al. \(2006, 2004\)](#). This phenomenon is also observed in this work in terms of PSC occurrence rate and the chemical ozone loss inside the polar vortex. The occurrence rate of PSCs is calculated as the ratio of the number of PSC detections and the total number of measurements in a given latitude and longitude bin of 5 and 10 degree, respectively, employing two weakly absorbing wavelengths in the near IR (750 nm and 1090 nm). More detail on the PSC detection technique can be found in [von Savigny et al. \(2005c\)](#). The occurrence rate maps of PSCs over the Arctic region retrieved from the SCIAMACHY limb measurements in January and February of 2003–2009 are shown in Fig. 6.10. From all panels in this figure, it can be seen that most of the PSCs form above 45°N and PSCs are detected in January more than in February.

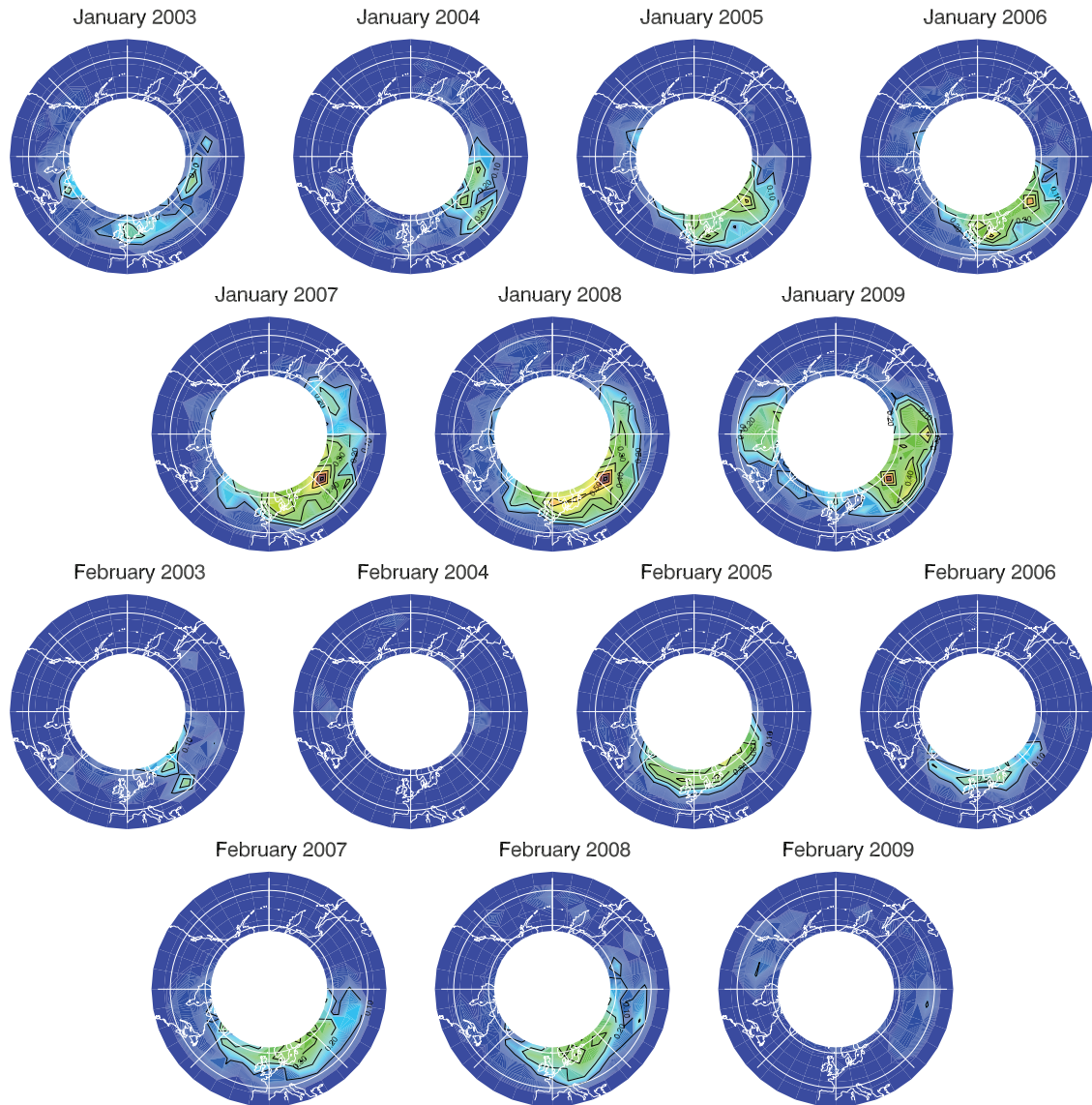


FIGURE 6.10: Polar maps of PSC occurrence rate in the northern hemisphere during January and February 2003–2009 from SCIAMACHY limb measurements.

The monthly averaged of PSC occurrence rates are shown in Fig. 6.11 – presented using the red–rightside scale. The averaged PSC occurrence rates in January and February for the northern hemisphere and the 40° – 65° latitude range are represented by the red lines with triangle and square, respectively, in panel a of Fig. 6.11. As can be noticed from Fig. 6.11a the PSC occurrences in the cold winters, i.e., 2003 and 2005 are quite similar in January and February. Larger changes in the PSC occurrence rates from January to February occurred in the warm winter years, e.g., 2004, 2009 which are characterized by SSWs events.

Panel a of Fig. 6.11 also shows the variation of the chemical ozone loss at the 475 K isentropic level over the Arctic region as the black line with circles. The filled–black

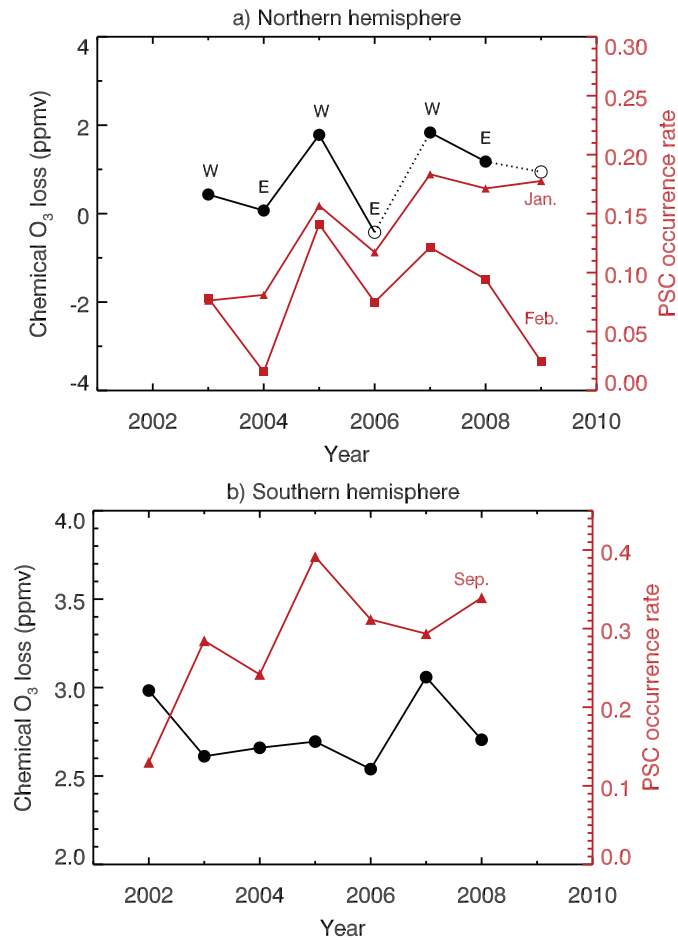


FIGURE 6.11: Panel a) The variation of PSC occurrence rate and chemical ozone loss from SCIAMACHY limb measurements. The red lines show the averaged PSC occurrence rates in the northern hemisphere in January (triangle) and on February (square) for the 40° – 65° latitude range. The chemical ozone losses from the start day (see Table 6.1) until April, 1 are shown as the black line with black-filled circles and until the last day when the polar vortex observed are shown as the black-open circle. Panel b) The red line with triangles shows the averaged PSC occurrence rates in the southern hemisphere during September for the 40° – 75° latitude range and the chemical ozone loss between August, 15 and November, 15 is shown as the black line with circles.

circle symbols show the chemical ozone loss from the individual start days as listed in Table 6.1 until April, 1. The open black circle symbols indicate the chemical ozone losses which are calculated only in the short period – start and end day as listed in Table 6.1 – due to lack of polar vortex information at the end of polar vortex season, i.e., 2006 and 2009. The letters E and W indicate the easterly/westerly phase of the QBO (quasi-biannual oscillation) (e.g., Baldwin et al. (2001)). This depiction now suggests a clear dependence of the relative magnitude of both the chemical ozone loss and the PSC occurrence rate on the phase of the QBO. The QBO westerly phase appears to be associated with large PSC occurrence and ozone losses, and the easterly phase with

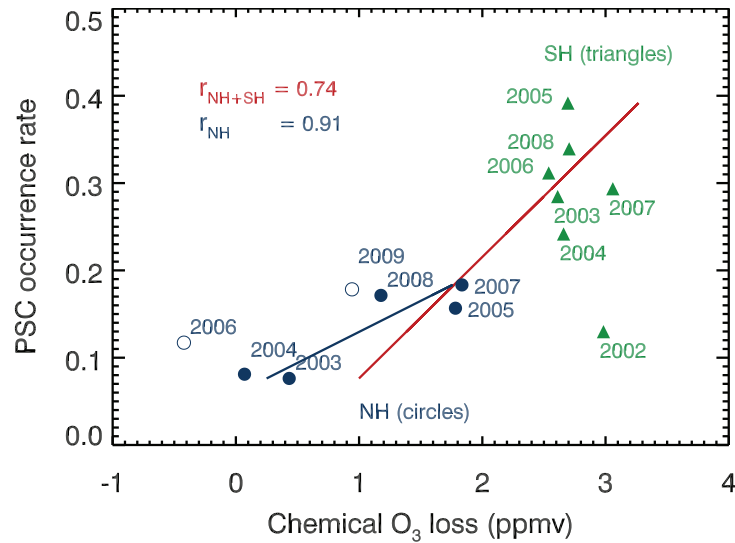


FIGURE 6.12: Scatter plot of PSC occurrence rate and chemical ozone loss from SCIAMACHY limb measurements. The circles show the PSC occurrence rate in the northern hemisphere in January and the triangles show the PSC occurrence rate in the southern hemisphere in September. The linear fit of PSC occurrence rate and chemical ozone loss is shown in the blue line for the northern hemisphere and the red line for both hemispheres.

lower PSC occurrence rates. This is consistent with the Holton–Tan mechanism (Holton and Tan, 1980) that related the westerly phase of the QBO with a more stable Arctic and colder vortex, subsequently leading to higher PSC occurrence and larger chemical ozone destruction.

The chemical ozone loss rates and the PSC occurrence rates in January for the Arctic region are replotted in Fig. 6.12 and the linear fit is shown as the blue line. Note, that years plotted as open circles (2006 and 2009 in northern hemisphere) are not taken into account for the correlation calculation. The PSC occurrence rate and chemical ozone loss in the northern hemisphere shows a very good correlation of 0.91. This result strongly supports the assumption of heterogeneous processes on the PSC surface leading catalytically ozone chemistry in northern hemisphere, and is in line with earlier studies (Rex et al., 2004; Rex et al., 2006).

PSCs in the southern hemisphere are also detected using SCIAMACHY limb measurements and are shown in Fig. 6.13 for the months of August and September. The occurrence of PSCs appears to be quite stable in these two months with the exception of 2002, when a major occurred after September 22 (e.g. von Savigny et al. (2005b)). The averaged PSC occurrence rates for September are shown as the red line in panel b of Fig. 6.11. The PSC occurrence rate in the southern hemisphere is higher than in the northern hemisphere for every winter season. Only considering the Antarctic polar

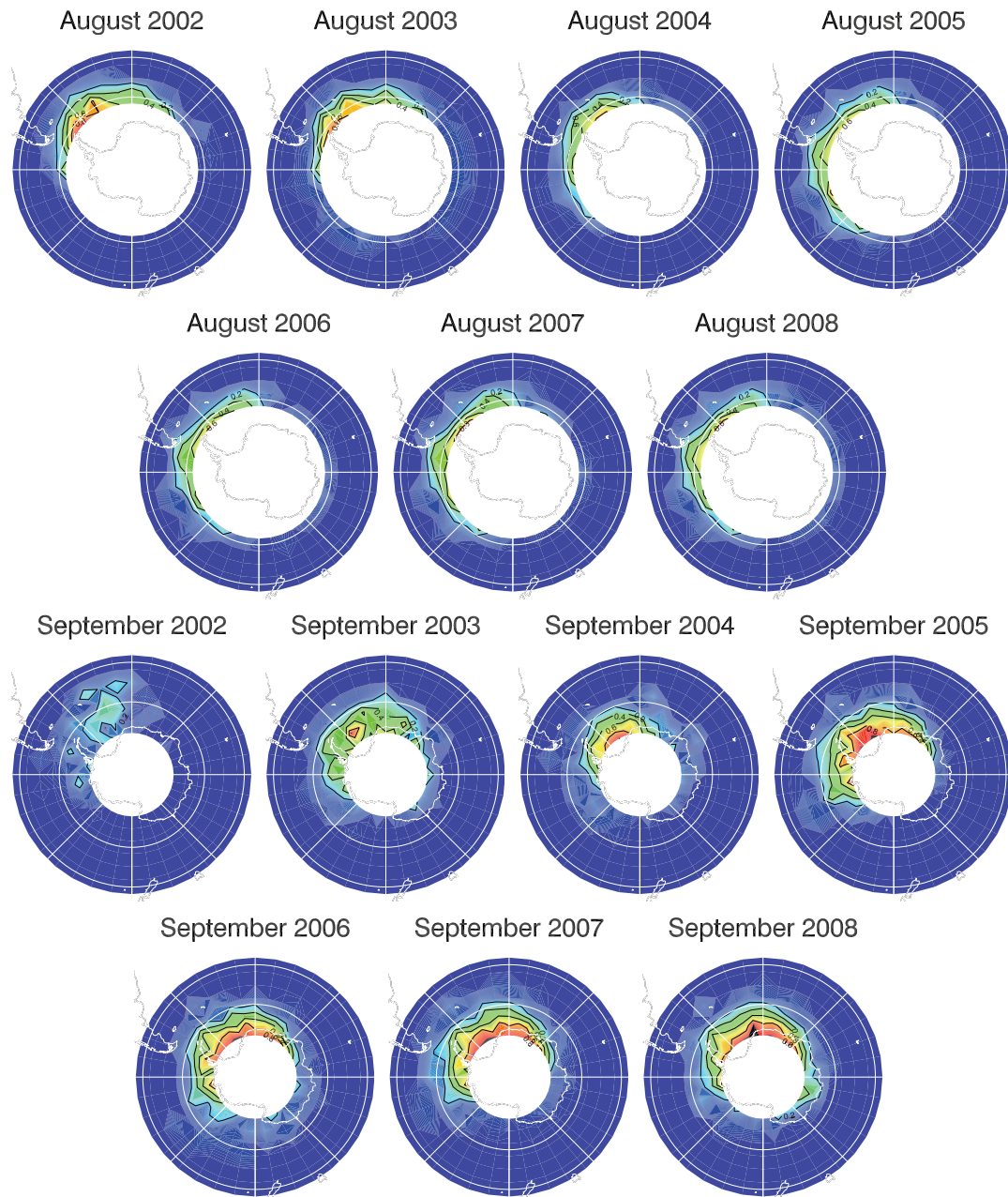


FIGURE 6.13: Polar maps of PSC occurrence rate in the southern hemisphere during August and September 2002–2008 from SCIAMACHY limb measurements.

winters, there is no strong correlation between chemical ozone loss and PSC occurrence rate. This is because of the low variability of PSC present in the southern hemisphere and because chemical ozone loss is determined from the ozone loss averaged inside the polar vortex region. However, PSC occurrence rate and chemical ozone loss, considering the polar winters in both hemispheres are found to be correlated with a coefficient of 0.74 as shown in Fig. 6.12.

6.5 Comparison of the chemical ozone loss from SCIAMACHY limb measurements to other instruments and techniques

The chemical ozone loss estimated from SCIAMACHY limb measurements using the vortex average method in the Arctic stratosphere 2004/2005 is selected for a comparison with other data sources and techniques. This year was chosen, because it was characterized by an unusually large catalytic ozone loss, as documented in numerous studies (e.g., Singleton et al., 2005; Dufour et al., 2006; Rex et al., 2006; Grooß and Müller, 2007; Singleton et al., 2007; Rösevall et al., 2008) and also in Fig. 6.8. Based on data from Rex et al. (2006), the vertical chemical ozone loss in terms of mixing ratio versus potential temperature over the time period from 5 January to 25 March 2005 is presented in Fig. 6.14. The red solid circles show the corresponding ozone loss rates derived from SCIAMACHY observations using the vortex average technique. Note that, no SCIAMACHY data below the 425 K isentropic level are presented here, because SCIAMACHY did not sample the vortex below the 425 K level during the first half of January, according to the vortex criterion employed here. The error bars represent the 1σ statistical uncertainties. The light-green, black, orange lines are based on POAM II/III, SAGE III and ozonesonde data, respectively. The dark-blue line is from Rex et al. (2006) and based on the Match method. The light-blue line was simulated with the Chemical Lagrangian Model of the Stratosphere (CLaMS) and is based on the work of Grooß and Müller (2007).

Fig. 6.14 shows that the vertical variation of the chemical ozone loss derived from SCIAMACHY is in quite good agreement with the other data sources and methods. The exception are model results from the CLaMS model which show lower ozone losses in the lower stratosphere below the 450 K isentropic level. Grooß et al. (2008) have quantified - using CLaMS model simulations for the Arctic winter 2002/2003 - the impact of transport across the vortex edge on ozone loss estimates using the Match method. They showed that the vortex average ozone loss rates, as determined using the Match technique are larger than the polar vortex average ozone loss in CLaMS below the 450 K isentropic level. Their result is consistent with the comparison here. Therefore, one of the reasons for the discrepancy between CLaMS and the other results may be across-vortex transport, as the transport across the vortex edge is ignored in the other techniques, including the vortex average technique applied to the SCIAMACHY data in this study.

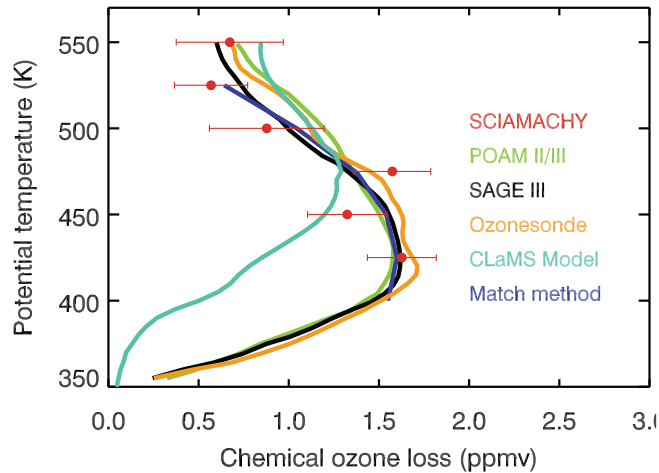


FIGURE 6.14: The chemical ozone loss over the time period from 5 January to 25 March 2005, estimated using various data sources and techniques. The data from the other instruments and methods are taken from [Rex et al. \(2006\)](#) and references therein.

[Singleton et al. \(2007\)](#) used the passive subtraction technique to quantify the daily chemical ozone loss using the SLIMCAT model and observed ozone from the POAM III, SAGE III, EOS MLS, ACE-FTS, and MAESTRO instruments by averaging over the measurement locations inside the vortex mostly during December 2004 to March 2005 over Arctic stratosphere, as shown in the top panel of Fig. 6.15. All instruments provided results, with a maximum inferred loss of 2–2.3 ppmv at the 450–475 K isentropic level. This is in good agreement with the losses estimated in the present study (see panel d of Fig. 6.6). [Groß and Müller \(2007\)](#) used the CLaMS model by applying the vortex average method to estimate the chemical ozone loss in the same year at latitude $> 65^\circ\text{N}$, as shown in the bottom panel of Fig. 6.15. The ozone loss results shown in Fig. 6.15 exhibit a similar pattern compared to the ozone losses derived from SCIAMACHY limb observations using the vortex average method shown in Fig. 6.7. That is the major ozone loss illustrated in the lower stratosphere at about the 450K–500 K isentropic levels. In addition, there is good correspondence of the chemical ozone loss feature at the high isentropic levels in Fig. 6.7 ($\sim 575\text{--}600$ K at the end of studied period) with the CLaMS results presented by [Groß and Müller \(2007\)](#) (see bottom panel of Fig. 6.15). However, this feature - attributed to NO_x driven catalytic ozone loss - does not appear in the multi-instrument analysis of [Singleton et al. \(2007\)](#) (see the top panel of Fig. 6.15).

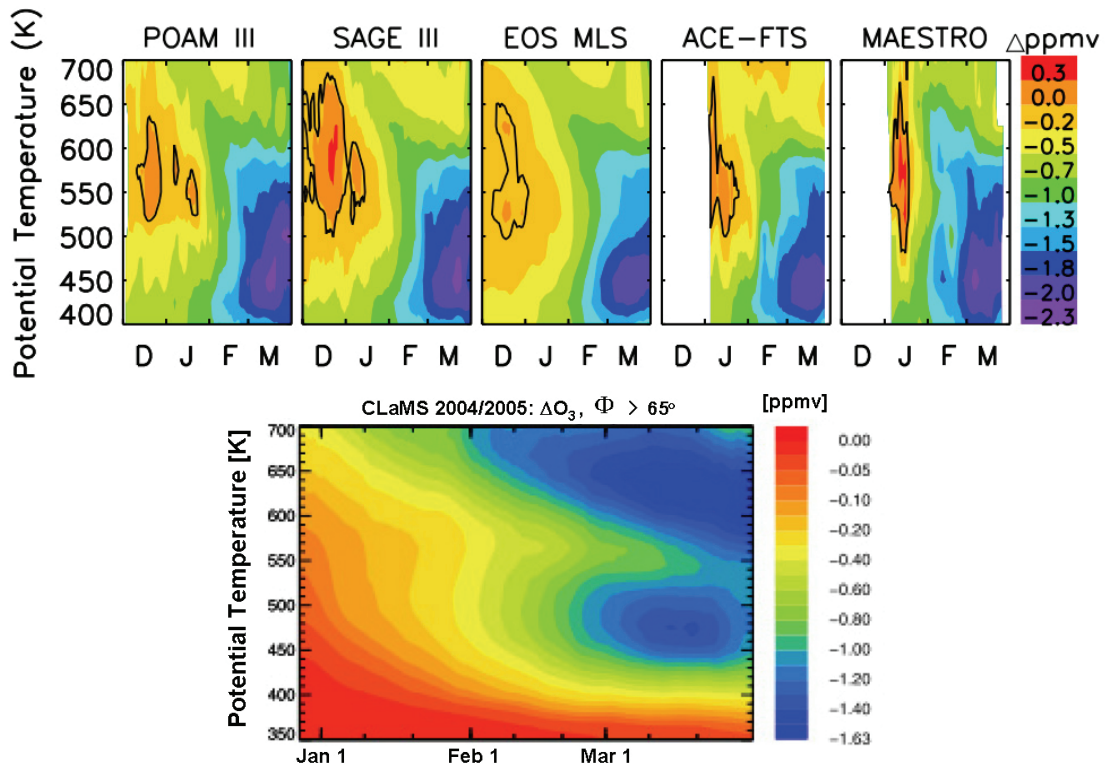


FIGURE 6.15: Chemical ozone loss in the Arctic stratosphere during spring/winter 2004-2005 from the other works. Top panel: Using the passive subtraction technique, differences were determined between passive ozone calculated by the SLIMCAT CTM and ozone measured by the POAM III, SAGE III, EOS MLS, ACE-FTS, and MAESTRO instruments (taken from Singleton et al. (2007)). Bottom panel: Using the vortex average method, the simulated ozone loss at latitude $> 65^\circ\text{N}$ from the CLaMS model is shown (taken from Groöß and Müller (2007)).

6.6 Concluding remarks on the chemical ozone loss inside the polar vortex

In this chapter, the polar vortex average technique was used for estimating ozone loss due to catalytic ozone destruction in the stratospheric vortex. Based on the SCIAMACHY limb observations 2002 – 2009, the estimation was made over the Arctic and Antarctic regions. The vortex boundaries at high latitudes were determined using a PV criterion and ozone inside the vortex was daily averaged. The deduced polar ozone losses showed distinct interhemispheric differences. From year to year, the high instability of the polar vortex was observed over the Arctic stratosphere during winter-spring. In contrast, relatively similar ozone losses were observed in the southern hemisphere polar spring where the dynamical conditions are more stable than in the northern

hemisphere. The stability of the polar vortex leads to strong radiative cooling that resulted in strong ozone descent across certain isentropic levels, even in the anomalous year 2002 characterized by the unusually early major stratospheric warming causing the well-documented vortex-split.

Large ozone losses in the Arctic stratosphere are only found in the cold winters 2004/2005 and 2006/2007 corresponding to PSC occurrence. The longest depletion period occurred in the 2006/2007 winter. The highest seasonally averaged depletion rate at the 475 K isentropic level occurred in the 2004/2005 winter, i.e., more than 20 ppbv per day, corresponding to a total relative ozone loss of about 40% during the studied period. Significant depletions around 1.4–2 ppmv were detected in the lower stratosphere between 450 K and 525 K isentropic levels in March of both years. Much lower ozone losses were determined for the warm winters 2003/2004 and 2005/2006.

Large ozone losses inside the polar vortex were found in the Antarctic stratosphere every year with similar seasonally averaged ozone loss rates of about 28–30 ppbv per day. The daily loss rates at the 475 K isentropic level were large from August to early October, and then decreased slowly until mid-November. By that time a total relative ozone loss averaged of about 80% or 2–2.5 ppmv inside the polar vortex occurred regularly each season. We note, that due to the limited vertical resolution of the SCIAMACHY ozone profile data product of about 4.5 km, the actual chemical ozone loss at the 475 K isentropic levels may be larger. The larger ozone losses observed in the Antarctic stratosphere are consistent with low temperatures dominating the polar vortex over a longer period and with higher stability as compared to the Arctic stratosphere. Over the Arctic region, the polar vortex is dynamically disturbed which leads to high temperatures and heat exchange and eventually to a break-up of the vortex. This is due to the asymmetrical distribution of topography and land-sea thermal contrast which are more pronounced in the northern hemisphere than in the southern hemisphere.

The PSC occurrence rates have been also determined in this work. We found that the PSC occurrence corresponds to the chemical ozone loss in the northern hemisphere and overall in both hemispheres. The correlation in the southern hemisphere is not so good due to the low interannual variability of vortex stability, PSC occurrence and catalytic ozone losses.

The vertical variation of the chemical ozone loss, which was determined from SCIAMACHY limb observations using the vortex averaged method, showed good agreement with the results of other instruments and techniques. In comparison to the CLaMS

model simulations, only at the lower stratosphere discrepancies appeared, with the CLaMS loss being smaller than the loss derived from SCIAMACHY observations. This discrepancy is most likely caused by the fact that across-vortex transport is neglected in the vortex average technique applied to the SCIAMACHY data.

Chapter 7

Summary and Outlook

This thesis has presented a technique to retrieve ozone profiles from satellite observations of scattered solar radiation in limb viewing geometry. This technique combines the Chappuis and Hartley band information to infer ozone profiles in the altitude range from the lower stratosphere to the middle mesosphere (15 – 65 km altitude). The ozone profile retrievals from SCIAMACHY limb measurements using this technique, which is called stratozone version 2.0, show good agreement with independent measurements. In this work, two aspects related to ozone profile retrievals using this combined Chappuis and Hartley bands approach are focused on.

The first focus is a comprehensive sensitivity study of ozone retrievals from limb-scattered radiance measurements to tropospheric clouds using the SCIATRAN radiative transfer model. The results show that cloud sensitivity of the limb ozone retrievals is significant in the Chappuis bands at lower stratospheric altitudes. The relative error in the retrieved ozone concentrations gradually decreases with increasing altitude and becomes negligible above about 40 km. The parameters with the largest impact on the ozone retrievals are cloud optical thickness, ground albedo and solar zenith angle. Clouds with different geometrical thicknesses or different cloud altitudes have a similar impact on the ozone retrievals for a given cloud optical thickness value, if the clouds are outside the field of view of the instrument. The effective radius of water droplets has a small influence on the error, i.e., less than 0.5% at altitudes above the cloud top height. Furthermore, the impact of clouds on the ozone profile retrievals was found to have a rather small dependence on the solar azimuth angle (less than 1% for all possible azimuth angles). For the most frequent cloud types, occurring in the terrestrial atmosphere, the total error is below 6% above 15 km altitude, if clouds are completely neglected in

the retrieval. Neglecting clouds in the ozone profile retrievals generally leads to a low bias for a low ground albedo and to a high bias for a high ground albedo, assuming that the ground albedo is well known. Future versions of the SCIAMACHY ozone profile retrieval processor operated at the University of Bremen will limit the tangent height range employed in the retrieval to tangent heights above cloud top height. As discussed in section 5.6.1, this leads to a significant reduction of the effect of clouds on the ozone retrievals in the lower stratosphere. Tropospheric clouds are also detected (and cloud top heights determined) from the SCIAMACHY limb measurements themselves, and this cloud data base will be used for the future ozone profile retrievals.

The second focus of this work deals with the quantification of the chemical ozone loss in the polar winter/spring stratosphere between the 475 K– 600 K isentropic levels. In this study, the vortex average method is applied to study the chemical ozone loss from SCIAMACHY limb measurements in 2002–2009 in the Arctic and Antarctic stratospheres. Descending ozone due to dynamic effects is taken into account in this method to determine the amount of ozone destroyed chemically in catalytic cycles. The results show that relative ozone losses occurred inside the polar vortices of up to about 40% in cold Arctic winters and about 80% in every year for the Antarctic stratosphere. The comparison of the vertical variation of the chemical ozone loss from SCIAMACHY limb measurements using the vortex average method with results from other instruments and techniques showed good agreement. An exception is the comparison with the CLaMS model showing lower ozone loss in the lowermost stratosphere. One of the reasons for this discrepancy may be that the horizontal ozone transport across the vortex edge is neglected in this work. It will be a future task to quantify the transport across the vortex edge.

Futhermore, the ozone profile retrieval from SCIAMACHY limb–scatter observations should be improved in the future by:

- a) simultaneously retrieving an effective surface albedo (including distribution effects of both the generally unknown surface albedo and tropospheric cloud cover)
- b) performing a retrieval of stratospheric aerosol extinction profiles prior to retrieving ozone profiles. Uncertainties in the knowledge of the actual stratospheric background aerosol loading and the microphysical characteristics of stratospheric aerosols is one of the most important error sources of ozone profile retrievals from limb–scatter observations.

Appendix A

Relationship between the Chappuis triplet and the limb radiance profile in the center of the Chappuis band

In this Appendix, we demonstrate that for the typical atmospheric/observation conditions the Chappuis triplet as a function of any cloud parameter has a similar behavior as the reflected nadir solar radiation. This means that, for example, an increase in the reflected radiance due to a variation of any cloud parameter leads to an increase in the Chappuis triplet value as well. To demonstrate this let us represent the limb radiance at the wavelength λ_k and tangent height h_i as a sum of the single scattered and the diffuse radiance:

$$I(\lambda_k, h_i) = I_s(\lambda_k, h_i) + I_d(\lambda_k, h_i) . \quad (\text{A.1})$$

Using this representation, Eq. (4.23) for the normalized limb radiance is rewritten as

$$I_N(\lambda_k, h_i) = \frac{I_s(\lambda_k, h_i) + I_d(\lambda_k, h_i)}{I_s(\lambda_k, h_r) + I_d(\lambda_k, h_r)} , \quad (\text{A.2})$$

where h_r is the reference tangent height, and the Chappuis triplet defined by Eq. (4.24) is obtained as

$$y(h_i) = \frac{I_N(\lambda_2, h_i)}{\sqrt{I_N(\lambda_1, h_i)I_N(\lambda_3, h_i)}} . \quad (\text{A.3})$$

Here, the wavelengths λ_1 , λ_2 , and λ_3 are defined as discussed in Sec. 4.4. Since our consideration is only qualitative, we assume for a further discussion that the normalized radiances at wavelengths λ_1 and λ_3 are equal, i.e., $I_N(\lambda_1, h_i) = I_N(\lambda_3, h_i)$. This allows the mathematical formulas presented below to be substantially shortened. Under this assumption, Eq. (A.3) results in

$$y(h_i) = \frac{I_s(\lambda_1, h_r) + I_d(\lambda_1, h_r)}{I_s(\lambda_2, h_r) + I_d(\lambda_2, h_r)} \times \frac{I_s(\lambda_2, h_i) + I_d(\lambda_2, h_i)}{I_s(\lambda_1, h_i) + I_d(\lambda_1, h_i)}, \quad (\text{A.4})$$

For the discussion below, we restrict our considerations to clouds with top heights below the tangent height h_i . In this case, the single scattered limb radiation is independent of cloud parameters and the dependence of the normalized limb radiance and of the Chappuis triplet on cloudiness is only due to the diffuse radiation. Let us now simplify Eqs. (A.2) and (A.4) expanding these into Taylor series with respect to the diffuse radiation and restricting the consideration to the linear terms. In particular, the normalized limb radiance given by Eq. (A.2) is written as follows:

$$I_N[I(\lambda_k, h_i), I(\lambda_k, h_r)] = I_N[I_s(\lambda_k, h_i), I_s(\lambda_k, h_r)] + \left. \frac{\partial I_N}{\partial I_d(h_i)} \right|_{I_d=0} I_d(\lambda_k, h_i) + \left. \frac{\partial I_N}{\partial I_d(h_r)} \right|_{I_d=0} I_d(\lambda_k, h_r), \quad (\text{A.5})$$

where $\partial I_N/\partial I_d(h_i)$ and $\partial I_N/\partial I_d(h_r)$ are partial derivatives of the normalized limb radiance with respect to the diffuse radiance at the tangent height h_i and h_r , respectively.

After some algebra Eq. (A.2) can then be rewritten in the following form:

$$I_N(\lambda_k, h_i) = r_s^n \left\{ 1 + \left[\frac{I_d(\lambda_k, h_i)}{I_s(\lambda_k, h_i)} - \frac{I_d(\lambda_k, h_r)}{I_s(\lambda_k, h_r)} \right] \right\}, \quad (\text{A.6})$$

where $r_s^n = I_s(\lambda_k, h_i)/I_s(\lambda_k, h_r)$ is the normalized single scattered limb radiance, and Eq. (A.4) results in

$$y(h_i) = r_s^t \left\{ 1 + \left[\frac{I_d(\lambda_2, h_i)}{I_s(\lambda_2, h_i)} - \frac{I_d(\lambda_2, h_r)}{I_s(\lambda_2, h_r)} \right] - \left[\frac{I_d(\lambda_1, h_i)}{I_s(\lambda_1, h_i)} - \frac{I_d(\lambda_1, h_r)}{I_s(\lambda_1, h_r)} \right] \right\}, \quad (\text{A.7})$$

where $r_s^t = I_s(\lambda_2, h_i)I_s(\lambda_1, h_r)/I_s(\lambda_1, h_i)I_s(\lambda_2, h_r)$ is the Chappuis triplet value corresponding to the single scattered limb radiation. Both the single scattered and the

diffuse limb radiation at the tangent height h_i can be represented as follows:

$$I_{s,d}(\lambda_k, h_i) = \int_{l_1}^{l_2} \sigma_k(l) J_{s,d}(\lambda_k, l) T_k(l) dl, \quad (\text{A.8})$$

where the integration is carried out along the instrument line of sight, $\sigma_k(l)$ is the extinction coefficient at the wavelength λ_k , $T_k(l) = e^{-\tau_k(l_1, l)}$ is the transmission function along the line of sight between the points having coordinates of l_1 and l , where l_1 corresponds to the instrument location, $\tau_k(l_1, l)$ is the corresponding optical depth, and $J_{s,d}(\lambda_k, l)$ is the source function of the single scattered or the diffuse radiation given by

$$J_{s,d}(\lambda_k, l) = \frac{\omega_k(l)}{4\pi} \int_{4\pi} p_k(\Omega(l), \Omega) I_{s,d}(\lambda_k, l, \Omega) d\Omega. \quad (\text{A.9})$$

Here, $\omega_k(l)$ is the single scattering albedo at wavelength λ_k at the line of sight point with coordinate l , $p_k(\Omega(l), \Omega)$ is the phase function describing the scattering probability from all directions to the line of sight direction, $\Omega := \{\mu, \phi\}$ describes the set of variables $\mu \in [-1, 1]$ and $\phi \in [0, 2\pi]$ where μ is the cosine of the polar angle θ measured from the positive τ -axis and ϕ is the SAA, and $I_{s,d}(\lambda_k, l, \Omega)$ is the single scattered or diffuse radiation field at the line of sight point l . Assuming that only the tangent point region contributes to the integral along the line of sight, Eq. (A.8) can be simplified as follows:

$$I_{s,d}(\lambda_k, h_i) \approx \sigma_k(h_i) J_{s,d}(\lambda_k, h_i) T_k(h_i), \quad (\text{A.10})$$

where $T_k(h_i)$ is the transmission function along the line of sight from the the tangent height h_i to top of atmosphere. Using Eq. (A.10) the ratio of the diffuse to the single scattered radiation can be written as follows:

$$\frac{I_d(\lambda_k, h_i)}{I_s(\lambda_k, h_i)} \approx \frac{J_d(\lambda_k, h_i)}{J_s(\lambda_k, h_i)}. \quad (\text{A.11})$$

Substituting the ratio $I_d(\lambda_k, h_i)/I_s(\lambda_k, h_i)$ as given by Eq. (A.11) into Eqs. (A.6) and (A.7), we obtain

$$I_N(\lambda_k, h_i) = r_s^n \left\{ 1 + \left[\frac{J_d(\lambda_k, h_i)}{J_s(\lambda_k, h_i)} - \frac{J_d(\lambda_k, h_r)}{J_s(\lambda_k, h_r)} \right] \right\} \quad (\text{A.12})$$

and

$$y(h_i) = r_s^t \left\{ 1 + \left[\frac{J_d(\lambda_2, h_i)}{J_s(\lambda_2, h_i)} - \frac{J_d(\lambda_2, h_r)}{J_s(\lambda_2, h_r)} \right] - \left[\frac{J_d(\lambda_1, h_i)}{J_s(\lambda_1, h_i)} - \frac{J_d(\lambda_1, h_r)}{J_s(\lambda_1, h_r)} \right] \right\}. \quad (\text{A.13})$$

At the next step, let us formulate an approximate relationship between the diffuse source function, $J_d(\lambda_k, h_i)$, and the intensity of radiation reflected by a cloud. This is done using the approximate expression for the intensity of diffuse radiation suggested by [Kokhanovsky and Rozanov \(2004\)](#) which we write here in the following form:

$$R(\Omega) = R_s(\Omega) + T(\mu_0; H, h_c) R_c(\Omega) T(\mu; h_i, h_c), \quad (\text{A.14})$$

where $R_s(\Omega)$ is the intensity of radiation scattered in the atmosphere above the cloud calculated in the single scattering approximation, $R_c(\Omega)$ is the intensity of radiation scattered within the cloud and in the underlying atmosphere including the surface reflection (we neglect with the dependence of $R_c(\Omega)$ on the wavelength within the Chapuis ozone absorption band), μ_0 is a cosine of the SZA, $T(\mu_0; H, h_c) = e^{-\tau(H, h_c)/\mu_0}$ is the transmission between the top of the atmosphere (H) and the cloud top height (h_c), and $T(\mu; h_i, h_c) = e^{-\tau(h_i, h_c)/\mu}$ is the transmission between the cloud top height (h_c) and the tangent point (h_i). In the case of a weak gaseous absorption, the first term on the right-hand side of Eq. (A.14) is much smaller than the second term and, thus, it can be neglected. Substituting then Eq. (A.14) into Eq. (A.9) the following approximate expression for the diffuse source function can be obtained :

$$J_d(\lambda_k, h_i) \approx \frac{\omega_k(h_i)}{4\pi} \int_{4\pi} p_k(\Omega_i, \Omega) R_c(\Omega) T_k(\mu; h_i, h_c) d\Omega \times T_k(\mu_0; H, h_c). \quad (\text{A.15})$$

Taking into account that

$$I_s(\lambda_k, l, \Omega) = \pi \delta(\Omega - \Omega_0) T_k(\mu_0; H, h_i), \quad (\text{A.16})$$

where $\delta(\Omega - \Omega_0)$ is the Dirac delta function and the extraterrestrial solar flux is set to π , Eq. (A.9) for the single scattering source function becomes

$$J_s(\lambda_k, h_i) = \frac{\omega_k(h_i)}{4} p_k(\Omega_i, \Omega_0) T_k(\mu_0; H, h_i) \quad (\text{A.17})$$

and the ratio of the diffuse to the single scattering source function at the tangent height h_i can be written as follows:

$$\begin{aligned} \frac{J_d(\lambda_k, h_i)}{J_s(\lambda_k, h_i)} &= \frac{1}{\pi} \int_{4\pi} \tilde{p}_k(\Omega_i, \Omega) R_c(\Omega) T_k(\mu; h_i, h_c) d\Omega \\ &\times T_k(\mu_0; h_i, h_c) , \end{aligned} \quad (\text{A.18})$$

where $\tilde{p}_k(\Omega_i, \Omega) = p_k(\Omega_i, \Omega)/p_k(\Omega_i, \Omega_0)$, and $T_k(\mu_0; h_i, h_c) = T_k(\mu_0; H, h_c)/T_k(\mu_0; H, h_i)$ is the transmission between the tangent height h_i and the cloud top height altitude h_c . The ratio of the diffuse to the single scattering source function at the reference tangent height can be obtained setting in Eq. (A.18) $h_i = h_r$. To simplify Eq. (A.18) let us introduce the following abbreviation for the product of two transmission functions:

$$T_k(h_i, h_c) = T_k(\mu; h_i, h_c) T_k(\mu_0; h_i, h_c) . \quad (\text{A.19})$$

Now, Eq. (A.18) can be rewritten as follows:

$$\frac{J_d(\lambda_k, h_i)}{J_s(\lambda_k, h_i)} = \frac{1}{\pi} \int_{4\pi} \tilde{p}_k(\Omega_i, \Omega) R_c(\Omega) T_k(h_i, h_c) d\Omega . \quad (\text{A.20})$$

Introducing an auxiliary function $\mathcal{T}(\lambda_k)$ as

$$\mathcal{T}(\lambda_k) = \frac{J_d(\lambda_k, h_i)}{J_s(\lambda_k, h_i)} - \frac{J_d(\lambda_k, h_r)}{J_s(\lambda_k, h_r)} , \quad (\text{A.21})$$

Eqs. (A.12) and (A.13) can be rewritten as follows:

$$I_N(\lambda_k, h_i) = r_s^n [1 + \mathcal{T}(\lambda_k)] , \quad (\text{A.22})$$

$$y(h_i) = r_s^t [1 + \mathcal{T}(\lambda_2) - \mathcal{T}(\lambda_1)] . \quad (\text{A.23})$$

These equations along with Eqs. (A.20) and (A.21) provide a simple linear relationship between the normalized limb radiance $I_N(\lambda_k, h_i)$ or the Chappuis triplet value $y(h_i)$ on the one hand and the intensity of radiation reflected by a cloud $R_c(\Omega)$ on the other hand.

The goal of our study is to prove that if the intensity of reflected radiation increases due to an increase in a certain cloud parameter, for example τ , i.e.,

$$\frac{\partial R_c(\Omega)}{\partial \tau} = R'_c(\Omega) > 0 , \quad (\text{A.24})$$

then $\partial I_N(\lambda_k, h_i)/\partial \tau > 0$ and $\partial y(h_i)/\partial \tau > 0$ as well, i.e., both the normalized limb

radiance and the Chappuis triplet increase when the intensity of reflected radiation increases. The discussion below is applicable to nearly all cloud parameters except for the cloud top height. This is because, unlike other cloud parameters, the variation in the cloud top height affects not only the solar radiation reflected by cloud in Eq. (A.14) but also the transmissions $T(\mu_0; H, h_c)$ and $T(\mu; h_i, h_c)$ which must be differentiated as well when calculating the derivative of $R(\Omega)$. Since, as shown in Sec. 5.6.3, the dependence of the ozone vertical profile retrievals on cloud top height is rather small, we exclude this parameter from the consideration below for a sake of simplicity.

Differentiating Eqs. (A.22) and (A.23) with respect to the cloud parameter of interest, we obtain

$$I'_N(\lambda_k, h_i) = r_s^n [1 + \mathcal{J}'(\lambda_k)] , \quad (\text{A.25})$$

$$y'(h_i) = r_s^t [1 + \mathcal{J}'(\lambda_2) - \mathcal{J}'(\lambda_1)] . \quad (\text{A.26})$$

Here, taking into account Eqns. (A.20) and (A.21), the derivative $\mathcal{J}'(\lambda_k)$ is obtained as

$$\begin{aligned} \mathcal{J}'(\lambda_k) &= \frac{1}{\pi} \int_{4\pi} \tilde{p}_k(\Omega_i, \Omega_0) R'_c(\Omega) \\ &\times \left[T_k(h_i, h_c) - T_k(h_r, h_c) \right] d\Omega . \end{aligned} \quad (\text{A.27})$$

or

$$\begin{aligned} \mathcal{J}'(\lambda_k) &= \frac{1}{\pi} \int_{4\pi} \tilde{p}_k(\Omega_i, \Omega_0) R'_c(\Omega) T_k(h_i, h_c) \\ &\times \left[1 - T_k(h_r, h_i) \right] d\Omega , \end{aligned} \quad (\text{A.28})$$

where $T_k(h_r, h_i) = T_k(h_r, h_c)/T_k(h_i, h_c)$ is the transmission between the reference tangent height h_r and the tangent height h_i . Now it is obvious that

$$\mathcal{J}'(\lambda_k) > 0 , \text{ if } R'_c(\Omega) > 0 . \quad (\text{A.29})$$

Thus, we found that the derivative of the normalized limb radiance with respect to a cloud parameter has the same sign as the derivative of the intensity the solar radiation reflected by the cloud.

To complete our discussion, we show that the corresponding derivative of the Chappuis triplet has the same sign as well, i.e., we prove that $\mathcal{J}'(\lambda_2) - \mathcal{J}'(\lambda_1) > 0$. This can be

done taking into account that the ozone absorption at wavelength λ_2 is larger than at λ_1 . This allows us to rewrite Eq. (A.27) for λ_2 in the following form:

$$\begin{aligned} \mathcal{J}'(\lambda_2) &= \frac{1}{\pi} \int_{4\pi} \tilde{p}_2(\Omega_i, \Omega_0) R'_c(\Omega) \left[T_1(h_i, h_c) T_g(h_i, h_c) \right. \\ &\quad \left. - T_1(h_r, h_c) T_g(h_r, h_c) \right] d\Omega, \end{aligned} \quad (\text{A.30})$$

where $T_g(h_i, h_c)$ and $T_g(h_r, h_c)$ describe additional gaseous absorption at wavelength λ_2 as compared to wavelength λ_1 . Now, taking into account that $T_1(h_r, h_c) = T_1(h_r, h_i) T_1(h_i, h_c)$, the difference $\mathcal{J}'(\lambda_2) - \mathcal{J}'(\lambda_1)$ can be written as

$$\begin{aligned} \mathcal{J}'(\lambda_2) - \mathcal{J}'(\lambda_1) &= \frac{1}{\pi} \int_{4\pi} \tilde{p}_2(\Omega_i, \Omega_0) R'_c(\Omega) T_1(h_i, h_c) \\ &\quad \times \left\{ \left[T_g(h_i, h_c) - T_1(h_r, h_i) T_g(h_r, h_c) \right] \right. \\ &\quad \left. - \left[1 - T_1(h_r, h_i) \right] \right\} d\Omega. \end{aligned} \quad (\text{A.31})$$

As seen from this equation, in contrast to $\mathcal{J}'(\lambda_k)$, the difference $\mathcal{J}'(\lambda_2) - \mathcal{J}'(\lambda_1)$ can be both negative and positive. Indeed, assuming that the absorption between h_i and h_c can be neglected, i.e., $T_g(h_i, h_c) = 1$, the expression in brackets results in

$$\begin{aligned} \{ \} &= T_1(h_r, h_i) - T_1(h_r, h_i) T_g(h_r, h_c) \\ &= T_1(h_r, h_i) \left[1 - T_g(h_r, h_c) \right], \end{aligned} \quad (\text{A.32})$$

and $\mathcal{J}'(\lambda_2) - \mathcal{J}'(\lambda_1) > 0$. On the other hand, assuming that gaseous absorption is very strong, i.e., $T_g(h_i, h_c) = T_g(h_r, h_c) = 0$, we have

$$\{ \} = - \left[1 - T_1(h_r, h_i) \right], \quad (\text{A.33})$$

i.e., $\mathcal{J}'(\lambda_2) - \mathcal{J}'(\lambda_1) < 0$. Thus, generally, the sign of the difference $\mathcal{J}'(\lambda_2) - \mathcal{J}'(\lambda_1)$ depends on the gaseous absorption in the atmosphere. In the considered case of measurements of scattered solar light in the Chappuis absorption band of ozone, it is reasonable to assume that the gaseous absorption and atmospheric extinction between the tangent heights h_r and h_i is weak. Under this assumption, we have

$$T_1(h_r, h_i) \approx 1 - \tau_1(h_r, h_i), \quad (\text{A.34})$$

$$T_g(h_r, h_c) \approx 1 - \tau_g(h_r, h_c), \quad (\text{A.35})$$

where $\tau_1(h_r, h_i)$ and $\tau_g(h_r, h_c)$ are the optical thicknesses of the extinction (Rayleigh scattering and ozone absorption at λ_1) and of the gaseous absorption, respectively (we remind that we neglect the aerosol extinction and the gaseous absorption should be understood as additional absorption at wavelength λ_2 as compared to wavelength λ_1). Substituting now these approximations into Eq. (A.31) and neglecting the quadratic terms, i.e., $\tau_1(h_r, h_i) \tau_g(h_r, h_c)$, after simple algebra we obtain

$$\begin{aligned} \mathcal{J}'(\lambda_2) - \mathcal{J}'(\lambda_1) &= \frac{1}{\pi} \int_{4\pi} \tilde{p}_2(\Omega_i, \Omega_0) R'_c(\Omega) T_1(h_i, h_c) \\ &\times \tau_g(h_r, h_i) d\Omega . \end{aligned} \quad (\text{A.36})$$

Thus, we can state that the derivative of the triplet with respect to the cloud parameters has the same sign as the derivative of the intensity of solar radiation reflected by clouds if the difference in gaseous absorption between the wavelengths forming the triplet is small and the extinction of the radiation between tangent heights h_r and h_i due to the scattering processes is small as well. Although these assumptions commonly hold, in the case of very large ozone concentrations Eq. A.35 is not valid anymore and the signs of the derivatives can be different. Thus, the sensitivity of the triplet to clouds can not be explained considering the intensity of the reflected solar radiation in this case.

Appendix B

Abbreviations

Abbreviations	Meanings
ACE	Atmosphere Chemistry Experiment
ACE-FTS	Atmospheric Chemistry Experiment–Fourier Transform Spectrometer
CLaMS	Chemical Lagrangian Model of the Stratosphere
DOC	Diabatic daily Ozone Change
DU	Dobson Unit
Envisat	ENVironment SATellite
EOS	Earth Observing System
ERBS	Earth Radiation Budget Satellite
FM	Flight Model
FUDD	FUrm ozone and Diabatic Descent
GOME	Global Ozone Monitoring Experiment
HALOE	HALogen Occultation Experiment
ISCCP	International Satellite Cloud Climatology Project
IUP	Institut für UmweltPhysik
MAESTRO	Measurements of Aerosol Extinction in the Stratosphere and Troposphere Retrieved by Occultation
MLS	Microwave Limb Sounder
MPV	Modified Potential Vorticity
NPOESS	National Polar-orbiting Operational Environmental Satellite System
OMPS	Ozone Mapping and Profiler Suite
OSIRIS	Optical Spectrograph and InfraRed Imager System
POAM	Polar Ozone and Aerosol Measurement
PMD	Polarisation Measurement Device
PV	Potential Vorticity
RTE	Relative Transfer Equation
SAA	Solar Azimuth Angle
SABER	Sounding of the Atmosphere using Broadband Emission Radiometry

continued

continued

Abbreviations	Meanings
SAGE	Stratospheric Aerosol and Gas Experiment
SCIAMACHY	Scanning Imaging Absorption SpectroMeter for Atmospheric CartographY
SODD	SCIAMACHY Ozone and Diabatic Descent
SOLSE/LORE	Shuttle Ozone Limb Sounding Experiment/Limb Ozone Retrieval Experiment
SSW	Stratospheric Sudden Warming
SZA	Solar Zenith Angle
TH	Tangent Height
UARS	Upper Atmosphere Reseach Satellite
UKMO	United Kingdom Meteorological Office
UV	UltraViolet

Bibliography

- Amekudzi, L. K., Weber, M., Rozanov, A., von Savigny, C., Doicu, A., Lichtenberg, G., Bovensmann, H. and Burrows, J. P.: 2008, SCIAMACHY limb ozone and NO₂ current validation results, *37th COSPAR Scientific Assembly*, Vol. 37 of *COSPAR, Plenary Meeting*, p. 80.
- Baldwin, M. P., Gray, L. J., Dunkerton, T. J., Hamilton, K., Haynes, P. H., Randel, W. J., Holton, J. R., Alexander, M. J., Hirota, I., Horinouchi, T., Jones, D. B. A., Kinnnersley, J. S., Marquardt, C., Sato, K. and Takahashi, M.: 2001, The quasi-biennial oscillation, *Rev. Geophys.* **39**, 179–230.
- Bates, D. R. and Nicolet, M.: 1950, The photochemistry of atmospheric water vapor, *J. Geophys. Res.*, **55**, 301–327.
- Bovensmann, H., Burrows, J. P., Buchwitz, M., Frerick, J., Noël, S., Rozanov, V. V., Chance, K. V. and Goede, A. P. H.: 1999, SCIAMACHY: Mission Objectives and Measurement Modes, *J. Atmos. Sci.*, **56**, 127–150.
- Braathen, G. O., Rummukainen, M., Kyrö, E., Schmidt, U., Dahlback, A., Jørgensen, T. S., Fabian, R., Rudakov, V. V., Gil, M. and Borchers, R.: 1994, Temporal development of ozone within the Arctic vortex during the winter of 1991/92, *Geophys. Res. Lett.*, **21**, 1407–1410.
- Bracher, A., Bovensmann, H., Bramstedt, K., Burrows, J. P., von Clarmann, T., Eichmann, K.-U., Fischer, H., Funke, B., Gil-López, S., Glatthor, N., Grabowski, U., Höpfner, M., Kaufmann, M., Kellmann, S., Kiefer, M., Koukouli, M. E., Linden, A., López-Puertas, M., Tsidu, G. M., Milz, M., Noël, S., Rohen, G., Rozanov, A., Rozanov, V. V., von Savigny, C., Sinnhuber, M., Skupin, J., Steck, T., Stiller, G. P., Wang, D.-Y., Weber, M. and Wuttke, M. W.: 2005, Cross comparisons of O₃ and NO₂ measured by the atmospheric ENVISAT instruments GOMOS, MIPAS, and SCIAMACHY, *Adv. Space Res.*, **36**, 855–867.

- Brasseur, G. P. and Solomon, S.: 2005, *Aeronomy of the Middle Atmosphere: Chemistry and Physics of the Stratosphere and Mesosphere*, Springer, Berlin.
- Brewer, A. W.: 1949, Evidence for a world circulation provided by the measurements of helium and water vapour distribution in the stratosphere, *Q. J. Roy. Meteorol. Soc.*, **75**, 351–363.
- Burrows, J. P., Holzle, E., Goede, A. P. H., Visser, H. and Fricke, W.: 1995, SCIAMACHY–Scanning imaging absorption spectrometer for atmospheric cartography, *Acta Astronautica* **35**, 445–451.
- Butz, A., Bösch, H., Camy-Peyret, C., Chipperfield, M., Dorf, M., Dufour, G., Grunow, K., Jeseck, P., Köhl, S., Payan, S., Pepin, I., Pukite, J., Rozanov, A., von Savigny, C., Sioris, C., Wagner, T., Weidner, F. and Pfeilsticker, K.: 2006, Inter-comparison of stratospheric O₃ and NO₂ abundances retrieved from balloon borne direct sun observations and Envisat/SCIAMACHY limb measurements, *Atmos. Chem. Phys.*, **6**, 1293–1314.
- Callis, L. B. and Natarajan, M.: 1986, The Antarctic ozone minimum - Relationship to odd nitrogen, odd chlorine, the final warming, and the 11-year solar cycle, *J. Geophys. Res.*, **91**, 10771–10796.
- Chance, K. V., Burrows, J. P. and Schneider, W.: 1997, Satellite measurements of atmospheric ozone profiles, including tropospheric ozone, from ultraviolet/visible measurements in the nadir geometry: A potential method to retrieve tropospheric ozone, *J. Quant. Spectr. Rad. Trans.*, **57**, 4, 461–476.
- Chapman, S.: 1930, A theory of upper atmospheric ozone, *Mem. Roy. Soc.*, **3**, 103–109.
- Christensen, T., Knudsen, B. M., Streibel, M., Andersen, S. B., Benesova, A., Braathen, G., Claude, H., Davies, J., de Backer, H., Dier, H., Dorokhov, V., Gerding, M., Gil, M., Henchoz, B., Kelder, H., Kivi, R., Kyrö, E., Litynska, Z., Moore, D., Peters, G., Skrivankova, P., Stübi, R., Turunen, T., Vaughan, G., Viatte, P., Vik, A. F., von der Gathen, P. and Zaitcev, I.: 2005, Vortex-averaged Arctic ozone depletion in the winter 2002/2003, *Atmos. Chem. Phys.*, **5**, 131–138.
- Chubachi, S.: 1984, A special ozone observation at Syowa Station, Antarctica from February 1982 to January 1983, in S. A. Bowhill & B. Edwards (ed.), *Middle Atmosphere Program, Handbook for MAP*, Vol. 14, pp. 453–457.

- Crutzen, P. J.: 1971, Ozone production rates in oxygen-hydrogen-nitrogen oxide atmosphere, *J. Geophys. Res.*, **76**, 7311–7327.
- Degenstein, D. A., Bourassa, A. E., Roth, C. Z. and Llewellyn, E. J.: 2009, Limb scatter ozone retrieval from 10 to 60 km using a multiplicative algebraic reconstruction technique, *Atmos. Chem. Phys.*, **9**, 6521–6529.
- Dethof, A., O’Neill, A. and Slingo, J.: 2000, Quantification of the isentropic mass transport across the dynamical tropopause, *J. Geophys. Res.*, **105**, 12279–12294.
- Dobson, G. M. B., Kimball, H. H. and Kidson, E.: 1930, Observations of the amount of ozone in the Earth’s atmosphere, and its relation to other geophysical conditions. Part IV, *R. Soc. Lond. Proc. A*, **129**, 411–433.
- Dufour, G., Nassar, R., Boone, C. D., Skelton, R., Walker, K. A., Bernath, P. F., Rinsland, C. P., Semeniuk, K., Jin, J. J., McConnell, J. C. and Manney, G. L.: 2006, Partitioning between the inorganic chlorine reservoirs HCl and ClONO₂ during the Arctic winter 2005 from the ACE-FTS, *Atmos. Chem. Phys.*, **6**, 2355–2366.
- Dupuy, E., Walker, K. A., Kar, J., Boone, C. D., McElroy, C. T., Bernath, P. F., Drummond, J. R., Skelton, R., McLeod, S. D., Hughes, R. C., Nowlan, C. R., Dufour, D. G., Zou, J., Nichitiu, F., Strong, K., Baron, P., Bevilacqua, R. M., Blumenstock, T., Bodeker, G. E., Borsdorff, T., Bourassa, A. E., Bovensmann, H., Boyd, I. S., Bracher, A., Brogniez, C., Burrows, J. P., Catoire, V., Ceccherini, S., Chabrillat, S., Christensen, T., Coffey, M. T., Cortesi, U., Davies, J., de Clercq, C., Degenstein, D. A., de Mazière, M., Demoulin, P., Dodion, J., Firanski, B., Fischer, H., Forbes, G., Froidevaux, L., Fussen, D., Gerard, P., Godin-Beekman, S., Goutail, F., Granville, J., Griffith, D., Haley, C. S., Hannigan, J. W., Höpfner, M., Jin, J. J., Jones, A., Jones, N. B., Jucks, K., Kagawa, A., Kasai, Y., Kerzenmacher, T. E., Kleinböhl, A., Klekociuk, A. R., Kramer, I., Küllmann, H., Kuttippurath, J., Kyrölä, E., Lambert, J.-C., Livesey, N. J., Llewellyn, E. J., Lloyd, N. D., Mahieu, E., Manney, G. L., Marshall, B. T., McConnell, J. C., McCormick, M. P., McDermid, I. S., McHugh, M., McLinden, C. A., Mellqvist, J., Mizutani, K., Murayama, Y., Murtagh, D. P., Oelhaf, H., Parrish, A., Petelina, S. V., Piccolo, C., Pommereau, J.-P., Randall, C. E., Robert, C., Roth, C., Schneider, M., Senten, C., Steck, T., Strandberg, A., Strawbridge, K. B., Sussmann, R., Swart, D. P. J., Tarasick, D. W., Taylor, J. R., Tétard, C., Thomason, L. W., Thompson, A. M., Tully, M. B., Urban, J., Vanhellemont, F., von Clarmann, T., von der Gathen, P., von Savigny, C., Waters, J. W., Witte, J. C., Wolff, M. and

- Zawodny, J. M.: 2009, Validation of ozone measurements from the Atmospheric Chemistry Experiment (ACE), *Atmos. Chem. Phys.*, **9**, 287–343.
- Ebojie, F.: 2009, *Investigation of long-term variations in stratospheric ozone through the combination of different satellite ozone data sets*, M.S. thesis, University of Bremen, Bremen, Germany.
- Eichmann, K.-U., Weber, M., Bramstedt, K. and Burrows, J. P.: 2002, Ozone depletion in Northern Hemisphere winter/spring 1999/2000 as measured by the Global Ozone Monitoring Experiment on ERS-2, *J. Geophys. Res. (Atmos.)*, **107**, 8280.
- Eluszkiewicz, J., Crisp, D., Zurek, R., Elson, L., Fishbein, E., Froidevaux, L., Waters, J., Grainger, R. G., Lambert, A., Harwood, R. and Peckham, G.: 1996, Residual circulation in the stratosphere and lower mesosphere as diagnosed from Microwave Limb Sounder data., *J. Atmos. Sci.*, **53**, 217–240.
- Erle, F., Pfeilsticker, K. and Platt, U.: 1995, On the influence of tropospheric clouds on zenith-scattered-light measurements of stratospheric species, *Geophys. Res. Lett.*, **22**, 2725 – 2728.
- Farman, J. C., Gardiner, B. G. and Shanklin, J. D.: 1985, Large losses of total ozone in Antarctica reveal seasonal ClO_x/NO_x interaction, *Nature*, **315**, 207–210.
- Farmer, C. B., Toon, G. C., Schaper, P. W., Blavier, J.-F. and Lowes, L. L.: 1987, Stratospheric trace gases in the spring 1986 Antarctic atmosphere, *Nature*, **329**, 126–130.
- Flittner, D. E., Bhartia, P. K. and Herman, B. M.: 2000, O₃ profiles retrieved from limb scatter measurements: Theory, *Geophys. Res. Lett.*, **27**, 2601–2604.
- Goede, A. P. H., van Baren, C., Aarts, H. J. M., Burrows, J. P. and Change, K. V.: 1991, SCIAMACHY instrument design, *Adv. Space Res.*, **11**, 243–246.
- Gottwald, M., Bovensmann, H., Lichtenberg, G., Noël, S., von Barga, A., Slijkhuis, S., Piders, A., Hoogeveen, R., von Savigny, C., Buchwitz, M., Kokhanovsky, A., Richter, A., Rozanov, A., Holzer-Popp, T., Bramstedt, K., Lambert, J.-C., Skupin, J., Wittrock, F., Schrijver, H. and Burrows, J. P.: 2006, *SCIAMACHY, Monitoring the Changing Earth's Atmosphere*, DLR.
- Groß, J.-U., Günther, G., Müller, R., Konopka, P., Bausch, S., Schlager, H., Voigt, C., Volk, C. M. and Toon, G. C.: 2005, Simulation of denitrification and ozone loss for the Arctic winter 2002/2003, *Atmos. Chem. Phys.*, **5**, 1437–1448.

- Grooß, J.-U. and Müller, R.: 2007, Simulation of ozone loss in Arctic winter 2004/2005, *Geophys. Res. Lett.*, **34**, L05804.
- Grooß, J.-U., Müller, R., Konopka, P., Steinhorst, H., Engel, A., Möbius, T. and Volk, C. M.: 2008, The impact of transport across the polar vortex edge on March ozone loss estimates, *Atmos. Chem. Phys.*, **8**, 565–578.
- Haley, C. S., Brohede, S. M., Sioris, C. E., Griffioen, E., Murtagh, D. P., McDade, I. C., Eriksson, P., Llewellyn, E. J., Bazureau, A. and Goutail, F.: 2004, Retrieval of stratospheric O₃ and NO₂ profiles from Odin Optical Spectrograph and Infrared Imager System (OSIRIS) Limb-Scattered Sunlight Measurements, *J. Geophys. Res.*, **109**, D16303.
- Hampson, J.: 1964, Photochemical behaviour of the ozone layer, *Tech. rep., Canadian Armament Research and Development Establishment, CARDE technical note*, p. 1627.
- Hansen, J. E. and Travis, L. D.: 1974, Light scattering in planetary atmospheres, *Space Sci. Rev.*, **16**, 527–610.
- Hay, P. J. and Dunning, T. H.: 1977, Geometries and energies of the excited states of O₃ from ab initio potential energy surfaces, *J. Chem. Phys.*, **67**, 2290–2303.
- Heidt, L. E., Lueb, R., Pollock, W. and Ehhalt, D. H.: 1975, Stratospheric profiles of CCl₃F and CCl₂F₂, *Geophys. Res. Lett.*, **2**, 445–447.
- Hendrick, F., van Roozendaal, M., Kylling, A., Petritoli, A., Rozanov, A., Sanghavi, S., Schofield, R., von Friedeburg, C., Wagner, T., Wittrock, F., Fonteyn, D. and de Mazière, M.: 2006, Intercomparison exercise between different radiative transfer models used for the interpretation of ground-based zenith-sky and multi-axis DOAS observations, *Atmos. Chem. Phys.*, **6**, 93–108.
- Holton, J. R.: 1992, *An introduction to dynamic meteorology*, Academic Press, New York.
- Holton, J. R., Haynes, P. H., McIntyre, M. E., Douglass, A. R., Rood, R. B. and Pfister, L.: 1995, Stratosphere–troposphere exchange, *Rev. Geophys.* **33**, 403–439.
- Holton, J. R. and Tan, H. C.: 1980, The influence of the equatorial QBO in the global circulation at 50mb., *J. Atmos. Sci.* **37**, 2200 – 2208.

- Hoogen, R., Rozanov, V. V. and Burrows, J. P.: 1999, Ozone profiles from GOME satellite data: algorithm description and first validation, *J. Geophys. Res.*, **14**, 7, 8263–8280.
- Hoppel, K., Bevilacqua, R., Allen, D., Nedoluha, G. and Randall, C.: 2003, POAM III observations of the anomalous 2002 Antarctic ozone hole, *Geophys. Res. Lett.*, **30**, 7, 1394.
- Hoppel, K., Bevilacqua, R., Nedoluha, G., Deniel, C., Lefèvre, F., Lumpe, J., Fromm, M., Randall, C., Rosenfield, J. and Rex, M.: 2002, POAM III observations of Arctic ozone loss for the 1999/2000 winter, *J. Geophys. Res. (Atmos.)*, **107**, D20, 8262.
- Johnston, H.: 1971, Reduction of stratospheric ozone by nitrogen oxide catalysts from supersonic transport exhaust, *Science*, **173**, 517–522.
- Jones, A., Urban, J., Murtagh, D. P., Eriksson, P., Brohede, S., Haley, C., Degenstein, D., Bourassa, A., von Savigny, C., Sonkaew, T., Rozanov, A., Bovensmann, H. and Burrows, J.: 2009, Evolution of stratospheric ozone and water vapour time series studied with satellite measurements, *Atmos. Chem. Phys.*, **9**, 6055–6075.
- Jucks, K. W. and Salawitch, R. J.: 2000, Future changes in upper stratospheric ozone. In: Atmospheric Science Across the Stratopause, *Geophys. Monograph S., American Geophys. Union*, **123**, 241–255.
- Knudsen, B. M., Larsen, N., Mikkelsen, I. S., Morcrette, J., Braathen, G. O., Kyrö, E., Fast, H., Gernandt, H., Kanzawa, H., Nakane, H., Dorokhov, V., Yushkov, V., Hansen, G., Gil, M. and Shearman, R. J.: 1998, Ozone depletion in and below the Arctic vortex for 1997, *Geophys. Res. Lett.*, **25**, 627–630.
- Kokhanovsky, A.: 2004, Optical properties of terrestrial clouds, *Earth Sci. Rev.*, **64**, 189–241.
- Kokhanovsky, A. A.: 2001, *Optics of light scattering media: Problems and Solutions*, Springer, Berlin.
- Kokhanovsky, A. A.: 2006, *Cloud Optics*, Springer, Berlin.
- Kokhanovsky, A. A. and Rozanov, V. V.: 2004, The physical parameterization of the top-of-atmosphere reflection function for a cloudy atmosphere-underlying surface system: the oxygen A-band case study, *J. Quant. Spectrosc. Radiat. Transfer*, **85**, 35–55.

- Komhyr, W. D., Grass, R. D. and Leonard, R. K.: 1986, Total ozone decrease at South Pole Antarctica 1964-1985, *Geophys. Res. Lett.*, **13**, 1248–1251.
- Konopka, P., Engel, A., Funke, B., Müller, R., Grooß, J.-U., Günther, G., Wetter, T., Stiller, G., von Clarmann, T., Glatthor, N., Oelhaf, H., Wetzel, G., López-Puertas, M., Pirre, M., Huret, N. and Riese, M.: 2007, Ozone loss driven by nitrogen oxides and triggered by stratospheric warmings can outweigh the effect of halogens, *J. Geophys. Res. (Atmos.)*, **112**, 11, D5105.
- Konopka, P., Grooß, J.-U., Hoppel, K. W., Steinhorst, H.-M. and Müller, R.: 2005, Mixing and Chemical Ozone Loss during and after the Antarctic Polar Vortex Major Warming in September 2002, *J. Atmos. Sci.*, **62**, 848–859.
- Kurosu, T., Rozanov, V. V. and Burrows, J. P.: 1997, Parameterization schemes for terrestrial water clouds in the radiative transfer model GOMETRAN, *J. Geophys. Res.*, **102**, 21809–21824.
- Lait, L. R.: 1994, An Alternative Form for Potential Vorticity., *J. Atmos. Sci.*, **51**, 1754–1759.
- Lehmann, R., von der Gathen, P., Rex, M. and Streibel, M.: 2005, Statistical analysis of the precision of the Match method, *Atmos. Chem. Phys.*, **5**, 2713–2727.
- Lelieveld, J., Crutzen, P. J. and Rodhe, H.: 1989, Zonal average cloud characteristics for global atmospheric chemistry modeling, *Report CM-76, Department of Meteorology, University of Stockholm* .
- Lenoble, J.: 1985, *Radiative transfer in scattering and absorbing atmospheres: Standard computational procedures*, Hampton, VA, USA, A. Deepak Publishing.
- Liou, K. N.: 1973, A numerical experiment on Chandrasekhar's Discrete-Ordinate method for radiative transfer: Applications to cloudy and hazy atmospheres, *J. Atmos. Sci.*, **30**, 1303–1326.
- Llewellyn, E., Lloyd, N. D., Degenstein, D. A., Gattinger, R. L., Petelina, S. V., Bourassa, A. E., Wiensz, J. T., Ivanov, E. V., McDade, I. C., Solheim, B. H., McConnell, J. C., Haley, C. S., von Savigny, C., Sioris, C. E., McLinden, C. A., Griffioen, E., Kaminski, J., Evans, W. F. J., Puckrin, E., Strong, K., Wehrle, V., Hum, R. H., Kendall, D. J. W., Matsushita, J., Murtagh, D. P., Brohede, S., Stegman, J., Witt, G., Barnes, G., Payne, W. F., Piche, L., Smith, K., Warshaw, G., Deslauniers, D. L., Marchand, P., Richardson, E. H., King, R. A., Wevers, I., McCreath, W.,

- Kyrölä, E., Oikarinen, L., Leppelmeier, G. W., Auvinen, H., Megie, G., Hauchecorne, A., Lefevre, F., de La Noe, J., Ricaud, P., Frisk, U., Sjöberg, F., von Scheele, F. and Nordh, L.: 2004, The OSIRIS instrument on the Odin spacecraft, *Can. J. Phys.*, **82**, 411–422.
- Loughman, R. P., Flittner, D. E., Herman, B. M., Bhartia, P. K., Hilsenrath, E. and McPeters, R. D.: 2005, Description and sensitivity analysis of a limb scattering ozone retrieval algorithm, *J. Geophys. Res. (Atmos.)*, **110**, D19301.
- Loughman, R. P., Griffioen, E., Oikarinen, L., Postylyakov, O. V., Rozanov, A., Flittner, D. E. and Rault, D. F.: 2004, Comparison of radiative transfer models for limb-viewing scattered sunlight measurements, *J. Geophys. Res. (Atmos.)*, **109**, D06303.
- Lovelock, J. E. and Maggs, R. J.: 1973, Halogenated Hydrocarbons in and over the Atlantic, *Nature*, **241**, 194–196.
- Mace, G. G., Marchand, R., Zhang, Q. and Stephens, G.: 2007, Global hydrometeor occurrence as observed by CloudSat: Initial observations from summer 2006, *Geophys. Res. Lett.*, **34**, L09808.
- Mankin, W. G. and Coffey, M. T.: 1989, Airborne Observations of Chemical Constituents in the Antarctic Winter Stratosphere, in R. D. Bojkov & P. Fabian (ed.), *Ozone in the Atmosphere*, p. 22.
- Manney, G. L., Krüger, K., Sabutis, J. L., Sena, S. A. and Pawson, S.: 2005a, The remarkable 2003–2004 winter and other recent warm winters in the Arctic stratosphere since the late 1990s, *J. Geophys. Res. (Atmos.)*, **110**, D04107.
- Manney, G. L., Sabutis, J. L., Allen, D. R., Lahoz, W. A., Scaife, A. A., Randall, C. E., Pawson, S., Naujokat, B. and Swinbank, R.: 2005b, Simulations of Dynamics and Transport during the September 2002 Antarctic Major Warming., *J. Atmos. Sci.*, **62**, 690–707.
- Manney, G. L., Schwartz, M. J., Krüger, K., Santee, M. L., Pawson, S., Lee, J. N., Daffer, W. H., Fuller, R. A. and Livesey, N. J.: 2009, Aura Microwave Limb Sounder observations of dynamics and transport during the record-breaking 2009 Arctic stratospheric major warming, *Geophys. Res. Lett.*, **36**, 12815–12821.
- Manney, G. L., Zurek, R. W., Froidevaux, L., Waters, J. W., O’Neill, A. and Swinbank, R.: 1995b, Lagrangian transport calculations using UARS data. Part II: Ozone., *J. Atmos. Sci.*, **52**, 3069–3081.

- Manney, G. L., Zurek, R. W., Lahoz, W. A., Harwood, R. S., Gille, J. C., Kumer, J. B., Mergenthaler, J. L., Roche, A. E., O'Neill, A., Swinbank, R. and Waters, J. W.: 1995a, Lagrangian Transport Calculations Using UARS Data. Part I. Passive Tracers., *J. Atmos. Sci.*, **52**, 3049–3068.
- McElroy, M. B., Salawitch, R. J., Wofsy, S. C. and Logan, J. A.: 1986, Antarctic ozone: Reductions due to synergistic interactions of chlorine and bromine, *Nature*, **321**, 759–762.
- McPeters, R. D., Janz, S. J., Hilsenrath, E., Brown, T. L., Flittner, D. E. and Heath, D. F.: 2000, The retrieval of O₃ profiles from limb scatter measurements: Results from the Shuttle Ozone Limb Sounding Experiment, *Geophys. Res. Lett.*, **27**, 2597–2600.
- Molina, L. T. and Molina, M. J.: 1987, Production of Cl₂O₂ from the selfreaction of the ClO radical, *J. Phys. Chem.*, **91**, 433–436.
- Mount, G. H., Sanders, R. W., Schmeltekopf, A. L. and Solomon, S.: 1987, Visible spectroscopy at McMurdo Station Antarctica 1. Overview and daily variations of NO₂ and O₃ during austral spring, *J. Geophys. Res.*, **92**, 8320–8328.
- Müller, R., Crutzen, P. J., Groöß, J.-U., Brühl, C., Russell, J. M., Gernandt, H., McKenna, D. S. and Tuck, A. F.: 1997, Severe chemical ozone loss in the Arctic during the winter of 1995-96, *Nature*, **389**, 709–712.
- Müller, R. and Günther, G.: 2003, A Generalized Form of Lait's Modified Potential Vorticity., *J. Atmos. Sci.*, **60**, 2229–2237.
- Müller, R., McKenna, D. S., Schmidt, U., Engel, A. and Proffitt, M. H.: 2001, The O₃-N₂O relation from balloon-borne observations as a measure of Arctic ozone loss in 1991/92, *Q. J. Roy. Meteor. Soc.*, **127**, 1389–1412.
- Newchurch, M. J., Yang, E., Cunnold, D. M., Reinsel, G. C., Zawodny, J. M. and Russell, J. M.: 2003, Evidence for slowdown in stratospheric ozone loss: First stage of ozone recovery, *J. Geophys. Res. (Atmos.)*, **108**, 4507.
- Oikarinen, L., Sihvola, E. and Kyrölä, E.: 1999, Multiple scattering radiance in limb-viewing geometry, *J. Geophys. Res.*, **104**, 31261–31274.
- Olsen, M. A., Schoeberl, M. R. and Douglass, A. R.: 2004, Stratosphere-troposphere exchange of mass and ozone, *J. Geophys. Res. (Atmos.)*, **109**, D24114.

- Prather, M. J. and Remsberg, E. E.: 1993, The atmospheric effects of stratospheric aircraft: Report of the 1992 models and measurements workshop, NASA reference publication 1292, *National Aeronautics and Space Administration, Washington, DC, USA*, **1–3**.
- Prinn, R., Cunnold, D., Rasmussen, R., Simmonds, P., Alyea, F., Crawford, A., Fraser, P. and Rosen, R.: 1987, Atmospheric trends in Methylchloroform and the global average for the Hydroxyl radical, *Science*, **238**, 945–950.
- Proffitt, M. H., Margitan, J. J., Kelly, K. K., Loewenstein, M., Podolske, J. R. and Chan, K. R.: 1990, Ozone loss in the Arctic polar vortex inferred from high-altitude aircraft measurements, *Nature*, **347**, 31–36.
- Pruppacher, H. R. and Jaenicke, R.: 1995, The processing of water vapor and aerosols by atmospheric clouds, a global estimation, *Atmos. Res.*, **38**, 283–295.
- Randel, W. J. and Wu, F.: 1999, Cooling of the Arctic and Antarctic polar stratospheres due to ozone depletion., *J. Clim.*, **12**, 1467–1479.
- Randel, W. J., Wu, F., Russell, III, J. M., Roche, A. and Waters, J. W.: 1998, Seasonal cycles and QBO variations in stratospheric CH₄ and H₂O observed in UARS HALOE data., *J. Atmos. Sci.* **55**, 163–185.
- Rault, D. F.: 2005, Ozone profile retrieval from Stratospheric Aerosol and Gas Experiment (SAGE III) limb scatter measurements, *J. Geophys. Res. (Atmos.)*, **110**, D09309.
- Rex, M., Salawitch, R. J., Deckelmann, H., von der Gathen, P., Harris, N. R. P., Chipperfield, M. P., Naujokat, B., Reimer, E., Allaart, M., Andersen, S. B., Bevilacqua, R., Braathen, G. O., Claude, H., Davies, J., De Backer, H., Dier, H., Dorokhov, V., Fast, H., Gerding, M., Godin-Beekmann, S., Hoppel, K., Johnson, B., Kyrö, E., Litynska, Z., Moore, D., Nakane, H., Parrondo, M. C., Risley, A. D., Skrivankova, P., Stübi, R., Viatte, P., Yushkov, V. and Zerefos, C.: 2006, Arctic winter 2005: Implications for stratospheric ozone loss and climate change, *Geophys. Res. Lett.*, **33**, L23808.
- Rex, M., Salawitch, R. J., Santee, M. L., Waters, J. W., Hoppel, K. and Bevilacqua, R.: 2003, On the unexplained stratospheric ozone losses during cold Arctic Januaries, *Geophys. Res. Lett.*, **30**, 1, 1008.
- Rex, M., Salawitch, R. J., von der Gathen, P., Harris, N. R. P., Chipperfield, M. P. and Naujokat, B.: 2004, Arctic ozone loss and climate change, *Geophys. Res. Lett.*, **31**, L04116.

- Ricaud, P., Lefèvre, F., Berthet, G., Murtagh, D., Llewellyn, E. J., Mégie, G., Kyrölä, E., Leppelmeier, G. W., Auvinen, H., Boone, C., Brohede, S., Degenstein, D. A., de La Noë, J., Dupuy, E., El Amraoui, L., Eriksson, P., Evans, W. F. J., Frisk, U., Gattinger, R. L., Girod, F., Haley, C. S., Hassinen, S., Hauchecorne, A., Jimenez, C., Kyrö, E., Lautié, N., Le Flochmoën, E., Lloyd, N. D., McConnell, J. C., McDade, I. C., Nordh, L., Olberg, M., Pazmino, A., Petelina, S. V., Sandqvist, A., Seppälä, A., Sioris, C. E., Solheim, B. H., Stegman, J., Strong, K., Taalas, P., Urban, J., von Savigny, C., von Scheele, F. and Witt, G.: 2005, Polar vortex evolution during the 2002 Antarctic major warming as observed by the Odin satellite, *J. Geophys. Res. (Atmos.)*, **110**, 9, D5302.
- Rodgers, C. D.: 1971, Some theoretical aspects of remote sounding in the Earth's atmosphere, *J. Quant. Spectr. Rad. Trans.*, **11**, 767–777.
- Rodgers, C. D.: 1976, Retrieval of atmospheric temperature and composition from remote measurements of thermal radiation, *Rev. Geophys. Space Phys.*, **14**, 609–624.
- Rodgers, C. D.: 1990, Characterization and error analysis of profiles retrieved from remote sounding measurements, *J. Geo. Phys. Res.*, **95**, 5587–5595.
- Rodgers, C. D.: 1998, Some theoretical aspects of remote sounding in the Earth's atmosphere, *Adv. Space Res.*, **21**, 361–367.
- Rodgers, C. D.: 2000, *Inverse methods for atmospheric sounding: Theory and practice*, World Scientific Publishing, Singapore.
- Roebeling, R. A., Berk, A., Feijt, A. J., Frerichs, W., Joliver, D., M. A. and Stammes, P.: 2005, Sensitivity of cloud property retrievals to differences in radiative transfer simulations, *Technical Report WR-2005-02, KNMI, Netherlands* .
- Rohen, G. J., von Savigny, C., Llewellyn, E. J., Kaiser, J. W., Eichmann, K.-U., Bracher, A., Bovensmann, H. and Burrows, J. P.: 2006, First results of ozone profiles between 35 and 65 km retrieved from SCIAMACHY limb spectra and observations of ozone depletion during the solar proton events in October/November 2003, *Adv. Space Res.*, **37**, 2263–2268.
- Rosenfield, J. E., Newman, P. A. and Schoeberl, M. R.: 1994, Computations of diabatic descent in the stratospheric polar vortex, *J. Geophys. Res.*, **99**, 16677–16689.

- Rösevall, J. D., Murtagh, D. P., Urban, J., Feng, W., Eriksson, P. and Brohede, S.: 2008, A study of ozone depletion in the 2004/2005 Arctic winter based on data from Odin/SMR and Aura/MLS, *J. Geophys. Res. (Atmos.)*, **113**, 12, D13301.
- Rossow, W. B. and Schiffer, R. A.: 1999, Advances in Understanding Clouds from ISCCP, *Bull. Amer. Meteor. Soc.*, **80**, 2261–2288.
- Roth, C. Z., Degenstein, D. A., Bourassa, A. E. and Llewellyn, E. J.: 2007, The retrieval of vertical profiles of ozone number density using Chappuis band absorption information and a multiplicative algebraic reconstruction technique, *Can. J. Phys.*, **85**, 1225–1243.
- Rowland, F. S.: 1991, Stratospheric ozone depletion, *Annu. Rev. Phys. Chem.*, **42**, 731–768.
- Rowland, F. S.: 2006, Stratospheric ozone depletion, *Philos. Trans. R. Soc. Lond. B Biol. Sci.*, **361**, 1469, 769–790.
- Rowland, F. S. and Molina, M. J.: 1975, Chlorofluoromethanes in the Environment, *Rev. Geophys. Space Phys.*, **13**, 1–15.
- Rožanov, A.: 2001, *Modelling of radiative transfer through a spherical planetary atmosphere: Application to atmospheric trace gases retrieval from occultation- and limb-measurements in UV-Vis-NIR*, Ph.D. thesis, University of Bremen, Bremen, Germany.
- Rožanov, A.: 2008, SCIATRAN 2.X: Radiative transfer model and retrieval software package, <http://www.iup.physik.uni-bremen.de/sciattran> .
- Rožanov, A., Bovensmann, H., Bracher, A., Hrechanyy, S., Rožanov, V., Sinnhuber, M., Stroh, F. and Burrows, J. P.: 2005a, NO₂ and BrO vertical profile retrieval from SCIAMACHY limb measurements: Sensitivity studies, *Adv. Space Res.*, **36**, 5, 846–854.
- Rožanov, A., Eichmann, K.-U., von Savigny, C., Bovensmann, H., Burrows, J. P., von Barmen, A., Doicu, A., Hilgers, S., Godin-Beekmann, S., Leblanc, T. and McDermid, I. S.: 2007, Comparison of the inversion algorithms applied to the ozone vertical profile retrieval from SCIAMACHY limb measurements, *Atmos. Chem. Phys.*, **7**, 4763–4779.

- Rozanov, A., Rozanov, V., Buchwitz, M., Kokhanovsky, A. and Burrows, J. P.: 2005b, SCIATRAN 2.0 - A new radiative transfer model for geophysical applications in the 175 – 2400 nm spectral region, *Adv. Space Res.*, **36**, 1015–1019.
- Rozanov, A., Rozanov, V. and Burrows, J. P.: 2001, A numerical radiative transfer model for a spherical planetary atmosphere: combined differential-integral approach involving the Picard iterative approximation, *J. Quant. Spectr. Rad. Trans.*, **69**, 491–512.
- Rozanov, V. V.: 2006, *Adjoint radiative transfer equation and inverse problems*, In 'Light Scattering Reviews', Ed. by A. A. Kokhanovsky, Springer, Praxis Publishing, Chichester, UK.
- Rozanov, V. V. and Kokhanovsky, A. A.: 2004, Semianalytical cloud retrieval algorithm as applied to the cloud top altitude and the cloud geometrical thickness determination from top-of-atmosphere reflectance measurements in the oxygen A band, *J. Geophys. Res. (Atmos.)*, **109**, D05202.
- Rozanov, V. V. and Kokhanovsky, A. A.: 2006, Determination of cloud geometrical thickness using backscattered solar light in a gaseous absorption band, *IEEE Geosci. Rem. Sens. Lett.*, **3**, 250–253.
- Rozanov, V. V. and Kokhanovsky, A. A.: 2008, *Impact of single- and multi-layered cloudiness on ozone vertical column retrievals using nadir observations of backscattered solar radiation*, In 'Light Scattering Reviews 3', Springer, Praxis Publishing, Chichester, UK.
- Rusch, D. W., Mount, G. H., Barth, C. A., Rottmann, G. J., Thomas, R. J., Thomas, G. E., Sanders, R. W., Lawrence, G. M. and Eckman, R. S.: 1983, Ozone densities in the lower mesosphere measured by a limb scanning UltraViolet Spectrometer, *Geophys. Res. Lett.*, **10**, 4, 241–244.
- Sathishkumar, S., Sridharan, S. and Jacobi, C.: 2009, Dynamical response of low-latitude middle atmosphere to major sudden stratospheric warming events, *J. Atmos. Sol. Terr. Phys.*, **71**, 857–865.
- Schmeltekopf, A. L., Goldan, P. D., Henderson, W. R., Harrop, W. J., Thompson, T. L., Fehsenfeld, F. C., Schiff, H. I., Crutzen, P. J., Isaksen, I. S. A. and Ferguson, E. E.: 1975, Measurements of stratospheric CFCl_3 , CF_2Cl_2 , and N_2O , *Geophys. Res. Lett.*, **2**, 393–396.

- Shine, K. P.: 1991, On the cause of the relative greenhouse strength of gases such as the halocarbons, *J. Atmos. Sci.* **48**, 1513–1518.
- Siewert, C. E.: 2000, A discrete-ordinates solution for radiative-transfer models that include polarization effects, *Quant. Spectr. Rad. Trans.*, **64**, 227–254.
- Singleton, C. S., Randall, C. E., Chipperfield, M. P., Davies, S., Feng, W., Bevilacqua, R. M., Hoppel, K. W., Fromm, M. D., Manney, G. L. and Harvey, V. L.: 2005, 2002-2003 Arctic ozone loss deduced from POAM III satellite observations and the SLIMCAT chemical transport model, *Atmos. Chem. Phys.*, **5**, 597–609.
- Singleton, C. S., Randall, C. E., Harvey, V. L., Chipperfield, M. P., Feng, W., Manney, G. L., Froidevaux, L., Boone, C. D., Bernath, P. F., Walker, K. A., McElroy, C. T. and Hoppel, K. W.: 2007, Quantifying Arctic ozone loss during the 2004-2005 winter using satellite observations and a chemical transport model, *J. Geophys. Res. (Atmos.)*, **112**, D7304.
- Sinnhuber, B.-M., Langer, J., Klein, U., Raffalski, U., Künzi, K. and Schrems, O.: 1998, Ground based millimeter-wave observations of Arctic ozone depletion during winter and spring of 1996/97, *Geophys. Res. Lett.*, **25**, 3327–3330.
- Sioris, C. E., Haley, C. S., McLinden, C. A., von Savigny C., McDade, I. C., McConnell, J. C., Evans, W. F. J., Lloyd, N. D., Llewellyn, E. J., Chance, K. V., Kurosu, T. P., Murtagh, D., Frisk, U., Pfeilsticker, K., Bösch, H., Weidner, F., Strong, K., Stegman, J. and Mégie, G.: 2003, Stratospheric profiles of nitrogen dioxide observed by Optical Spectrograph and Infrared Imager System on the Odin satellite, *J. Geophys. Res.*, **108**, D74215.
- Siskind, D. E., Froidevaux, L., Russell, J. M. and Lean, J.: 1998, Implications of upper stratospheric trace constituent changes observed by HALOE for O₃ and ClO from 1992 to 1995, *Geophys. Res. Lett.* **25**, 3513–3516.
- Solomon, S.: 1999, Stratospheric ozone depletion: A review of concepts and history, *Rev. Geophys.*, **37**, 275–316.
- Solomon, S., Garcia, R. R., Rowland, F. S. and Wuebbles, D. J.: 1986, On the depletion of Antarctic ozone, *Nature*, **321**, 755–758.
- Steinbrecht, W., Claude, H., Schönenborn, F., McDermid, I. S., Leblanc, T., Godin-Beekmann, S., Keckhut, P., Hauchecorne, A., van Gijssel, J. A. E., Swart, D. P. J., Bodeker, G. E., Parrish, A., Boyd, I. S., Kampfer, N., Hocke, K., Stolarski, R. S.,

- Frith, S. M., Thomason, L. W., Remsberg, E. E., von Savigny, C., Rozanov, A. and Burrows, J. P.: 2009, Ozone and temperature trends in the upper stratosphere at five stations of the Network for the Detection of Atmospheric Composition Change, *Int. J. Rem. Sens.*, **30**, 3875–3886.
- Steinfeld, J. I., Adler-Golden, S. M. and Gallagher, J. W.: 1987, Critical survey of data on the spectroscopy and kinetics of ozone in the mesosphere and thermosphere, *J. Phys. Chem. Ref. Data*, **16**, 911–951.
- Stolarski, R. S. and Cicerone, R. J.: 1974, Stratospheric chlorine: A possible sink for ozone, *Can. J. Chem.*, **52**, 1610–1615.
- Stolarski, R. S., Krueger, A. J., Schoeberl, M. R., McPeters, R. D., Newman, P. A. and Alpert, J. C.: 1986, Nimbus-7 satellite measurements of the springtime antarctic ozone decrease, *Nature*, **322**, 808–811.
- Stolarski, R. S., McPeters, R. D. and Newman, P. A.: 2005, The ozone hole of 2002 as measured by TOMS., *J. Atmos. Sci.* **62**, 716–720.
- Thorne, A. P., Litzen, U. and Johansson, S.: 1999, *Spectrophysics: Principles and Applications*, Springer, Berlin.
- Trishchenko, A. P., Li, Z., Chang, F.-L. and Barker, H.: 2001, Cloud optical depths and TOA fluxes: Comparison between satellite and surface retrievals from multiple platforms, *Geophys. Res. Lett.*, **28**, 979–982.
- Tukiainen, S., Hassinen, S., Seppälä, A., Auvinen, H., Kyrölä, E., Tamminen, J., Haley, C. S., Lloyd, N. and Verronen, P. T.: 2008, Description and validation of a limb scatter retrieval method for Odin/OSIRIS, *J. Geophys. Res. (Atmos.)*, **113**, D04308.
- Tung, K. K., Ko, M. K. W., Rodriguez, J. and Sze, N. D.: 1986, Are Antarctic ozone variations manifestations of dynamics or chemistry?, *Nature*, **333**, 811–814.
- Vanbauce, C., Cadet, B. and Marchand, R. T.: 2003, Comparison between satellite and surface retrievals from multiple platforms, *Geophys. Res. Lett.*, **28**, 979–982.
- von Savigny, C.: 2002, *Retrieval of stratospheric ozone density profiles from OSIRIS scattered sunlight observations*, Ph.D. thesis, York University, Toronto, Canada.
- von Savigny, C., Haley, C. S., Sioris, C. E., McDade, I. C., Llewellyn, E. J., Degenstein, D., Evans, W. F. J., Gattinger, R. L., Griffioen, E., Kyrölä, E., Lloyd, N. D., McConnell, J. C., McLinden, C. A., Mégie, G., Murtagh, D. P. and Solheim, B.: 2003,

- Stratospheric ozone profiles retrieved from limb scattered sunlight radiance spectra measured by the OSIRIS instrument on the Odin satellite, *Geophys. Res. Lett.*, **30**, 14, 1755–1758.
- von Savigny, C., McDade, I. C., Griffioen, E., Haley, C. S., Sioris, C. E. and Llewellyn, E. J.: 2005a, Sensitivity studies and first validation of stratospheric ozone profile retrievals from Odin/OSIRIS observations of limb scattered solar radiation, *Can. J. Phys.*, **83**, 9, 957–972.
- von Savigny, C., Rozanov, A., Bovensmann, H., Eichmann, K.-U., Noël, S., Rozanov, V., Sinnhuber, B.-M., Weber, M., Burrows, J. P. and Kaiser, J. W.: 2005b, The ozone hole breakup in September 2002 as seen by SCIAMACHY on Envisat, *J. Atmos. Sci.*, **62**, 3, 721–734.
- von Savigny, C., Ulasi, E. P., Eichmann, K., Bovensmann, H. and Burrows, J. P.: 2005c, Detection and mapping of polar stratospheric clouds using limb scattering observations, *Atmos. Chem. Phys.*, **5**, 3071–3079.
- Wagner, T., Burrows, J. P., Deutschmann, T., Dix, B., von Friedeburg, C., Frieß, U., Hendrick, F., Heue, K.-P., Irie, H., Iwabuchi, H., Kanaya, Y., Keller, J., McLinden, C. A., Oetjen, H., Palazzi, E., Petritoli, A., Platt, U., Postylyakov, O., Pukite, J., Richter, A., van Roozendaal, M., Rozanov, A., Rozanov, V., Sinreich, R., Sanghavi, S. and Wittrock, F.: 2007, Comparison of box-air-mass-factors and radiances for Multiple-Axis Differential Optical Absorption Spectroscopy (MAX-DOAS) geometries calculated from different UV/visible radiative transfer models, *Atmos. Chem. Phys.*, **7**, 1809–1833.
- Wayne, R. P.: 1987, The photochemistry of ozone, *Atm. Environment*, **21**, 8, 1683–1694.
- Wayne, R. P.: 2000, *Chemistry of Atmospheres*, Oxford University Press.
- Weber, M., Dhomse, S., Wittrock, F., Richter, A., Sinnhuber, B.-M. and Burrows, J. P.: 2003, Dynamical control of NH and SH winter/spring total ozone from GOME observations in 1995-2002, *Geophys. Res. Lett.*, **30**, 11, 1583.
- Wirth, V.: 1995, Diabatic heating in an axisymmetric cut-off cyclone and related stratosphere-troposphere exchange, *Q. J. Roy. Meteor. Soc.*, **121**, 127–147.

Erklärung

Hiermit erkläre ich, dass ich die Arbeit ohne unerlaubte fremde Hilfe angefertigt habe, dass ich weiterhin keine anderen als die angegebenen Quellen und Hilfsmittel benutze und die den benutzten Werken wörtlich oder inhaltlich entnommenen Stellen als solche kenntlich gemacht habe.

Bremen, 04.December 2009

Thiranan Sonkaew

Acknowledgements

I am thankful to Dr. Christian von Savigny, Prof. Dr. John Burrows and Dr. Heinrich Bovensmann for accepting me into the SCIAMACHY research team and entrusting me to work on these interesting atmospheric issues.

I wish my sincere special thanks to Dr. Christian von Savigny, my research advisor, for his excellent support of explaining, guidance, understanding and encouragement of entire my research work. I very appreciate all valuable advice and be patient to proofread throughout this dissertation. Without his persistent support this dissertation would not have been possible.

I am very thankful to Prof. Dr. John Burrows for very useful teaching and guidance on atmospheric issues and also motivational advice.

I am indebted to Dr. Heinrich Bovensmann for keeping in touch to my new results, giving advice, as well as finding financial support.

I would like to express my genuine appreciation to Dr. Vladimir Rozanov and Dr. Alexei Rozonov for their fruitful advice, scientific discussion, helping me to be acquainted with the SCIATRAN software, and for their nice collaborative work for my first international scientific journal publication.

Further thanks go to Dr. Kai-Uwe Eichmann and Dr. Astrid Bracher for their guidance in the beginning of the ozone loss task and I am grateful Dr. Kai-Uwe for his advice and discussion on my results.

I also would like to express my thanks to Dr. Sandip Dhomse, a former colleague at IUP, for assistance in technical programming during the earlier stage of my Ph.D. studies.

I am thankful the PEP/PIP program and all the lecturers of the environmental physics courses at IUP. I benefited from the all worthy lectures and excursion activities organized by the PEP/PIP program.

I appreciate the co-operation of the secretaries for their assistance, especially Petra Horn and Anja Gatzka.

Thanks to my officemates: Sebastian Dikty, and Sebastian Meiruch, for making nice atmosphere and helping to translate German sentences, or to make letter.

I am grateful to Heiko Schellhorn and Heiko Schröter for technical computer support.

Thanks to the British Atmospheric Data Centre (BADC) and UK Met Office to create the UKMO dataset and can be accessed. Thanks to Dr. Jens-Uwe Grooß for the ozone loss data from the CLaMs model. Thanks for monthly ozone mean data from Felix Ebojie.

During this work I have collaborated with many IUP colleagues, who have generously shared their knowledge and technical expertise with me. I wish to extend my grateful thanks to all of them.

I also would like to thank Peter and Nongyao Macholl, my landlord and nice neighbours, for providing the perfect house, their social help, and keeping me to be enthusiastic for sport.

My warm thanks go to Joseph Pagaran, Ronald Macatanguy and Anna Chrobry, for making me happy stay in Germany, encouragement, all entertaining, as well as on scientific discussion. Special thanks to Joseph for always being ready to help me with the operating system and programming problems and for his constancy beside me, understanding and inspiring when I was discouraged.

I would like to express my deepest gratitude to my parents and thanks to my sister for their constant love, encouragement supports throughout my life and I always being with me even we were miles away.

Thanks to Lampang Rajabhat University for partial fellowship support and Dr. Wilart Poompimol for driving me to study in Germany.

This work was funded in part by European Space Agency (ESA), the German aerospace center (DLR) and the German Ministry of Education and Research, University of Bremen. It is a pleasure for me to thank the generous financial support.